Digital quantum simulation of physical systems on noisy intermediate-scale quantum computers

Thesis by
Adrian Tan Teck Keng

In Partial Fulfillment of the Requirements for the
Degree of
Doctor of Philosophy

CALIFORNIA INSTITUTE OF TECHNOLOGY
Pasadena, California

2023
Defended May 24, 2023

Adrian Tan Teck Keng
ORCID: 0000-0002-6660-0397

ACKNOWLEDGEMENTS

First, I would like to thank Prof. Austin J. Minnich, who has provided the guidance and resources needed to perform the research outlined in this thesis.

I would also like to extend my thanks to the members of the thesis committee, Prof. Garnet Kin-Lic Chan, Prof. Andrei Faraon, and Prof. Alireza Marandi, for their valuable time and constructive feedback. In addition, I would like to extend my appreciation to the members of my candidacy committee, Prof. Fernando L. Brandao, Prof. Olexei Motrunich, and Prof. Garnet Kin-Lic Chan, again for their valuable suggestions.

I would also like to express my appreciation for members of the Minnich's group, both past and present, for providing your kind help and suggestions. In particular, I appreciate working with Shi-Ning Sun on various quantum simulation projects. I would also like to thank Dr. Mario Motta, and Dr. Sun Chong, former members of the Chan's group with whom I enjoyed collaborating for the QITE project.

My gratitude goes towards Ms. Jennifer Blankenship, the Options Manager for the Applied Physics Department, Ms. Sonya Lincoln, the former secretary of the Minnich's group, and Ms. Laura Flower Kim, the Associate Director at the Caltech International Student office, as well as other members of the staff at Caltech for providing critical help and support.

Lastly, a big thank you to friends and family. I don't think I could have done it without your support.

ABSTRACT

Current quantum computers are characterized as having the order of 5-100 qubits, with limited connectivity restricting two-qubit operations to nearest neighbors, and with too much noise to achieve fault-tolerance. Such devices, called noisy intermediate-scale quantum (NISQ) devices, have been demonstrated to have sufficient coherent lifetime to perform interesting experiments motivated by quantum information sciences. This motivates the question of whether such devices can be utilized to study physical systems commonly encountered in condensed matter and quantum chemistry.

In this thesis, we address the open problem of identifying approaches to perform quantum simulations of physical systems on NISQ devices. We begin our study by considering the Hamiltonian ground state problem, a task routinely solved in numerical studies of materials and molecules. We provided a new quantum primitive, the quantum imaginary time evolution (QITE), that provides a practical approach to solve the Hamiltonian ground state problem. In addition, the QITE subroutine can be used in a Lanczos scheme to speed up convergence time.

Next, we consider the problem of performing finite temperature simulations and demonstrate how QITE can be used as a subroutine to develop scalable and feasible approaches to perform such calculations on a quantum computer. More specifically, we develop routines to obtain thermal averages by sampling minimally entangled thermal states, and also free energy by evaluating the partition function directly.

In our final study, we consider the study of topological states of matter, which do not fit within the Landau paradigm of local order parameters associated with symmetry breaking, and have been shown to exhibit unusual behavior. We show how a specific class of topological states of matter, the symmetry-protected topological states can be feasibly realized on present NISQ devices and their unusual behavior experimentally validated. Our study provides a benchmark of capabilities of state-of-the-art NISQ devices to study these interesting phases of matter.

PUBLISHED CONTENT AND CONTRIBUTIONS

[Include a bibliography of published articles or other material that are included as part of the thesis. Describe your role with the each article and its contents. Citations must include DOIs or publisher URLs if available electronically.

If you are incorporating any third-party material in the thesis, including works that you have authored/co-authored but for which you have transferred copyright, you must indicate that permission has been secured to use the material. For example: "Fig. 2 reprinted with permission from the copyright holder, holder name"

Add the option `iknowwhattodo` to this environment to dismiss this message.]

1. **Tan, Adrian T.K.**, Sun, S.-N., Tazhigulov, R. N., Chan, G. K.-L. & Minnich, A. J. Realizing symmetry-protected topological phases in a spin-1/2 chain with next-nearest neighbor hopping on superconducting qubits. *Phys. Rev. A* **107,** 032614. https://link.aps.org/doi/10.1103/PhysRevA.107.032614 (3 2023).

   Contributions A.T.K.T. conceptualized the project, designed and optimized the quantum circuits, carried out the simulation runs on the quantum computers, performed simulations and analyzed the experimental data, and wrote the manuscript.

2. Motta, M., Sun, C., **Tan, Adrian T. K.**, O'Rourke, M. J., Ye, E., *et al.* Determining eigenstates and thermal states on a quantum computer using quantum imaginary time evolution. *Nat. Phys.* ISSN: 1745-2481. https://doi.org/10.1038/s41567-019-0704-4 (2019).

   Contributions A.T.K.T. designed the quantum circuits to execute the algorithms, carried out the simulation runs on the quantum computers, performed simulations and analyzed the experimental data, and contributed to the writing of the manuscript.

TABLE OF CONTENTS

LIST OF ILLUSTRATIONS

Number *Page*

LIST OF TABLES

Number *Page*

Chapter 1

INTRODUCTION

The formulation of quantum mechanics has provided the theoretical foundation to analyze and understand the behaviors of materials and molecules. Unfortunately, it was and still remains a challenging task to apply the mathematical framework of quantum mechanics. Such difficulties are well captured by Paul Dirac in 1929 [1]:

> The underlying physical laws necessary for the mathematical theory of a large part of physics and the whole of chemistry are thus completely known, and the difficulty is only that the exact application of these laws leads to equations much too complicated to be soluble
>
> It therefore becomes desirable that approximate practical methods of applying quantum mechanics should be developed, which can lead to an explanation of the main features of complex atomic systems without too much computation.

As noted by Dirac, the primary challenge is that the quantum mechanical equations prove too difficult to solve. The advent of digital computers have provided the approach to tackle this problem using computing resources instead, an endeavor which earned Walter Kohn and John A. Pople the Nobel Prize in Chemistry in 1998 [2]. However, even though the use of digital computers had and is likely to continue to bear fruits in the near future, there remains problems of such size and magnitude that are beyond the reach of today's state-of-the-art supercomputer facilities.

Richard Feynman [3] suggested that the challenge in using computers to solve quantum mechanical equations might be a result of representing quantum mechanical systems with classical bits and logic. He speculated that a computer "built of quantum mechanical elements which obey quantum mechanical laws" would be able to efficiently simulate the behavior of quantum mechanical systems. Such an approach is known today as quantum simulation. More than a decade later, Seth Lloyd [4] put on concrete footing, Feynman's vision of a universal quantum simulator and with Daniel S. Adams [5], provided a provable fast algorithm to simulate the time dynamics of the Hubbard model [6]. This subsequently led to

a flurry of theoretical proposals and small-scale demonstrations [7–10] of ways to study the behavior of quantum mechanical systems using simulators made of quantum mechanical elements as envisioned by Feynman.

In this thesis, our focus is on optimizing the utilization of state-of-the-art superconducting quantum processors for quantum simulations, specifically for studying the behavior of materials and molecular systems. To provide a foundation for understanding the main body of this thesis, this chapter introduces the formalism of circuit-based quantum computing. Additionally, we present a concise overview of the superconducting quantum computing architecture that serves as the physical platform for our simulations. The chapter concludes by summarizing each project, outlining the reasons for undertaking them, and highlighting the achieved results. Subsequent research chapters delve into the intricacies of each project. Finally, we conclude by presenting an outlook on the future of quantum simulations using modern quantum computers, while also suggesting potential directions for further exploration and expansion based on the results presented in this thesis.

1.1 Formalism of circuit-based quantum computing

1.1.1 Different approaches to quantum simulation

One approach to quantum simulation is to use a quantum simulator [11], that is a controllable quantum system that can be used to emulate the quantum mechanical systems of interest. Let the state of the simulated system be denoted by $|\phi\rangle$. The system evolves from the initial state $|\phi(0)\rangle$ to $|\phi(t)\rangle$ via the unitary transformation $U = \exp[-i\hbar H_{sys}t]$ where H_{sys} is the Hamiltonian of the system. A quantum simulator works as follows: an initial state $|\psi(0)\rangle$ is prepared and a unitary evolution $U' = \exp[-i\hbar H_{sim}t]$ is engineered by controlling H_{sim}, the Hamiltonian of the simulator. If a mapping between the system and the simulator, that is to say, between $|\phi(t)\rangle$ and $|\psi(t)\rangle$ can be found, then the system can be simulated using the simulator. This approach is known as analog quantum simulation and the schematic of the idea is sketched out in Fig. 1.1.

While there have been successful quantum simulations carried out using various quantum simulators [12–15], this approach has a few drawbacks. First, it is difficult to tune interactions in a simulator and thus, a given setup might only be able to simulate a given subset of quantum mechanical systems and does not serve as a general quantum simulator [16]. More importantly, errors in the experiment accumulate over time and there exists no systematic approach to correct for these

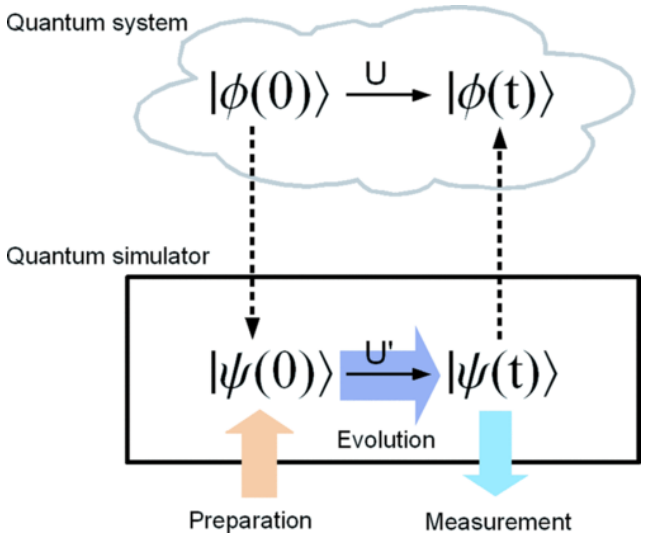

Figure 1.1: **Schematic of the quantum simulation protocol in a typical analog quantum simulation.** A quantum simulator is prepared in an initial state $|\phi(0)\rangle$ and evolves to a state $|\phi(t)\rangle = U|\phi(0)\rangle$ where the unitary U represents the dynamics of the system of interest. Let the initial state and the dynamics of the simulator be represented by $|\psi(0)\rangle$ and U' respectively. Suppose a correspondence can be found between the simulator state $|\psi(t)\rangle = U'|\psi(0)\rangle$, and the state of the system of interest $|\phi(t)\rangle$, the dynamics of the system of interest can be simulated using the simulator. The figure is reproduced from [11].

errors [16].

An alternative approach is to employ quantum computation, which involves using a quantum computational logic device to simulate the behavior of quantum mechanical systems. This method, referred to as digital quantum simulation [11], allows for the simulation of a wide range of quantum mechanical systems, as supported by the universality theorem [17] which we will elaborate on later in the chapter.

There are several models of quantum computation, including the circuit-based model [18], measurement-based model [19], and adiabatic computation model [20]. These models have been shown to be polynomially equivalent to each other [20], meaning they are theoretically equivalent. However, in practice, the circuit-based model has emerged as the dominant choice among experimental groups for implementing digital quantum computers, making it the focus of this thesis. Therefore, our discussion will primarily revolve around the circuit-based model of quantum computation.

1.1.2 Gate operations in circuit model of quantum computation

To ensure clarity and comprehension of the main content of this thesis, we will focus on presenting the fundamental elements of the circuit model for quantum computation as outlined in Nielsen and Chuang [21]. At the core of the circuit model are qubits, which serve as the quantum counterparts of classical bits. A qubit is a two-level quantum system with basis states commonly denoted as $|0\rangle$ and $|1\rangle$. A convenient vector representation of qubits can be expressed as follows:

$$|0\rangle = \begin{pmatrix} 1 \\ 0 \end{pmatrix} \tag{1.1}$$

$$|1\rangle = \begin{pmatrix} 0 \\ 1 \end{pmatrix} \tag{1.2}$$

Ideal, reversible action on qubits are called gates, and transformation of the qubits are unitary as dictated by evolution under the time-dependent Schrodinger equation. Common gates that act on a single qubit are the Pauli operators X, Y, and Z. In the computational basis ordered by $\{|0\rangle, |1\rangle\}$, the matrix representation of these gates are given by

$$X = \sigma_1 = \begin{bmatrix} 0 & 1 \\ 1 & 0 \end{bmatrix} \tag{1.3}$$

$$Y = \sigma_2 = \begin{bmatrix} 0 & -i \\ i & 0 \end{bmatrix} \tag{1.4}$$

$$Z = \sigma_3 = \begin{bmatrix} 1 & 0 \\ 0 & -1 \end{bmatrix} \tag{1.5}$$

where in defining the Pauli operators, we also introduced their common designations as σ_1 σ_2 and σ_3. Any single-qubit gate can be parametrized by

$$U_{single} = \exp(-i \sum_{k=0}^{3} \alpha_k \sigma_k) \tag{1.6}$$

where in this case, $\sigma_0 = I$ is the identity matrix and α_k are all real numbers. Other common single-qubit gates are the Hadamard gate (H), the T-gate, and the phased

gate(S). Their matrix representations are given by

$$H = \frac{1}{\sqrt{2}} \begin{bmatrix} 1 & 1 \\ 1 & -1 \end{bmatrix} \tag{1.7}$$

$$T = \begin{bmatrix} 1 & 0 \\ 0 & e^{i\pi/4} \end{bmatrix} \tag{1.8}$$

$$S = \begin{bmatrix} 1 & 0 \\ 0 & i \end{bmatrix} \tag{1.9}$$

We also have the single-qubit gate $R_z(\theta)$, which performs a rotation of the qubit state around the z-axis by an angle θ. The matrix representation of this gate is given by

$$R_z(\theta) = \begin{bmatrix} e^{-i\theta} & 0 \\ 0 & e^{i\theta} \end{bmatrix} \tag{1.10}$$

In addition to the $R_z(\theta)$ gate, there are also the $R_x(\theta)$ and $R_y(\theta)$ single-qubit gates. These gates perform rotations of the qubit state around the x-axis and y-axis by an angle θ, respectively. These gates can be defined as follows

$$R_x(\theta) = HR_z(\theta)H, \quad R_y(\theta) = S^\dagger R_z(\theta)S \tag{1.11}$$

A group of qubits is referred to as a quantum register, and a natural basis for representing the state of the register is $\otimes_i |q_i\rangle$, where $q_i \in 0, 1$ and i denotes the i-th qubit. Besides applying single-qubit gates, manipulation of the state of the quantum register can also be achieved by applying gates that act on multiple qubits simultaneously. A common example is the CNOT gate, which is a two-qubit gate, and performs a NOT (or X) gate on a target qubit based on the state of a control qubit. In a two-qubit system, the matrix representation of the CNOT gate in the ordered basis $|00\rangle, |01\rangle, |10\rangle, |11\rangle$ is given by

$$\text{CNOT} = \begin{bmatrix} 1 & 0 & 0 & 0 \\ 0 & 1 & 0 & 0 \\ 0 & 0 & 0 & 1 \\ 0 & 0 & 1 & 0 \end{bmatrix} \tag{1.12}$$

A common notation is $\text{CNOT}_{i,j}$ where the control and target qubits are the $i-$th and $j-$th qubits.

Of course, there exists an arbitrary number of unitary operations that can act on an arbitrary number of qubits within a quantum register. Surprisingly, it has been demonstrated that a small set of one and two-qubit gates is sufficient to approximate any arbitrary unitary operation on n qubits to within a desired precision ϵ, as measured by the operator norm. This approximation can be achieved using at most $O(4^n \log^{3.97}(\frac{1}{\epsilon}))$ gates from a universal gate set [17].

One such universal gate set is H, T, CNOT, where H is the Hadamard gate, T is the T gate, and CNOT is the controlled-NOT gate. The earlier claim that digital quantum simulation is a general approach stems from this property. By employing a universal gate set, such as H, T, CNOT, digital quantum simulation allows for the simulation of any quantum mechanical system, highlighting its versatility and broad applicability.

1.1.3 Measurement in circuit base quantum computers

The sequence of quantum gates used to manipulate a quantum register is referred to as a quantum program. Once a quantum program is executed, measurements are often performed to extract information relevant to the specific task at hand. In the context of this thesis, our focus is on measuring the expectation values of Pauli strings, which are operators composed solely of Pauli operators. Examples of such Pauli strings in a two-qubit system include $\langle I_1 \otimes Z_2 \rangle$ and $\langle Z_1 \otimes X_2 \rangle$. For the sake of brevity, we will omit the tensor product notation and remove any identity operators within a Pauli string. Consequently, we will use $\langle Z_2 \rangle$ and $\langle Z_1 X_2 \rangle$ instead of $\langle I_1 \otimes Z_2 \rangle$ and $\langle Z_1 \otimes X_2 \rangle$.

Let us begin by introducing the concept of projective measurements [21]. Since Pauli operators are Hermitian, any Pauli string is also Hermitian. We can express a Hermitian observable A as a sum over its eigenvalues a_k and the projectors P_k associated with the respective eigenspaces. The decomposition is given by

$$A = \sum_k a_k P_k \tag{1.13}$$

For a given state $|\psi\rangle$, the expectation value of the operator A is computed as

$$\langle A \rangle = \sum_k p_k a_k \tag{1.14}$$

Here, $p_k = \langle\psi|P_k|\psi\rangle$ represents the probability of obtaining the eigenvalue a_k when measuring A on the state $|\psi\rangle$.

To establish a connection with experimental procedures and how we estimate the expectation values of Pauli strings using data obtained from experiments, let's consider an example involving a single-qubit system.

Suppose quantum gates have been applied to the quantum register, preparing a state $|\psi\rangle$. The Pauli operator Z has eigenvalues $+1$ and -1 when acting on the computational basis states $|0\rangle$ and $|1\rangle$, respectively. Thus, the computational basis states serve as the eigenbasis for the Pauli operator Z.

In current digital quantum computers, measurements typically involve performing an action that projects the state of interest onto the computational basis, followed by the recording of the measured quantity. In our single-qubit example, a measurement would project the state $|\psi\rangle$ onto either $|0\rangle$ or $|1\rangle$. The measurement instrument would then record the outcome as either $+1$ or -1, corresponding to the eigenvalues of the measured state.

If the experiment is repeated N times, there will be n_{+1} outcomes where $|\psi\rangle$ is projected onto $|0\rangle$ and a $+1$ is recorded, and there will be n_{-1} outcomes where $|\psi\rangle$ is projected onto the $|1\rangle$ and a value of -1 is recorded instead. Using these information, one can estimate p_{+1} and p_{-1}, the probabilities of obtaining the outcome $+1$ and -1 as n_{+1}/N and n_{-1}/N respectively. Then, we have an estimator of the expected value of Z denoted by $\langle\tilde{Z}\rangle$ and given by

$$\langle\tilde{Z}\rangle = (+1)n_{+1}/N + (-1)n_{-1}/N \tag{1.15}$$

The variance of this estimator scales as $(\langle Z^2\rangle - \langle Z\rangle^2)/N$. As we increase the number of measurements N, the variance decreases, indicating that our estimated value becomes more precise.

A similar protocol can be used to estimate the expectation values of the Pauli operators X and Y for our single-qubit state $|\psi\rangle$ with just one difference; a quantum gate is applied to rotate the $|\psi\rangle$ before performing measurement. For example, in order to estimate the expectation value of X, we will apply the Hadamard gate H to obtain a state $|\psi'\rangle = H|\psi\rangle$ before performing measurements as outlined above. This works because if performing the above protocol on the unrotated state $|\psi\rangle$ gives the

estimated value $\langle\psi|Z|\psi\rangle$, then doing measurements on the rotated state $|\psi'\rangle$ gives

$$\langle\psi'|Z|'\psi\rangle = \langle\psi|H^\dagger ZH|\psi\rangle \tag{1.16}$$

$$= \langle\psi|X|\psi\rangle \tag{1.17}$$

where we used the fact that $H^\dagger ZH = X$. Hence, our estimator is now an estimator for $\langle X\rangle$. To obtain the estimator for $\langle Y\rangle$, we apply the gate $S^\dagger$.

Beyond that, we are also need to estimate the expectation value of Pauli strings such as $\langle Z_1X_2\rangle$ and $\langle Z_1X_2Y_3\rangle$. We first consider an example of measuring the Pauli string $\langle Z_1Z_2\rangle$ in a two-qubit system where the two qubits are labelled as qubit 1 and qubit 2 and, where the state of the qubits is given by $|\phi\rangle$.

There are actually two approaches to do so. The first approach is to apply CNOT_{12}, with qubit 1 acting as the control qubit. Then, the measurement protocol described earlier is performed on qubit 2. This gives an estimator for the expectation value $\langle Z_1Z_2\rangle$.

Alternatively, one can perform a measurement on qubit 1, followed by a measurement on qubit 2. Repeating this N times will generate a stream of data that looks like

$$+1+1 \quad -1+1 \quad +1+1 \quad +1+1 \quad -1-1 \quad +1-1... \tag{1.18}$$

where the first value is the outcome of the measurement on qubit 1 and the second is the outcome of the measurement on qubit 2. There are four distinct outcomes: $+1+1, +1-1, -1+1$, and $-1-1$ and $n_{+1,+1}, n_{+1,-1}, n_{-1,+1}$, and $n_{-1,-1}$ are the number of times each outcome occur. Let $P(i|j)$ denote the probability of measuring qubit 2 in state-i after measuring qubit 1 in state-j. This can be estimated from the experiment by noting $P(i|j) \approx \frac{n_{i,j}}{N}$. The estimator of $\langle Z_1Z_2\rangle$, denoted by $\langle Z_1\tilde{Z}_2\rangle$, can be constructed as

$$\begin{aligned}\langle Z_1\tilde{Z}_2\rangle =& \frac{n_{+1,+1}}{N}(+1\times+1) + \frac{n_{+1,-1}}{N}(+1\times-1) \\ &+\frac{n_{-1,+1}}{N}(-1\times+1) + \frac{n_{-1,-1}}{N}(-1\times-1)\end{aligned} \tag{1.19}$$

While it may appear that the second approach is more cumbersome compared to the first, the second approach of applying specific quantum gates before performing measurements becomes particularly advantageous in larger quantum systems where connectivity limitations exist. In experimental setups, it may not always be feasible or straightforward to directly apply a controlled-NOT gate between distant qubits, such as CNOT1, 5 in the case of estimating $\langle Z1Z_5\rangle$.

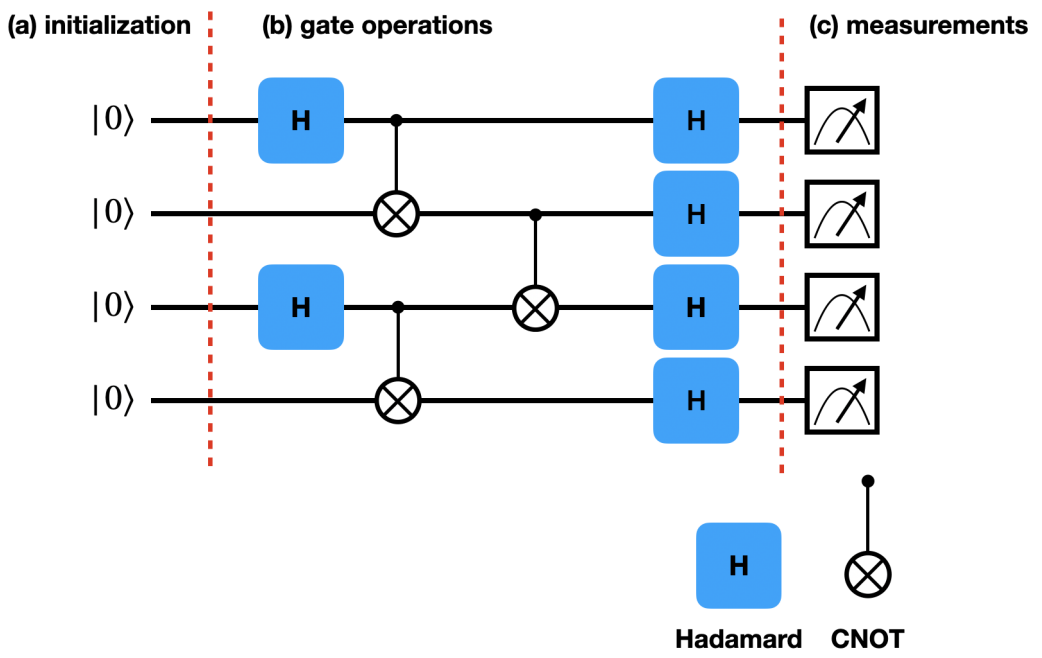

Figure 1.2: **Example of a quantum circuit diagram for a 4-qubit system.** A quantum circuit is usually divided into three steps: (**a**) The quantum register is initialized in the computational basis, which in this case, is given by $\prod_{i=1}^{4} |0\rangle_i$. (**b**) This is followed by a series of gate operations that made up a quantum program. Diagrammatically, the control qubit in a CNOT operation is indicated by $\cdot$ and the target qubit indicated by $\otimes$. (**c**) Finally, measurements are carried out. The measurements are usually repeated in order to construct a precise estimator for the required information.

To estimate the expectation values of Pauli strings that contain X or Y, say $\langle X_1 Y_2 \rangle$, we perform the unitary rotations introduced earlier before applying the measurement protocol. And to estimate the expectation values of longer Pauli strings, we can also generalize the approach outlined above by performing measurements on the relevant qubits and performing the necessary sums.

In summary, a circuit model of quantum computation starts with a register of n qubits initialized in some state, and a quantum program consisting of gate operations act on the qubits resulting in a final state $|\psi\rangle$. Unitary rotations and measurements are then carried out at the end to estimate the expectation value of a Pauli string. This series of operations can be captured in a quantum circuit diagram, and an example is illustrated in Fig. 1.2

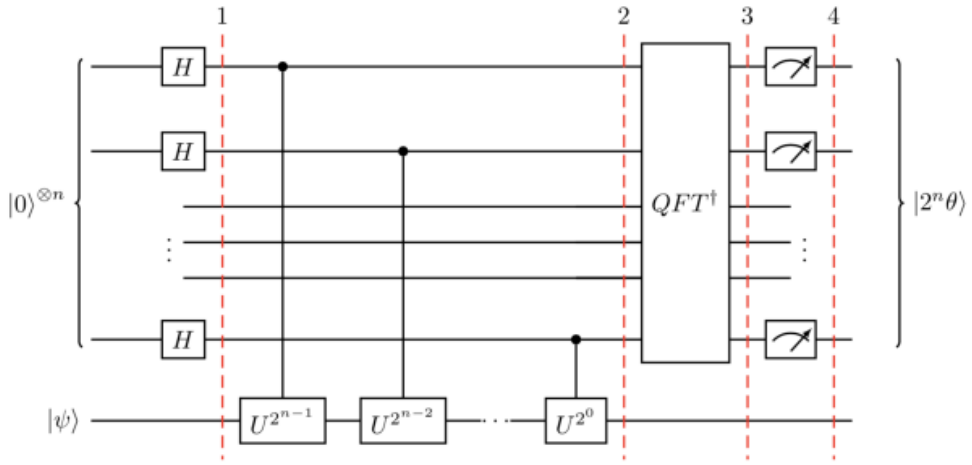

Figure 1.3: **Circuit diagram of the quantum phase estimation algorithm.** (**1**) n ancilla qubits are initialized by applying the Hadamard gate H on each ancillary ancilla. (**2**) Successive application of the controlled-U gate is applied on $|\psi\rangle$. The controlled-U^{2r-1} gate is a shorthand for $2^r - 1$ applications of the controlled-U gate. (**3**) The inverse quantum Fourier transform $QFT^{\dagger}$ is applied on the ancilla register. (**4**) Measurements are carried out on the ancilla qubit. This provides information to reconstruct the eigenvalues. Image is reproduced from [23]

1.2 Quantum phase estimation algorithm

We will use the formalism introduced earlier in Chapter 1.1 to explain how the quantum phase estimation (QPE) algorithm works [22]. Some of the earliest proposals for quantum simulation relies on integrating QPE into its workflow [7, 8]. Understanding the working principles of the QPE algorithm will be particularly beneficial for our discussions in Chapter 2.

We begin by considering an eigenstate $|\psi\rangle$ of some unitary operator U. We assume that $U|\psi\rangle = e^{2\pi i\theta}|\psi\rangle$ where $2^n\theta$ is an integer for some value $n \in \{0, 1, 2, ...\}$ and we wish to estimate the value of this eigenvalue.

The QPE algorithm begins by initializing a register of n ancilla qubits in the state $\otimes_i^n |0\rangle_i$. A Hadamard gate H is applied on each ancilla. The controlled-U^{2r-1} gate is a shorthand for $2^r - 1$ applications of the controlled-U gate. Application of the controlled-U gate are performed as illustrated in Fig. 1.3. The action of the first controlled-U on $|\psi\rangle$ gives

$$|0\rangle \otimes |\psi\rangle + |1\rangle |\psi\rangle \rightarrow |0\rangle \otimes |\psi\rangle + e^{2^n i\theta} |1\rangle \otimes |\psi\rangle \tag{1.20}$$

By applying the controlled-U as illustrated in the diagram, the system is in the state

$$\frac{1}{2^{n/2}} \sum_{k=0}^{2^n-1} e^{2\pi i k\theta} |k\rangle \otimes |\psi\rangle \tag{1.21}$$

where $|k\rangle$ encodes the computational basis in binary format. That is, $|00...00\rangle = |0\rangle$, $|00...01\rangle = |1\rangle$, $|00...10\rangle = |2\rangle$ and, so on. Let $|j\rangle$ be the computational basis encoded in binary format, the quantum Fouier transform, QFT, can be defined by its action on each computational basis state $|j\rangle$ [21]

$$|j\rangle \rightarrow \frac{1}{2^{n/2}} \sum_{k=1}^{2^n-1} e^{2\pi i jk/2^n} |k\rangle \tag{1.22}$$

The inverse quantum Fourier transform, $QFT^\dagger$ inverts this operation. Recall we claim that $2^n\theta$ is an integer, say j. Therefore, the application of $QFT^\dagger$ on $|\psi\rangle_2$ yields the state $|2^n\theta\rangle \otimes |\psi\rangle$. Measuring the ancilla register gives $2^n\theta$.

In the general case, $|\psi\rangle$ is not an eigenstate of U and the eigenvalues of U may not be integers divided by powers of two. Expanding $|\psi\rangle$ by the eigen basis of U $\{\phi_i\}$ gives

$$|\psi\rangle = \sum_i c_i |\phi_i\rangle \tag{1.23}$$

In this case, applying the circuit in Fig. 1.3 and measuring it yields an n-bit approximation to the eigenvalue of $|\phi_i\rangle$ with probability $|c_i|^2$. For sufficiently large n, the post-measurement state yields a very accurate approximation to the eigenstate. In addition, the eigenbasis of U can be measured to within a precision ϵ with a cost (defined as the number of calls to controlled-U) that scales as $O(\frac{1}{\epsilon})$ [21, 22].

1.3 Trotterization scheme

The family of operators represented by $e^{t\sum_i A_i}$ where t can be real or imaginary, is frequently encountered in simulations of quantum mechanical systems. Such operators can be decomposed using the Lie-Suzuki-Trotter [24] formula given by

$$e^{t\sum_i A_i} = \prod_i e^{tA_i} + O(t^2) \tag{1.24}$$

Approaches based on this decomposition were some of the earliest proposals for simulating Hamiltonian dynamical evolution [4]. More sophisticated decompositions that are correct up to arbitrary powers of t [25] exist, but we shall only introduce them when relevant.

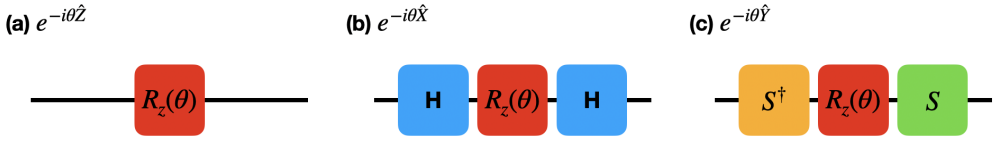

Figure 1.4: **Quantum gate operations to implement one-qubit time evolution.** (**a**) The unitary time evolution $e^{-i\theta\hat{Z}}$ can be implemented as a rotation and (**b**,**c**) $e^{-i\theta\hat{X}}$, $e^{-i\theta\hat{Y}}$ can be implemented by using the appropriate unitary rotations.

In the case where t is real, the resulting operator is non-unitary, and its implementation using quantum gate operations becomes more challenging. However, we will defer the treatment of such cases to Chapter 2.3, where we will discuss the quantum imaginary time evolution (QITE) algorithm.

Here, we will focus on the case where t is imaginary, i.e., $t = im$ where m is a real parameter. Operators of the form e^{imA}, where A is a Pauli string, are frequently encountered in dynamical simulations, and they are unitary. This property enables us to implement them directly using quantum circuits. We shall introduce the necessary circuit elements that can do so.

For a system of one-qubit, the unitary evolution $e^{-i\theta\hat{Z}}$ can be treated as a rotation around the z-axis and hence, implemented as a $R_z(\theta)$ gate operation. In addition, $e^{-i\theta\hat{X}}$ and $e^{-i\theta\hat{Y}}$ can be implemented by using the relevant unitary rotations: $e^{-i\theta\hat{X}} = \hat{H}R_z(\theta)\hat{X}$ and $e^{-i\theta\hat{Y}} = \hat{S}R_z(\theta)\hat{S^\dagger}$. The circuit layouts are illustrated in Fig. 1.4.

We now consider dynamical evolution of a two-qubit system with the time evolution operator given by $e^{-i\theta\sigma_1\sigma_2}$ where $\sigma_1, \sigma_2 \in \{\hat{X}, \hat{Y}, \hat{Z}\}$. In the particular case of $e^{-i\theta\hat{Z}_1\hat{Z}_2}$, it can be shown that this can be implemented using the circuit represented by $\text{CNOT}_{1,2}R_{z2}(\theta)\text{CNOT}_{1,2}$ where $R_{z2}(\theta)$ is a rotation of qubit-2 around the z-axis by θ. The circuit schematic is given in Fig 1.5a. In the case where the Pauli strings contain terms that are not $\hat{Z}$, such as $e^{-i\theta\hat{X}_1\hat{Y}_2}$, we can implement by doing a pre- and post-rotation. More concretely, $e^{-i\theta\hat{X}_1\hat{Y}_2} = (H_1 \otimes S_2)\text{CNOT}_{1,2}R_{z2}(\theta)\text{CNOT}_{1,2}(H_1 \otimes S_2^\dagger)$ and the circuit layout is shown in Fig. 1.5b.

Unitary time evolution containing three or more Pauli strings can be implemented using a quantum circuit with a cascaded CNOTs structure. For example, the evolution $e^{-i\theta\hat{Z}_1\hat{Z}_2\hat{Z}_3\hat{Z}_4\hat{Z}_5}$ can be constructed as $\text{CNOT}_{1,2}\text{CNOT}_{2,3}\text{CNOT}_{3,4}\text{CNOT}_{4,5}$ $R_{z5}(\theta)$ $\text{CNOT}_{4,5}\text{CNOT}_{4,3}\text{CNOT}_{2,3}$ $\text{CNOT}_{1,2}$ as shown in Fig. 1.6. If there are non $\hat{Z}$ terms, unitary rotations are prepended and appended to the cascaded CNOT

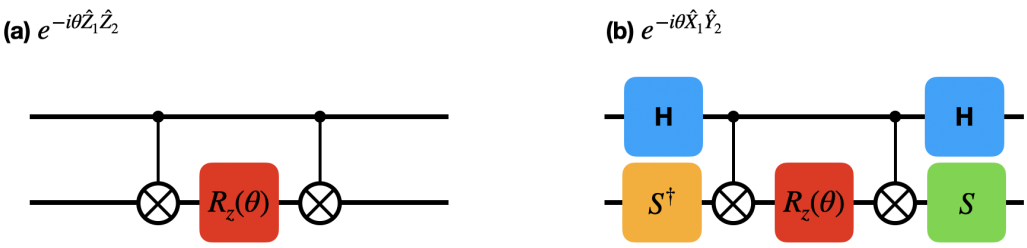

Figure 1.5: **Quantum gate operations to implement two-qubit time evolution.** (**a**) $e^{-i\theta\hat{Z}_1\hat{Z}_2}$ can be implemented using $\text{CNOT}_{1,2}R_{z2}(\theta)\text{CNOT}_{1,2}$. (**b**) When there are non$-\hat{Z}$ terms in the Pauli strings, we perform the appropriate unitary rotations. For example, the evolution $e^{-i\theta\hat{X}_1\hat{Y}_2}$ can be constructed as $(H_1 \otimes S_2)\text{CNOT}_{1,2}R_{z2}(\theta)\text{CNOT}_{1,2}(H_1 \otimes S_2^\dagger)$.

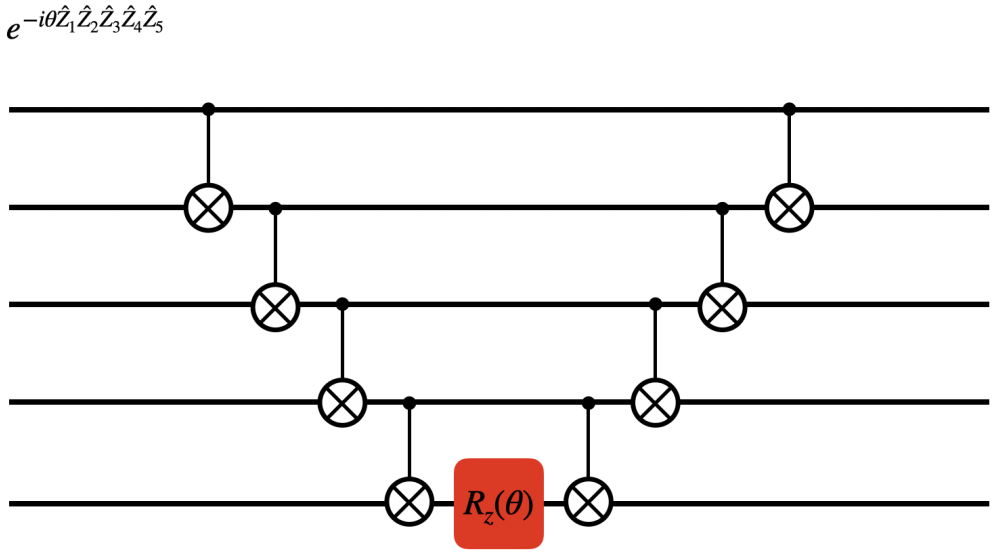

Figure 1.6: **Quantum circuit to implement time evolution with 3 or more Pauli string terms.** The circuit has a cascaded CNOT structure and the layout to implement $e^{-i\theta\hat{Z}_1\hat{Z}_2\hat{Z}_3\hat{Z}_4\hat{Z}_5}$ is shown. If there are non$-\hat{Z}$ terms, we will perform unitary rotations like in Fig. 1.5

structure as in Fig. 1.5.

1.4 Noisy intermediate-scale quantum computer devices

Having discussed the formalism of circuit-based quantum computation, we now provide a brief introduction to the experimental platforms used for implementing the circuit model of quantum computation. While this overview does not aim to be exhaustive, it focuses on three prominent platforms: (i) superconducting quantum

processors based on the transmon architecture, (ii) trapped ion quantum computers, and (iii) neutral atom qubits. As of 2023, these platforms serve as the foundation for hardware architectures adopted by quantum cloud-service providers [26–30]. For a more comprehensive review, refer to the report cited [31].

Arguably, the leading platforms in quantum computing is the modern superconducting quantum processor based on the transmon architecture [32, 33]. Transmons utilize the lowest two levels of a weakly anharmonic oscillator as qubits. These superconducting quantum processors offer several advantages. They can perform gate operations within tens of nanoseconds [34], enabling fast operations and a higher number of repeated measurements for data collection. Moreover, the fabrication of superconducting processors can leverage established semiconductor fabrication processes, allowing for the use of off-the-shelf components from foundries [31]. Consequently, prominent quantum cloud-service providers such as Rigetti [26], IBM [27], and Google [28] have initially built their quantum processors based on the transmon architecture. Notably, Google's highly acclaimed quantum supremacy experiment [35] was conducted using a 53-qubit Sycamore chip, which utilizes the transmon architecture.

A competing alternative is the ion trap quantum computer [36]. In these devices, ions are suspended in a vacuum using electromagnetic fields, and the atomic energy levels of the trapped ions serve as the basis for the qubits. One notable advantage of trapped ion devices is the guarantee of identical qubits, which cannot be said for transmon-based superconducting quantum processors. Additionally, modern ion trap quantum computers exhibit long coherence times on the order of seconds [36], surpassing the typical microseconds reported in superconducting-based quantum processors [34]. However, the platform faces some drawbacks. Firstly, gate operations in trapped ion systems are slower, with typical two-qubit gate times around 100μs [36], compared to the faster operations achieved with transmons. Furthermore, scaling up trapped ion systems is more challenging [36], resulting in significantly fewer qubits compared to superconducting platforms.

Neutral atom quantum computers [37] are similar to ion trap quantum computers, with the key distinction being the use of neutral atoms trapped using optical tweezers instead of electrically-charged ions as qubit bases. Due to their electrical neutrality, neutral atoms can be densely packed in a smaller area, allowing for scalability with more qubits. However, a major challenge with this technology is that each atom necessitates its own set of lasers and control mechanisms [38].

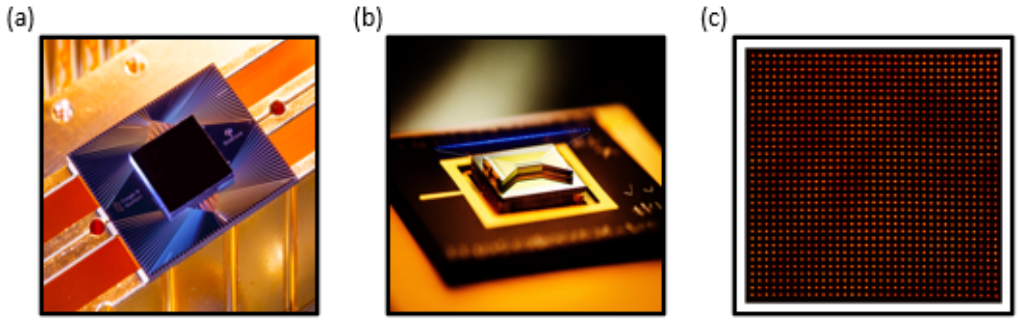

Figure 1.7: **Different quantum computing architectures.** (**a**) 53-qubit Sycamore chip built using transmon architecture [35] (**b**) IonQ's trapped ion system [39]. (**c**) Neutral atoms quantum computer in the Saffman's lab [40].

Examples of existing quantum hardware built using the aforementioned technologies can be seen in Fig. 1.7. For this thesis, all projects were conducted using superconducting quantum processors provided by cloud service providers. This choice was primarily driven by the availability of such hardware from 2018 to 2022, the timeframe in which the projects were completed. It remains to be determined which approach will ultimately prove the most successful.

As of 2023, all the platforms can be considered as noisy intermediate-scale quantum (NISQ) [41] devices. They are characterized as having on the order of 5-100 qubits, with limited connectivity restricting two-qubit operations to nearest neighbors and, with too much noise to achieve fault-tolerance. Yet such devices have coherent lifetime that may be sufficient for practical applications. Thus, there have been a flurry of activities in trying to discover potential applications of NISQ devices.

To identify applications for NISQ devices, it is crucial to understand how noise can impact their performance. In most cases, the specific sources of noise encountered in an experiment can be disregarded, and a phenomenological model of noise can be employed to capture the experimental outcomes.

1.5 Noise models for quantum computing

In this section, we will explore different approaches to comprehend the non-ideal behaviors observed in quantum computing hardware, which stem from the presence of noise. Rather than delving into the specific sources of noise, we will focus on phenomenological models that can capture their characteristics. These models offer a quantitative framework for representing the data obtained from our experiments and prove adequate for our purposes.

1.5.1 Depolarizing, dephasing, and amplitude damping channels

Noise that occurs during the application of single-qubit and two-qubit operations are often modeled using quantum channel formalism [42]. In this formalism, the most general valid transformation of a quantum state is a completely positive trace-preserving (CPTP) map. A transformation defined by $\Phi(\rho)$ is a CPTP map if and only if it can be expressed in the form

$$\Phi(\rho) = \sum_a M_a \rho M_a^\dagger \tag{1.25}$$

for a collection of operators $\{M_a\}$ that satisfies

$$\sum_a M_a M_a^\dagger = I \tag{1.26}$$

We repeat some of the common models [42] for reference here. One common model is the single-qubit amplitude damping channel. The Kraus operator representations that defined this channel is given by

$$M_0 = \begin{pmatrix} 1 & 0 \\ 0 & \sqrt{1-p_a} \end{pmatrix}, \; M_1 = \begin{pmatrix} 0 & \sqrt{p_a} \\ 0 & 0 \end{pmatrix} \tag{1.27}$$

where p_a is known as the decay probability. One way to interpret this channel is that if the state of the qubit is $|\psi\rangle = |1\rangle$, then there is a $1 - p_a$ probability that nothing happens to the qubit, that is it remains in state $|1\rangle$ and a p_a probability that it decays to $|0\rangle$.

Another model is the single-qubit dephasing channel with its Kraus operator representations given by

$$M_0 = \sqrt{1-p_d} I, \; M_1 = \begin{pmatrix} \sqrt{p_d} & 0 \\ 0 & 0 \end{pmatrix}, \; M_2 = \begin{pmatrix} 0 & 0 \\ 0 & \sqrt{p_d} \end{pmatrix} \tag{1.28}$$

where p_d is known as the dephasing probability. A way to interpret this channel is that phase information is lost. To see this, consider an initial state given by $|\psi\rangle = \alpha|0\rangle + \beta|1\rangle$. Under the action of this channel, the resulting ensemble is $|\alpha|^2|0\rangle\langle 0| + |\beta|^2|1\rangle\langle 1|$. The off diagonal components in the density matrix is lost.

One more example of a commonly used channel is the single-qubit depolarizing channel. Its Kraus operator representations is given by

$$M_1 = (1 - p_{del})I, \; M_2 = \frac{p_{del}}{3} X, \; M_3 = \frac{p_{del}}{3} Y, \; M_4 = \frac{p_{del}}{3} Z \tag{1.29}$$

where p_{del} is the depolarizing probability. A way to interpret this channel is that there is a $1 - p_{del}$ probability that nothing happens, and a probability of $p_{del}/3$ that either X, Y or Z is applied on the qubit. The effect of this can be observed from its action on a state $|\psi\rangle = \alpha|0\rangle + \beta|1\rangle$. The action of this channel is that it has a $1 - p_{dep}$ probability that nothing happens to the state, and a p_{dep} probability that the resulting state is $|0\rangle\langle 0| + |1\rangle\langle 1|$, which is a maximally-mixed state where all useful information is washout.

1.5.2 Readout errors

Another error commonly encountered arise due to noise during the measurement process [35, 43]. Such errors occur due to coupling between the qubit and the environment when trying to read information from it. The effect of measurement error leads to the qubit's state being 'flipped'. To illustrate this, we consider during the measurement of a single qubit, a $|0\rangle$ is measured to be $|1\rangle$. The reverse, where a $|1\rangle$ is measured to be $|0\rangle$ can also occur.

These errors can be modelled by a classical noise model that describes a noisy n-qubit measurement by a matrix of transition probabilities M of size $2^n \times 2^n$ such that $M_{y(r),x(s)}$ is the probability of observing a measurement outcome $|r\rangle$ provided that the true outcome is $|s\rangle$ [43]. Going back to our example, a noise model to describe the measurement errors encountered in a single-qubit system is given by

$$\begin{pmatrix} y(0) \\ y(1) \end{pmatrix} = \begin{bmatrix} M_{y(0),x(0)}, & M_{y(0),x(1)} \\ M_{y_1,x(0)}, & M_{y(1),x(1)} \end{bmatrix} \begin{pmatrix} x(0) \\ x(1) \end{pmatrix} \tag{1.30}$$

where $x(0), x(1)$ are the true probabilities of measuring the state in $|0\rangle, |1\rangle$ respectively, and $y(0), y(1)$ are the observed probabilities due to the presence of the measurement noise.

1.5.3 Coherent errors

Most of the errors we mention are stochastic in nature, where there is a probability p_{err} where the error occurs, and a probability $1 - p_{err}$ where nothing happens. In addition to stochastic errors, errors can be coherent too [44]. One example will be errors resulting from systematic shift in control parameters. An illustrative example will be to consider the single-qubit gate operation to $R_z(\theta)$ [45]. It is possible that during the calibration of the gate, an angle of $\theta + \delta$ is applied instead of θ. The systematic shift δ is an example of coherent error.

To sum it all, today's qubits are heavily affected by noises and the phenomenological

Figure 1.8: **Quantum circuits to estimate transition probabilities A for a system of one qubit.** (**a**) In an ideal situation, measurements in this circuit should produce only 0. However, due to readout errors, we observe 1s in our data stream. Given the data, we can estimate $A_{y(0),x(0)}$ and $A_{y(1),x(0)}$, the probabilities of observing 0 and 1 given the state is 0 respectively. (**b**) Similarly, measurements in this circuit should produce only 1. However, due to readout errors, we observe 0s in our data stream. Given the data, we can estimate $A_{y(0),x(1)}$ and $A_{y(1),x(1)}$, the probabilities of observing 0 and 1 given the state is 1 respectively.

models we introduce provide a sufficient method to model the effects of noise in our experiments.

1.6 Error mitigation techniques

In this section, we will delve into the concept of error mitigation [46]. As discussed in Chapter 1.4, NISQ devices exhibit significant noise levels that prevent the achievement of fault-tolerant quantum computing. Consequently, noise will unavoidably manifest in the data obtained from NISQ devices for the foreseeable future. In order to harness the potential of NISQ devices for solving real-world problems, it becomes crucial to mitigate the impact of noise through post-processing techniques [46]. In this context, we will outline several error mitigation strategies employed in our work.

1.6.1 Readout error mitigation

As discussed in Chapter 1.5.2, measurement errors can be characterized by a classical noise model represented by a transition matrix A. In the case of a single-qubit system, this can be described by Eqn. 1.30.

One approach to mitigate the impact of readout errors [43] is to estimate the transition matrix $M_{y(k),x(k)}$ and utilize it, along with the observed probabilities $y(k)$, to infer

the true probabilities $x(k)$. To achieve this, we can employ the circuits depicted in Fig. 1.8a and 1.8b to estimate the transition matrices $M_{y(0),x(0)}$, $M_{y(1),x(0)}$, $M_{y(0),x(1)}$, and $M_{y(1),x(1)}$, which fully characterize our classical readout error model. Subsequently, we can leverage these estimates in combination with Eqn. 1.30 to enhance the accuracy of our probability estimates. As discussed in Chapter 1.1.3, these improved estimates can then be utilized to compute expectation values of desired observables.

The readout error mitigation strategy was successfully implemented in the work presented in Chapter 4, and we will defer the discussion into the observed improvements to then.

1.6.2 Post-selection by symmetry

An additional approach for mitigating errors involves identifying errors that violate symmetry constraints and applying post-selection techniques to remove them [46]. Many quantum circuits possess inherent symmetries that can be leveraged for error mitigation. By measuring these inherent symmetries and discarding circuit runs that produce incorrect results, a post-selected state can be obtained, from which the expectation values of desired observables can be more accurately determined [47, 48].

To illustrate this concept, let's consider the total spin symmetry defined as

$$\hat{S}\text{total} = \sum i^N \hat{Z} i \tag{1.31}$$

In the computational basis, all eigenstates of $\hat{S}$total are represented. For instance, in a system with 4 qubits, the state $|0001\rangle$ is an eigenstate with a total spin of 1. If a quantum program U commutes with $\hat{S}$total, applying U to $|\psi\rangle$ would still yield an eigenstate of $\hat{S}$total with a definite total spin. Consequently, if we measure $U|0001\rangle$ in the z-basis, we would expect measurement outcomes corresponding only to bitstrings associated with a total spin of 1.

The presence of hardware noise can result in bitstrings with incorrect total spin values. By discarding such bitstrings and utilizing the remaining measurements, the desired observables can be accurately determined. Figure 1.9 illustrates an example of post-selection by total spin symmetry. Post-selection by symmetry was effectively employed in Chapter 5, and a detailed discussion on the observed improvements will be provided in that chapter.

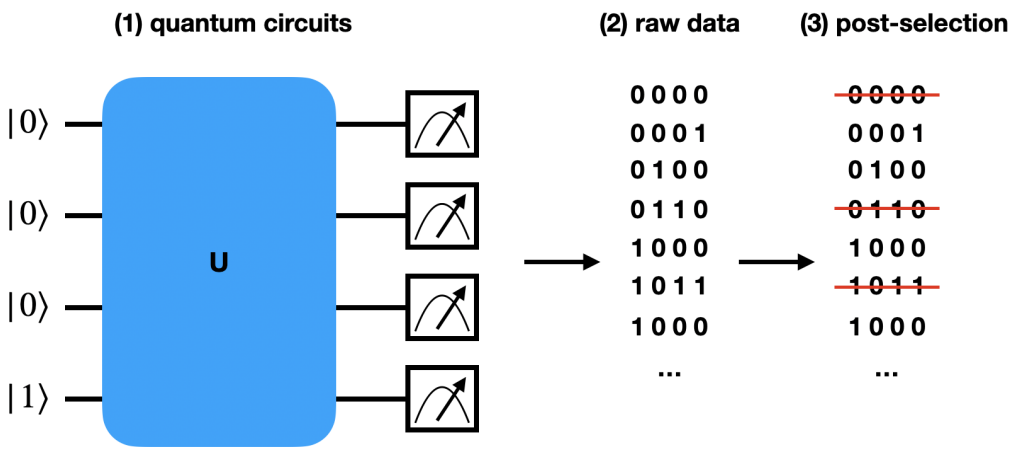

Figure 1.9: **Outline of post-selection by total spin symmetry.** (**1**) Our initial $|0001\rangle$ is an eigenstate of the total spin symmetry with total spin 1. If the quantum program U commutes with the total spin symmetry, $U|0001\rangle$ is also an eigenstate with total spin 1. (**2**) Presence of hardware noise may lead to bitstrings with the wrong total spin. (**3**) Bitstrings with the wrong total spin can be discarded. The discarded bitstrings are crossed-out with a red line for illustration purpose. The remaining measurements can be used to determine the observables of interest.

1.7 Outline of thesis

Having provided the introductory material on the formalism of circuit-based quantum computation and noise analysis, we are ready to present a brief outline of the thesis in this section. All the chapters are related by the main theme of discovering approaches to perform quantum simulations on a gate-based quantum computer.

In Chapter 2, we address the Hamiltonian ground state problem, which is a fundamental task in numerical studies of materials and molecules. We examine existing approaches for solving this problem on current quantum computers and discuss their limitations, including a quantum primitive called quantum imaginary time evolution (QITE) introduced by our collaborators. We present our efforts to validate the approach by implementing the algorithms on Rigetti's Aspen-1 superconducting processor and showcase its potential for accurately determining the ground state behavior of physical systems [49].

Moving on to Chapter 3, our focus shifts to finite temperature simulations. We illustrate how QITE can be employed as a subroutine to develop scalable and feasible methods for performing these calculations on quantum computers. Specifically, we demonstrate how QITE can be used to obtain thermal averages by sampling minimally entangled thermal states [49] and and to determine the free energy of a

system by evaluating the partition function.

In Chapter 4, we delve into the study of topological states of matter, which exhibit unconventional behavior and cannot be characterized by local order parameters associated with symmetry breaking within the Landau paradigm. We explore the feasibility of realizing a particular class of topological states known as symmetry-protected topological states on current NISQ devices. Additionally, we experimentally validate the unusual behavior associated with these states. Our study [50] serves as a benchmark for assessing the capabilities of state-of-the-art NISQ devices in investigating these intriguing phases of matter.

Lastly, in Chapter 5, we consolidate the significant findings from the aforementioned research and offer a comprehensive summary of our results. We also provide an overview of the ongoing developments in each respective area, highlighting the potential for further advancements. Moreover, we explore new directions that can build upon the outcomes we have achieved, presenting exciting opportunities for future exploration and expansion of our work.

Chapter 2

QUANTUM IMAGINARY TIME EVOLUTION (QITE) FOR THE DETERMINATION OF GROUND STATE PROPERTIES

This chapter has been adapted from:

1. Motta, M., Sun, C., **Tan, Adrian T. K.**, O'Rourke, M. J., Ye, E., *et al.* Determining eigenstates and thermal states on a quantum computer using quantum imaginary time evolution. *Nat. Phys.* ISSN: 1745-2481. https://doi.org/10.1038/s41567-019-0704-4 (2019).

   Contributions A.T.K.T. designed the quantum circuits to execute the algorithms, carried out the simulation runs on the quantum computers, performed simulations and analyzed the experimental data, and contributed to the writing of the manuscript.

The computation of the ground state $|\psi\rangle$ of a Hamiltonian $\hat{H}$ is one of the most promising applications of quantum computers. However, the limitations of NISQ devices necessitate the development of resource-efficient methods for such tasks. Existing approaches, such as quantum phase estimation and variational quantum algorithms, have their limitations. Quantum phase estimation relies on deep circuits that are currently impractical for NISQ devices, while variational quantum algorithms involve shallower circuits but require solving high-dimensional optimization problems.

In this chapter, we present our efforts to implement and benchmark the quantum imaginary time evolution (QITE) algorithm on current quantum hardware. This algorithm was proposed by our collaborators as an alternative solution for the Hamiltonian ground state problem on NISQ devices.

We begin by discussing previous proposals for solving the Hamiltonian ground state using quantum computers. We then introduce the variational quantum eigensolver (VQE) as a method that has already been implemented on NISQ devices, demonstrating the potential of quantum computing platforms for solving the ground state problem. Next, we present the theoretical formulation of QITE, which is an adaptation of the imaginary time evolution proposed by our collaborators. The algorithm significantly reduces time and space requirements, eliminating the need for deep circuits or high-dimensional optimization. Additionally, we present our collaborators'

adaptation of the Lanczos scheme, which, based on numerical evidence, exhibits a faster convergence rate to the ground state solution.

We then describe our efforts to implement the schemes on gate-based quantum computers using quantum circuits. We successfully validate QITE on Rigetti's Aspen-1 transmon superconducting devices. Furthermore, we perform a detailed resource analysis comparing QITE and VQE, revealing that QITE requires fewer measurement resources compared to VQE. These results uncover a new class of quantum algorithms with promising prospects for Hamiltonian ground state simulations.

2.1 Background

The accurate computation of ground state properties is a common routine in the fields of quantum chemistry and materials science [16]. It can be formally treated as

$$E_0 = \min_{|\psi\rangle} \langle\psi|\hat{H}|\psi\rangle \tag{2.1}$$

where $\hat{H}$ is the Hamiltonian of the chemical or materials system of interest, and E_0 is the ground state energy. While such calculations can be carried out on classical computers [2], there is growing interest in investigating the use of quantum computation to carry out such routines and determining whether such calculations can be completed exponentially quicker on quantum computers [51]. Suppose the latter is true, quantum computers can potentially revolutionize application areas like drug designs and materials development [16].

Unfortunately, results from complexity theories have ruled out quantum advantage for solving the Hamiltonian ground state problem [52]. It is now known that the k-local Hamiltonian ground state problem is in the Quantum Merlin Arthur (**QMA**) class, meaning a quantum computer will not offer an exponential speedup in finding the ground state of a generic k-local Hamiltonian. One particular example with relevance to materials science, finding the ground state of the Hubbard model in an external magnetic field, is likely to be a **QMA**-complete problem [53].

While complexity arguments imply that no exponential speedup can be expected for generic Hamiltonians, it does not rule out the possibility that certain Hamiltonians encountered in quantum chemistry and materials science may be efficiently solvable on quantum computers, while remaining exponentially hard to solve using classical methods.

Therefore, it is important to actively pursue the targeted development of quantum

algorithms for computing ground state energies and thoroughly test their performance on specific Hamiltonians of interest. Such studies are warranted to explore the potential advantages offered by quantum computing in solving relevant problems motivated by materials science and quantum chemistry.

Initial studies [7, 8] investigating the use of quantum computers for ground states computation of atomic and molecular energy levels all relied on quantum phase estimation algorithm (see Chapter. 1.2) in their proposed protocol. otably, Aspuru-Guzik et al. (2005) presented a protocol for efficiently estimating the ground state energies of molecules, assuming the availability and efficient preparation of a reference state with significant overlap with the true ground state. However, the algorithm requires very long and deep circuit depth due to the need to apply the inverse quantum fourier transform, and the controlled-gates. As a result, despite algorithmic improvements [54–57] aimed at reducing the number of required quantum gate operations, and some successful small-scale demonstrations [10, 58], it remains unlikely that the algorithm can be reliably implemented on present-day NISQ devices to simulate larger systems of interest. This necessitates the development of alternative algorithms capable of running more reliably on today's devices.

2.2 Formulation of variational quantum eigensolver (VQE)

Variational quantum eigensolver (VQE) [59, 60] is a promising class of state preparation methods that can be used to compute ground state energies on present noisy NISQ device. Let $\hat{H}$ denotes the Hamiltonian of interest whose ground state energy E_G we wish to determine. The VQE method begins by selecting an ansatz, typically a parameterized quantum circuit represented by $U(\hat{\theta})$. This ansatz acts on an initial state $|\psi\rangle$, often chosen as the computational basis $\otimes_i|0\rangle_i$, resulting in the ansatz state $|\psi(\hat{\theta})\rangle = U(\hat{\theta})|\psi\rangle$. The energy of this ansatz state is estimated through the measurement protocol outlined in Chapter 1.1, providing an upper bound to the ground state energy E_G according to the Rayleigh-Ritz variational principle [61]. To estimate E_G, we can solve the following optimization problem

$$\min_{\hat{\theta}} = \langle\psi(\hat{\theta})|\hat{H}|\psi(\hat{\theta})\rangle \tag{2.2}$$

can thus be solved to estimate E_G. A schematic illustrating the workflow of VQE is presented in Figure 2.1.

In order for the approach to be successful, the chosen ansatz must not only provide a good approximation to the true ground state, but it should also be feasible to execute on NISQ devices [16]. Empirically, this was found to be true, enabling the successful

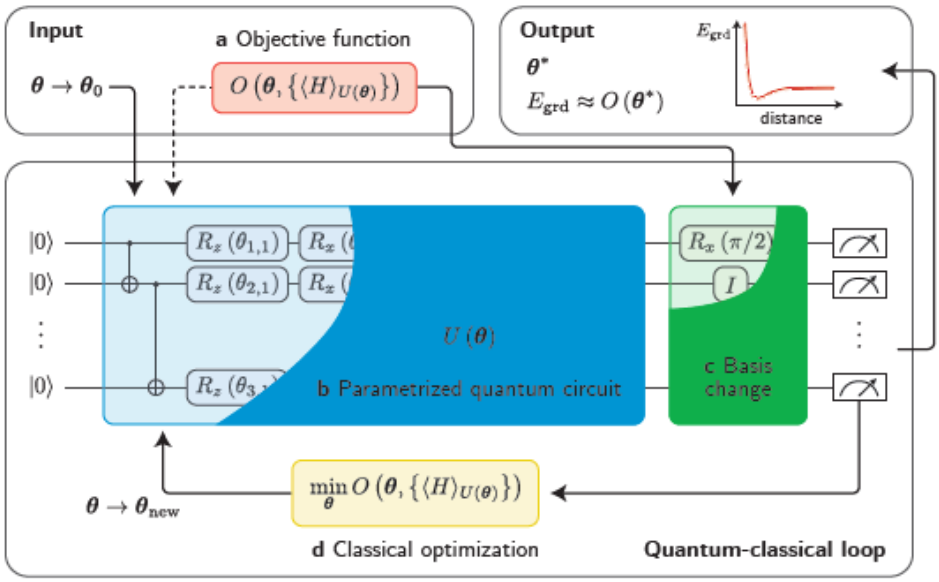

Figure 2.1: **Schematic of VQE workflow.** A VQE workflow can be divided into four main components: (**a**) the objective function O encodes the problem to be solved such as solving the ground state of a Hamiltonian H; (**b**) the parametrized quantum circuit U, which variables θ are tuned to minimize the objective; (**c**) the measurement scheme in which basis changes and measurements needed to compute expectation values that are used to evaluate the objective; and (**d**) the classical optimizer that minimizes the objective. The optimal set of parameters are denoted by $\theta*$. The figure is reproduced from [62].

determination of ground state energies for various chemical and condensed matter systems using VQE [59, 63, 64]. An example of applying this approach to compute the ground state energy of BeH_2 is illustrated in Figure 2.2.

However, one notable drawback of the VQE approach is the potential difficulty in solving the optimization problem [65]. This is particularly true when the energy landscape exhibits complex dependencies with many local minima or regions of vanishing gradients [65]. Additionally, accurately estimating the energy may require a large number of measurements [60]. These challenges highlight the need for alternative approaches that circumvent high-dimensional optimization and with lesser measurement requirements.

2.3 Formulation of QITE

The quantum imaginary time evolution algorithm (QITE) was proposed by our collaborators [49] as an alternative to treat the Hamiltonian ground state problem on NISQ devices. QITE is a quantum analogue to the imaginary time evolution [66],

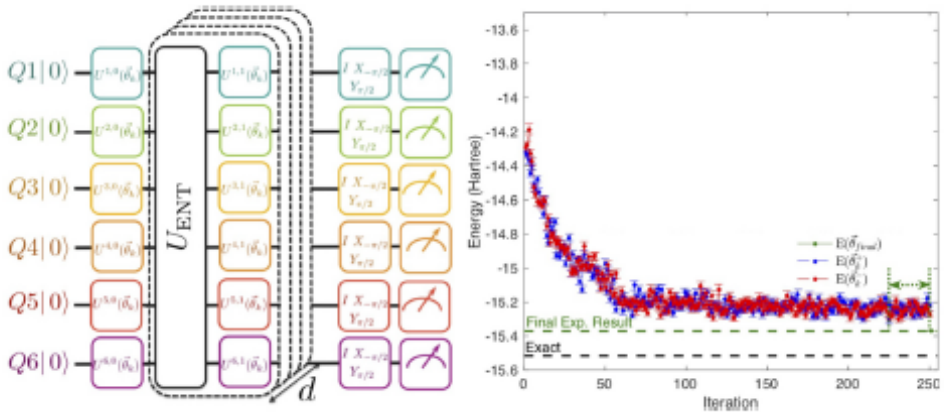

Figure 2.2: **Implementation of VQE to solve for the ground state energy of BeH_2.** (**Left**) Hardware-efficient quantum circuit for trial state preparation and energy estimation, shown here for 6 qubits. The circuit is composed of a sequence of interleaved single-qubit rotations, and entangling unitary operations UENT that entangle all the qubits in the circuit. A final set of post-rotations prior to qubit readout are used to measure the expectation values of the terms in the qubit Hamiltonian, and estimate the energy of the trial state. (**Right**) energy minimization for the six-qubit Hamiltonian describing BeH_2. The figure is reproduced from [63].

an approach commonly employed on classical computers to find the ground state wavefunction and energy of a system of interest [67]. The method does not require the deep circuits commonly found in quantum phase estimation algorithms, and does not need to solve the high-dimensional optimization problem that is encountered frequently in VQE.

2.3.1 Imaginary time evolution

For a system described by the Hamiltonian $\hat{H}$, the imaginary time dynamics of a state $|\psi\rangle$ is governed by

$$-\partial_\beta|\psi\rangle = \hat{H}|\psi\rangle \tag{2.3}$$

where $\beta = it$ with $\hbar$ is taken to be one for convenience. Assuming that the Hamiltonian is time-independent, then for an initial state $|\psi(0)\rangle$, the normalized imaginary time evolution to imaginary time τ is given by

$$|\psi(\tau)\rangle = \mathcal{N}^{-1/2}(\tau)e^{-\tau\hat{H}}|\psi(0)\rangle, \quad \mathcal{N} = \langle\psi(0)|e^{-2\tau\hat{H}}|\psi(0)\rangle \tag{2.4}$$

where the normalization factor $\mathcal{N}(\tau)$ arises due to the fact that the propagator $e^{-\tau H}$ is non-unitary. The ground state wavefunction and energy of $\hat{H}$ can be obtained

using imaginary time evolution as

$$|\psi\rangle_{ground\ state} = \lim_{\beta\to\infty} e^{-\beta\hat{H}}|\psi\rangle / || \, e^{-\beta\hat{H}}|\psi\rangle \, || \tag{2.5}$$

2.3.2 QITE

The challenge in implementing imaginary time evolution on a quantum computer arises from the fact that the imaginary time propagator is non-unitary. The difficulty can be circumvented as such: First, consider a geometric k-local Hamiltonian $\hat{H} = \sum_r \hat{h}_r$(where each term $\hat{h}_r$ acts on at most k neighbouring qubits) and perform a first-order Trotter decomposition of the imaginary time propagator:

$$e^{-\tau\hat{H}} = (e^{\Delta\tau\hat{H}})^n + O(\Delta\tau), \quad \Delta\tau = \frac{\tau}{n} \tag{2.6}$$

At the $(m+1)$th Trotter step, the normalized state $|\psi(m+1)\rangle$ is given by

$$|\psi(m+1)\rangle = c(m+1)^{-1/2} e^{-\Delta\tau\hat{H}}|\psi(m)\rangle \tag{2.7}$$

$$c(m+1) = \langle\psi(m)|e^{-2\Delta\tau\hat{H}}|\psi(m)\rangle \tag{2.8}$$

$$\approx 1 - 2\Delta\tau\langle\psi(m)|\hat{H}|\psi(m)\rangle \tag{2.9}$$

Our collaborator's approach is to find a unitary operator $e^{-iA(m)}$ that maps $|\psi(m)\rangle$ to $|\psi(m+1)\rangle$. $A(m)$ can be expanded as a sum of Pauli basis that spans the system:

$$A(m) = \sum_{i_1,i_2,\ldots,ik} a(m)_{i_1 i_2 \ldots i_k} \sigma_{i_1} \otimes \sigma_{i_2} \ldots \otimes \sigma_{i_k} \tag{2.10}$$

with $a(m)_{i_1 i_2 \ldots i_k}$ being the coefficient of the $i_1 i_2 \ldots i i_k$ Pauli basis at step m and k is the size of the system.

To determine the weights, the rotated state $|\tilde{\psi}(m+1)\rangle$ can be defined as

$$|\tilde{\psi}(m+1)\rangle = e^{-iA(m)}|\psi(m)\rangle \tag{2.11}$$

and define the difference between this rotated state and the previous state as

$$|\Delta\rangle = |\tilde{\psi}(m+1)\rangle - |\psi(m)\rangle \tag{2.12}$$

$$\approx -iA(m)|\psi(m)\rangle$$

where the last line is obtained by making an approximation that the rotation is so small that $e^{-iA(m)}|\psi(m)\rangle \approx |\psi(m)\rangle - iA(m)|\psi(m)\rangle$. Define the original difference as

$$|\Delta_0\rangle = |\psi(m+1)\rangle - |\psi(m)\rangle \tag{2.13}$$

The distance squared between the two states; $f = || \, |\Delta\rangle - |\Delta_0\rangle \, ||^2$ is given by

$$f = f_0 + \frac{i}{\sqrt{c(m+1)}} \langle \Delta_0 | \sum_I a_I \sigma_I |\psi(m)\rangle - \frac{i}{\sqrt{c(m+1)}} \sum_I a_I \langle \psi(m) | \sigma_I^\dagger | \Delta_0 \rangle + \sum_{I,J} a_I a_J \langle \psi(m) | \sigma_I \sigma_J | \psi(m) \rangle \tag{2.14}$$

where the index I, J is used to suppress the index $i_1 i_2 ... i_k$ and $f_0 = \langle \Delta_0 | \Delta_0 \rangle$. To obtain the coefficients, minimize this distance with respect to the coefficients a_I gives

$$(\mathbf{S} + \mathbf{S}^T)\mathbf{x} = \mathbf{b} \tag{2.15}$$

$$S_{I,J} = \langle \psi(m) | \sigma_I \sigma_J | \psi(m) \rangle \tag{2.16}$$

$$b_I = \frac{2}{\sqrt{c(m+1)}} Im \langle \psi(m) | \sigma_I \hat{H} | \psi(m) \rangle \tag{2.17}$$

where x is the vector of the desired coefficients a_I. Solving this system of linear equations requires measurement over the Pauli basis to obtain all the required expectation values as described in Chapter 1.1.

2.3.3 Complexity analysis of QITE

Here, a summary of the complexity analysis presented in [49] is provided. The analysis begin by considering a state $|\Psi\rangle$ with finite correlation length extending over C qubits (that is, correlations between observables separated by distance L that are bounded by $\exp(-L/C)$) and a $k-$local Hamiltonian represented by $\hat{h}_m$. It is argued [49] that the normalized state $e^{-\Delta\tau \hat{h}_m}|\Psi\rangle / ||e^{-\Delta\tau \hat{h}_m}|\Psi\rangle||$ can be generated by a unitary $e^{-i\Delta\tau \hat{A}[m]}$ acting on a domain of width at most $O(C)$ qubits surrounded the qubits acted on by $\hat{h}_m$.

As a result, the unitary can be determined by performing measurements and solving the least squares problem in this domain (Fig. 2.3). For example, for a nearest-neighbor local Hamiltonian on a d-dimension cubic lattice, the domain size D is bounded by $O(C^d)$.

In many physical systems, it is expected that the maximum correlation length throughout the Trotter steps should increase with β and saturate for $C_{\max} \ll N$ [68]. Fig. 2.3 shows the mutual information between qubits i and j as a function of imaginary time in the 1-D and 2-D ferromagnetic transverse field Ising models computed by tensor network simulation, demonstrating a monotonic increase and clear saturation.

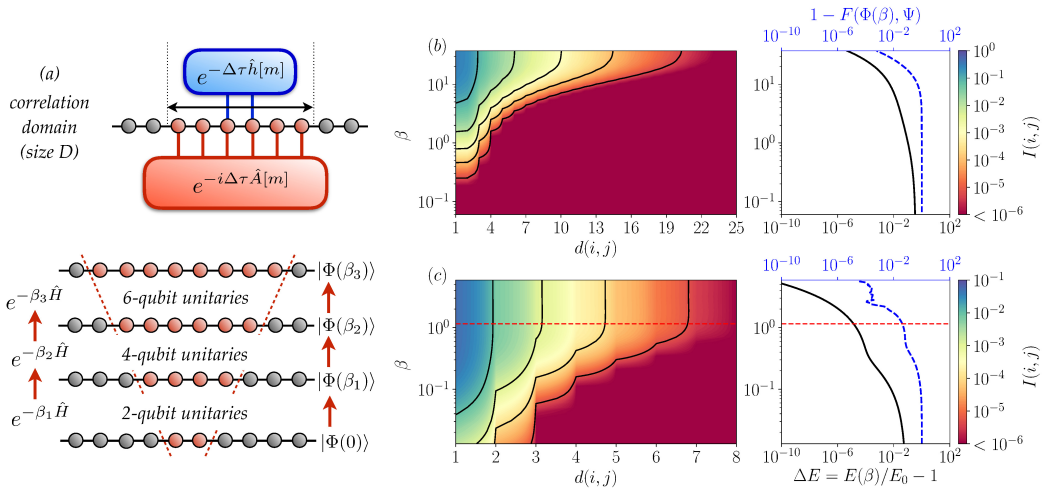

Figure 2.3: **Physical foundations of the quantum imaginary time evolution algorithm.** (a) Schematic of the QITE algorithm. Top: imaginary-time evolution under a geometric k-local operator $\hat{h}[m]$ can be reproduced by a unitary operation acting on $D > k$ qubits. Bottom: exact imaginary-time evolution starting from a product state requires unitaries acting on a domain D that grows with correlations. (b,c) Left: mutual information $I(i, j)$ between qubits i, j as a function of distance $d(i, j)$ and imaginary time β, for a 1-D (b) and a 2D (c) FM transverse-field Ising model, with $h = 1.25$, 50 qubits and $h = 3.5$, 21×31 qubits respectively. $I(i, j)$ saturates at longer times. Right: relative error in the energy ΔE and fidelity $F = |\langle\Phi(\beta)|\Psi\rangle|^2$ between the finite-time state $\Phi(\beta)$ and infinite-time state Ψ as a function of β. The noise in the 2-D fidelity error at large β arises from the approximate nature of the algorithm used. The figure is reproduced from [49].

To thus compare the algorithm with its classical counterpart, it is argued that the number of measurements and classical storage at a given time step (starting propagation from a product state) is bounded by $\exp(O(C^d))$ (with C the correlation length at that time step), since each unitary at that step acts on at most $O(C^d)$ sites; classical solution of the least squares problem has a similar scaling $\exp(O(C^d))$, as does the synthesis and application as a quantum circuit (composed of two-qubit gates) of the unitary $e^{-i\Delta\tau\hat{A}[m]}$. Thus, space and time requirements are bounded by exponentials in C^d, but are polynomial in N when one is interested in a local approximation of the state (the polynomial in N comes from the number of terms in H). Since C saturates, compared with a direct classical implementation of imaginary time evolution, the cost of a QITE time step (for bounded C) is linear in N in space and polynomial in N in time, thus giving an exponential reduction in space and time.

2.3.4 Lanczos algorithm on quantum computer

The Lanczos algorithm is an especially economical realization of a quantum subspace method [69, 70]. The Lanczos algorithm typically converges much more quickly than imaginary time evolution, and often in physical simulations only tens of iterations are needed to converge to good precision. Thus, the implementation of the Lanczos algorithm with QITE [49] offer practical advantages in ground state computation. We present its formulation [49] here.

Starting from a trial wavefunction $|\phi\rangle$, the Lanczos iteration constructs the Hamiltonian matrix $\hat{\mathbf{H}}$ in a successively enlarged Krylov subspace $\{|\phi\rangle, \hat{H}|\phi\rangle, \hat{H}^2|\phi\rangle, ...\}$; diagonalizing $\hat{\mathbf{H}}$ yields an estimate of the ground state energies that practically converges much more quickly than direct imaginary time evolution. In addition, the method provides an estimate of the excited state energies.

The QITE subroutine can be used to construct a quantum analogue of the Lanczos scheme. Starting from a trial wavefunction $|\phi\rangle$, QITE can be used to generate a set of wavefunctions given by

$$\begin{aligned} |\phi_l\rangle &= e^{-l\Delta\tau\hat{H}}|\phi\rangle / || \, e^{-l\Delta\tau\hat{H}}|\phi\rangle \, ||, \quad 0 \leq l < L_{max} \\ &\equiv n_l e^{-l\Delta\tau\hat{H}}|\phi\rangle \end{aligned} \tag{2.18}$$

where n_l is the normalization constant. The matrices $\hat{\mathbf{S}}$ and $\hat{\mathbf{H}}$ are defined with the following matrix elements

$$\hat{S}_{l,l'} = \langle\phi_l|\phi_{l'}\rangle, \quad \hat{H}_{l,l'} = \langle\phi_l|\hat{H}|\phi_{l'}\rangle \tag{2.19}$$

Let $2r = l + l'$, the matrix elements can be expressed as

$$\hat{S}_{l,l'} = \frac{n_l n_{l'}}{n_r^2}, \quad \hat{H}_{l,l'} = \frac{n_l n_{l'}}{n_r^2}\langle\phi_r|H|\phi_r\rangle \tag{2.20}$$

Since the normalization factor n_r can be computed recursively by

$$\frac{1}{n_{r+1}^2} = \frac{\langle\phi_r|e^{-2\Delta\tau\hat{H}}|\phi_r\rangle}{n_r^2} \tag{2.21}$$

the matrices $\hat{S}$ and $\hat{H}$ can be constructed by performing sequential imaginary time steps and storing the energy and norm at each step.

The generalized eigenvalue equation $\hat{\mathbf{H}}\mathbf{x} = E\hat{\mathbf{S}}\mathbf{x}$ can be solved to find an approximation to the ground state $|\phi'\rangle = \sum_l x_l|\phi_l\rangle$ for the ground state. In practice, this eigenvalue equation can be numerically ill-conditioned because S can contain small

and negative eigenvalues for the following reasons: (i) $|\phi_l\rangle$ can become linearly-dependent and (ii) simulations have finite precision as well as noise arising from sampling and hardware imperfections.

To regularize the problem, out of the set of time-evolved states, a well-behaved sequence can be extracted by the following: (i) start from $|\phi_{last}\rangle = |\phi_0\rangle$, (ii) add the next $|\phi_l\rangle$ in the set of time-evolved states s.t. $|\langle\phi_l|\phi_{last}\rangle| < s$, where s is a regularization parameter $0 < s < 1$, (iii) repeat (i) and (ii) by setting $|\phi_{last}\rangle = |\phi_l\rangle$

The generalized eigenvalue equation $\tilde{\mathbf{H}}\mathbf{x} = E\tilde{\mathbf{S}}\mathbf{x}$ spanned by this regularized sequence can then be solved.

2.4 Demonstration of QITE and Lanczos on Aspen-1 quantum processor

In this section, we present the results of our experimental efforts to implement QITE and Lanczos on a superconducting quantum processor to solve the Hamiltonian ground state problem.

2.4.1 Hardware and software

To demonstrate the feasibility of QITE, we conducted proof-of-concept experiments using Rigetti Computing's Aspen-1 quantum processing units (QPUs). The layout of Aspen-1 can be observed in Figure 2.4. For remote interaction with the QPUs, we employed pyQuil [71], an open-source Python library developed by Rigetti Computing. This library provides convenient application programming interfaces (APIs) for defining and executing quantum circuits on the QPUs, as well as retrieving the measurement data obtained during the experiments. Furthermore, pyQuil includes a quantum virtual machine (QVM) emulator capable of simulating the desired circuits and generating synthetic data that emulates the measurement outcomes observed in real-world experiments. Additionally, the library offers APIs for introducing noise to the synthetic data, through specifying various noise models discussed in Chapter 1.5, which will aid in the analysis of the collected data.

2.4.2 Results for one-qubit system

We first report calculations for a single-qubit systm with a Hamiltonian given by

$$\hat{H} = \frac{1}{\sqrt{2}}(X + Z) \tag{2.22}$$

In this case, we start off in the state $|0\rangle$ and the operators $\{X, Y, Z\}$ are needed to construct the QITE operation for each Trotter step. The gate operations are shown in Fig. 2.5.

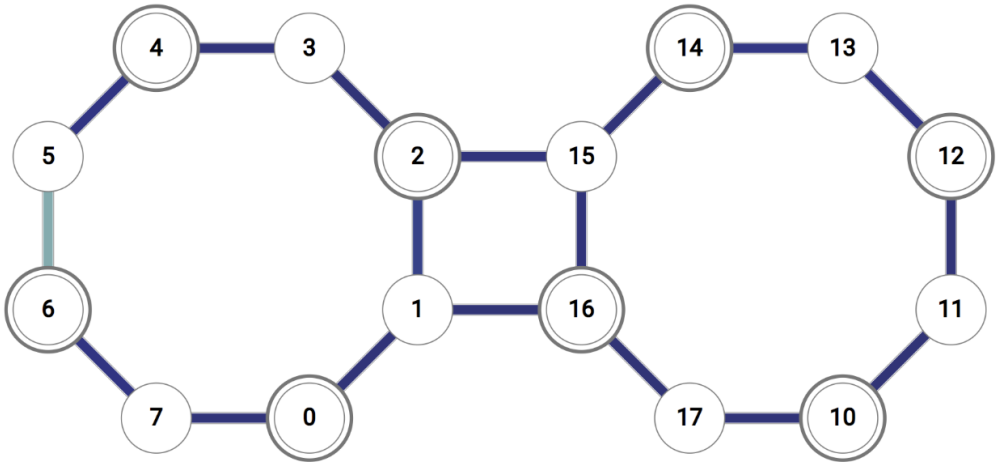

Figure 2.4: **Schematic of the Aspen-1 quantum processing units.** It has 17 qubits in total but not all of them are connected to one other. A line joining a pair of qubits indicates they are connected and a two-qubit operation can be executed on them directly. Figure reproduced from [26].

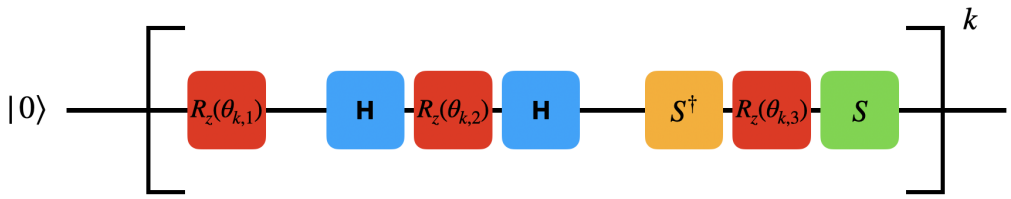

Figure 2.5: **Gate operations to implement QITE for a single qubit system.** The initial step is $|0\rangle$ and each trotter step k is implemented by the unitaries $R_z(\theta_{k,1}$, $R_x(\theta_{k,2}$, and $R_y(\theta_{k,3}$.

We executed the QITE algorithm using the QVM with a readout (RO) noise model, as described in Chapter 1.5.2. We plot the energy $E(\beta)$ as a function of the imaginary time β in Fig. 2.6. We observe that the energy converges to -0.91, which is larger than the exact value of -1.0. Promisingly, by implementing RO mitigation as described in Chapter 1.6.1, our energy converges to the exact value.

Next, we demonstrate the QITE and Lanczos algorithms on the Aspen-1 quantum processing unit. Fig. 2.7 presents the energy $E(\beta)$ plotted against the imaginary time β. Even with RO mitigation, the energy converges to -1.05, which is slightly lower than the exact value of -1.0. The additional error can be attributed to other hardware imperfections, as discussed in Chapter 1.5. Nevertheless, the relative error, computed as $|E(\beta = 3.0) - E_{\text{exact}}|/E_{\text{exact}} \times 100$, is only 5%, indicating a relatively small deviation. Consequently, these results provide compelling evidence

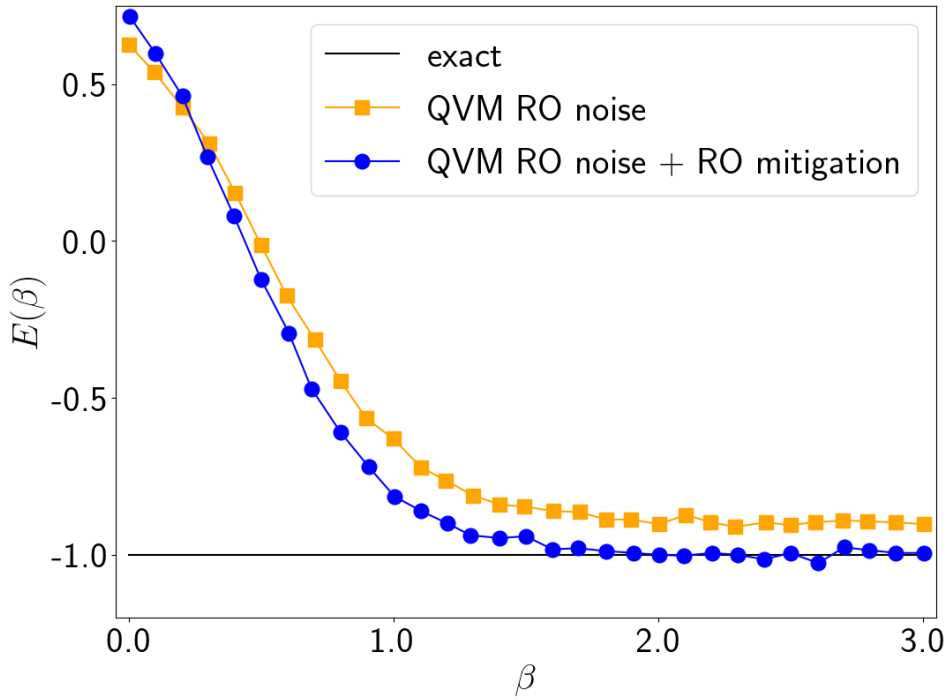

Figure 2.6: **Emulation of QITE algorithm for 1 qubit system with readout (RO) noise.** Energy $E(\beta)$ as a function of the imaginary time β. With RO noise, the energy converges to -0.91, which is larger than the exact value of -1.0. By applying RO mitigation, the energy converges to the exact value. The readout transition matrix $A_{0,0} = 0.95, A_{0,1} = 0.05, A_{1,0} = 0.05, A_{1,1} = 0.95$ and trotter step size $d\tau = 0.1$ are used for the calculations. 100000 measurements are used to determine the expectation values of each observable.

for the reliable execution of QITE on NISQ devices.

Furthermore, our data reveals that the Lanczos algorithm exhibits a faster convergence rate. The Lanczos algorithm achieves convergence in just 6 Trotter steps, whereas the QITE algorithm requires 10 Trotter steps. This demonstrates the potential of employing Lanczos to accelerate calculations for the Hamiltonian ground state problem.

2.4.3 Results for two-qubit system

We next report calculations for a two-qubit tranverse-field Ising model (TFIM) with the Hamiltonian given by

$$H = -J \sum_{i=0}^{N-1} Z_i Z_{i+1} + h \sum_{i=0}^{N} X_i \tag{2.23}$$

where $J = 1$ and $h = 1$. In particular, we focus on the case where $N = 2$ and start off in the state $|00\rangle$. To construct the QITE operation at each Trotter step, we need

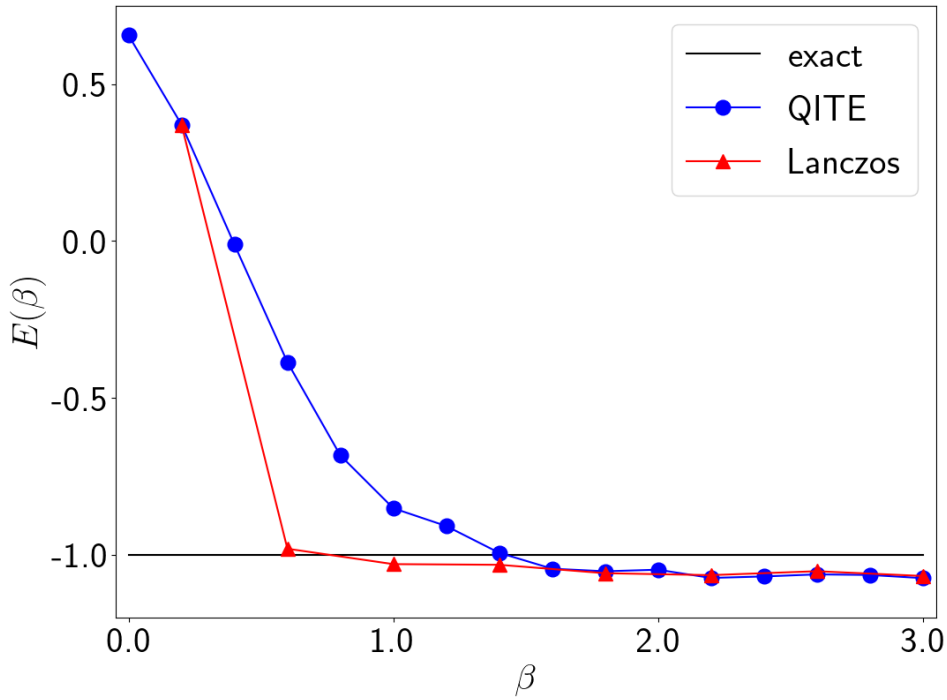

Figure 2.7: **Demonstration of QITE algorithm for 1 qubit system on Aspen-1.** Energy $E(\beta)$ as a function of the imaginary time β. The energy converges to -1.05 which is smaller than the exact value of -1.0 and the relative error, defined by $|E(\beta = 3.0) - E_{exact}|/E_{exact} \times 100$ is 5%. The QITE and Lanczos algorithms converges after 10 and 6 Trotter steps respectively. Our data demonstrates that QITE and Lanczos can run reliably on NISQ devices. The trotter step size $d\tau = 0.2$ are used for the QITE and Lanczos algorithms. 100000 measurements are used to determine the expectation values of each observable. The regularization parameters $s = 0.75$ and $\epsilon = 10^{-2}$ were used for the Lanczos algorithm.

the following 15 operators: $\{X_0, Y_0, Z_0, X_1, Y_1, Z_1, X_0X_1, X_0Y_1, X_0Z_1, Y_0X_1, Y_0Y_1, Y_0Z_1, Z_0X_1, Z_0Y_1, Z_0Z_1\}$. The gate operations can be implemented as discussed in Chapter 1.3.

We begin by showcasing representative runs of the QITE algorithm for the two-qubit system on Aspen-1. Fig. 2.8 displays the energy $E(\beta)$ plotted against the imaginary time β. It is evident that there are substantial variations in the trajectories across different runs, likely attributable to hardware imperfections as previously mentioned. Furthermore, the energy converges to -1.22 in the more accurate run, deviating from the exact value of -1.581. The resulting relative error of 20 % is larger compared to the data obtained from the single-qubit experiment. This larger error can be attributed to the use of a greater number of gates and, more significantly, the inclusion of two-qubit gates, which exhibit higher error rates when compared to

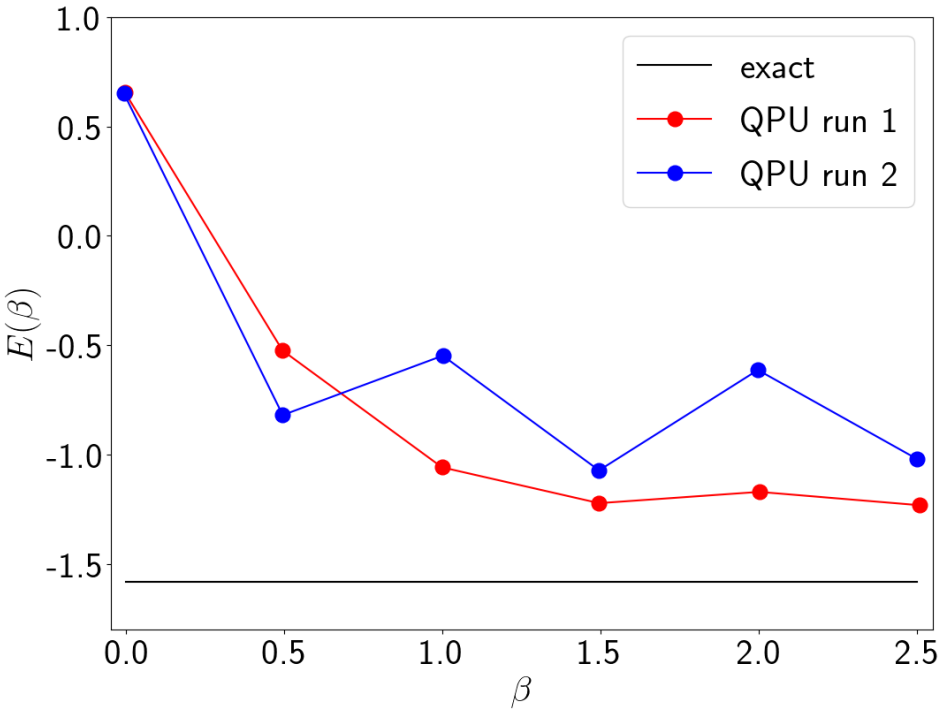

Figure 2.8: **Representative quantum processing unit (QPU) runs for two-qubit system.** Energy $E(\beta)$ as a function of the imaginary time β. We see huge variations from run-to-run. In addition, the energy of run 1 converges to -1.22 which is larger than the exact value of -1.581 and the relative error, defined by $|E(\beta = 2.5) - E_{exact}|/E_{exact} \times 100$ is 20%. This is much larger compared to the results for the single-qubit case likely due to the fact that two-qubit gates have a much high error rate compared to the single-qubit gates. The trotter step size $d\tau = 0.5$ are used for the QITE algorithms. 100000 samples are used to determine the expectation values of each observable.

single-qubit gates.

To investigate the impact of noise on the results for the two-qubit system, we conduct noisy emulations using the quantum channels introduced in Chapter 1.5 via the QVM. In these emulations, we employ the following noise parameters

- noise model 1

  $A_{00} = 0.95,\ A_{01} = 0.05$ $\quad$ $A_{11} = 0.95,\ A_{10} = 0.05$

  $T_1 = 10.5\,\mu s$ $\quad$ $T_2 = 14.0\,\mu s$

  $p_1 = 0.001$ $\quad$ $p_2 = 0.01$

where p_1 and p_2 are the single-qubit and two-qubit depolarizing probability, T_1 is the relaxation time that characterizes the amplitude damping channel since $p_a = e^{T_1/T_{gate}}$

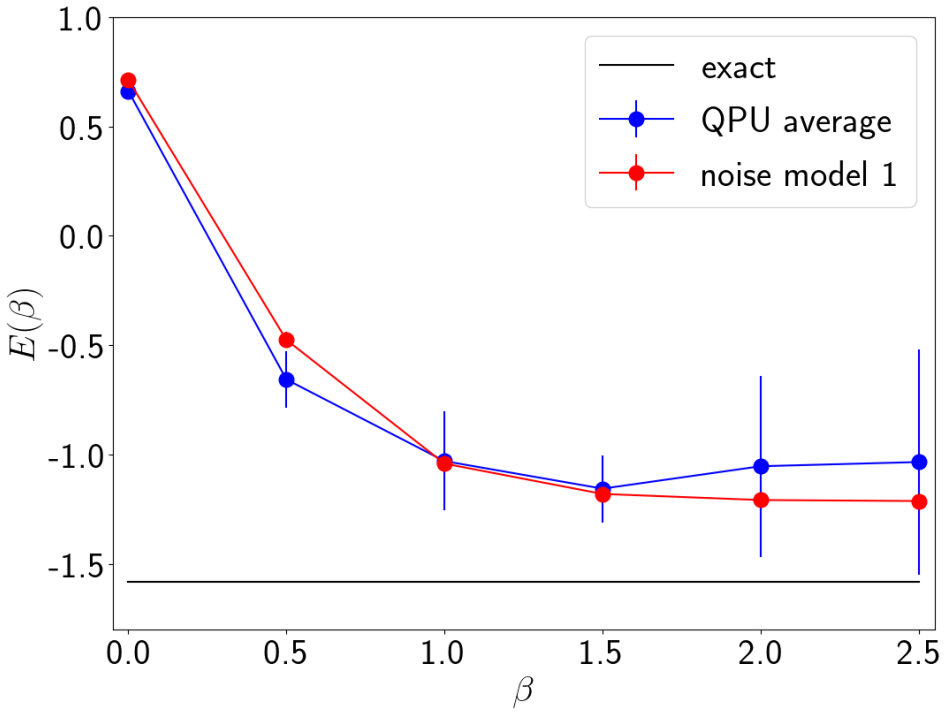

Figure 2.9: **Comparison of data collected from QPU and noisy emulation.** Energy $E(\beta)$ as a function of the imaginary time β. We collected data from 10 runs on the QPU and show the average and mean. The noisy emulation using the parameters defined in noise model 1 is able to reproduce the systematic shift in the converged energy. A trotter step of $d\tau = 0.5$ is used for the QITE algorithm. 100000 measurements are used to determine the expectation values of each observable.

where T_{gate} is the actual gate time and, T_2 is the coherence time that characterizes the dephasing channel since $p_d = e^{T_2/T_{gate}}$.

We obtained data from 10 runs on the QPU, and plot the mean and standard deviation of the energy with respect to imaginary in Fig. 2.9. We also plot the data generated by the noisy emulation using noise model 1 for comparison. Our noisy emulation successfully replicates the systematic shift observed in the QPU data. The remaining discrepancies are likely attributable to cross-talk noise, which is not accounted for in our noise model.

To explore the influence of reduced noise on the 2-qubit results, we introduce a different set of noise parameters.

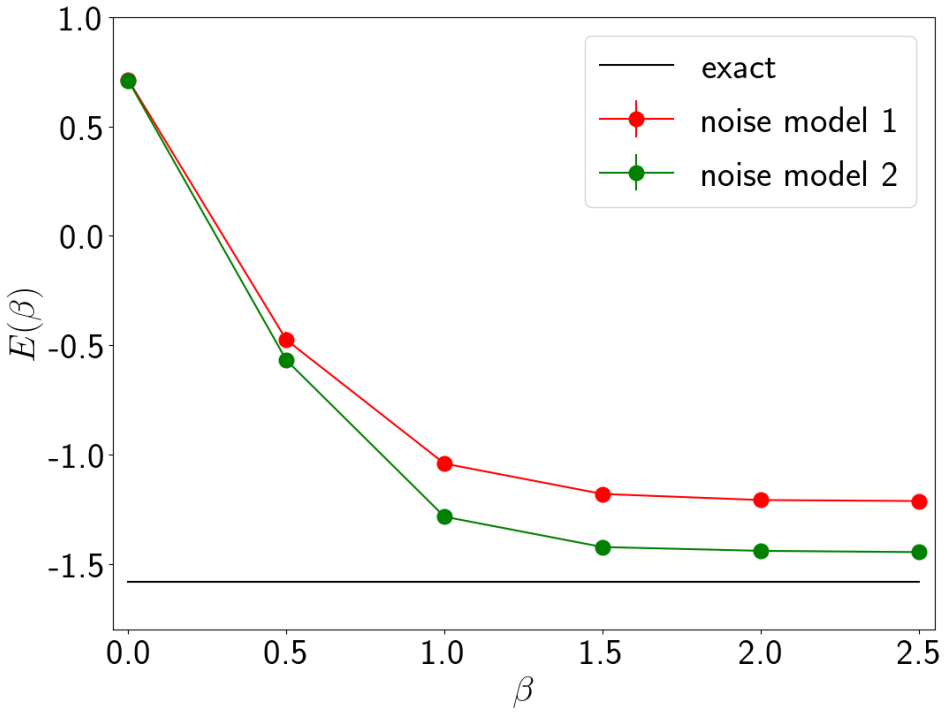

Figure 2.10: **Comparison of noisy emulations using different noise parameters.** Energy $E(\beta)$ as a function of the imaginary time β. The energy converges to -1.22 and -1.44 when noise model 1 and noise model 2 are used respectively. Comparing this to the exact value of -1.581, the results highlight that a modest improvement in the quality of qubit is needed for QITE to run reliably for larger systems. A trotter step of $d\tau = 0.5$ is used for the QITE algorithm. 100000 measurements are used to determine the expectation values of each observable.

- noise model 2

  $A_{00} = 0.99,\ A_{01} = 0.01$ $\quad$ $A_{11} = 0.99,\ A_{10} = 0.01$

  $T_1 = 20.0\,\mu s$ $\quad$ $T_2 = 40.0\,\mu s$

  $p_1 = 0.0001$ $\quad$ $p_2 = 0.001$

We compare the data generated using two different noise models and investigate the impact on the converged energy. Fig. 2.10 displays the energy $E(\beta)$ as a function of the imaginary time β. Notably, we observe a significant improvement in the converged energy when using noise model 3, with the energy converging to -1.44. This is in contrast to the energy convergence of -1.21 observed with noise model 1. The energy obtained with noise model 3 is closer to the exact value of -1.58, indicating that a moderate improvement in qubit quality can lead to more accurate results for larger system sizes.

Furthermore, in order to gain insights into the impact of differences in the quality

factor of qubits on the overall performance of the QITE algorithm, we conducted experiments using two different pairs of qubits, referred to as Pair 1 and Pair 2. These qubit pairs are characterized by distinct quality factors, which are detailed in Table 2.1.

name	fRO	f1Q	fCZ
Pair 1	0.96	0.97	0.92
Pair 2	0.89	0.95	0.89

Table 2.1: Parameters for different qubit pairs. fRO, f1Q and fCZ are the average fidelities of the readout, single-qubit gate and two-qubit gate for each pair of qubits.

We averaged the data from 10 runs conducted on Pair 1 and Pair 2, and plotted the mean and standard deviation of the energy as a function of imaginary time in Fig. 2.11. Notably, we observed a significant improvement in the converged energies when utilizing qubits with higher quality factors. These findings further support the notion that QITE can reliably handle larger system sizes if there is a moderate improvement in qubit quality.

In conclusion, our experimental runs, which included data from both actual hardware and the emulator, have demonstrated the potential of QITE in effectively solving the Hamiltonian ground state problem.

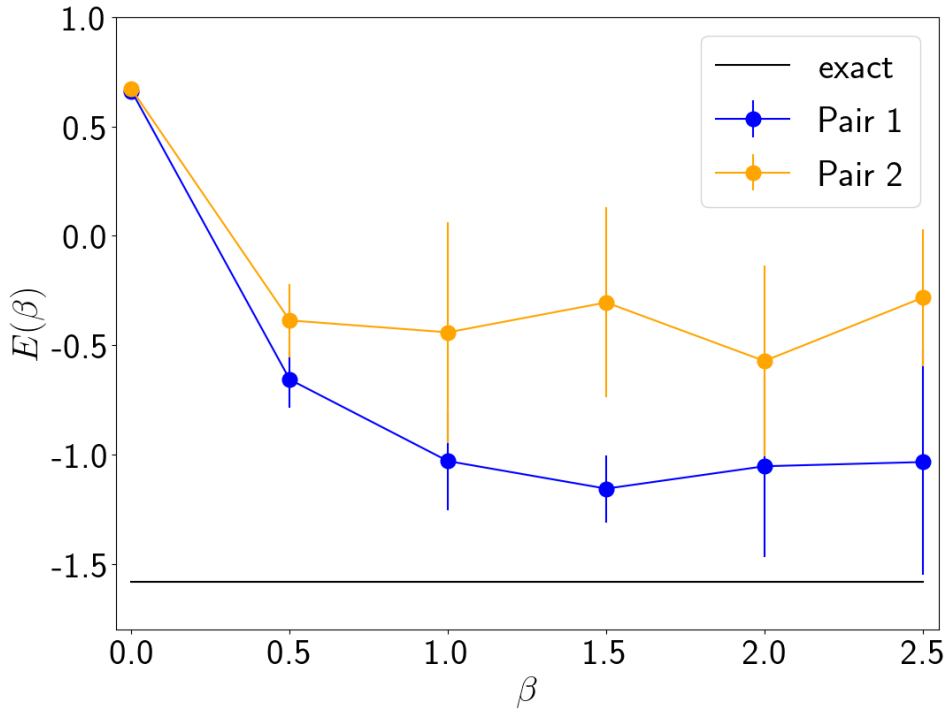

Figure 2.11: **Comparison of QITE on different pairs of qubits on the QPU.** Energy $E(\beta)$ as a function of the imaginary time β. 10 different runs were collected from each pair and their mean and standard deviation plotted. The energies converged to -1.04 and -0.4 for data collected from Pair 1 and Pair 2 respectively. Comparing this to the exact value of -1.581, the data validates that only a modest improvement in the quality of qubit is needed for QITE to run reliably for larger system. A trotter step of $d\tau = 0.5$ is used for the QITE algorithm. 100000 measurements are used to determine the expectation values of each observable.

2.5 Comparison between QITE and VQE

To gain an insight into the performance differences between QITE and VQE, we conducted a comparison based on the total number of Pauli string measurements required to obtain the ground state for two distinct spin models. The first model considered was a 1-D Heisenberg chain in a magnetic field, represented by the Hamiltonian

$$\hat{H} = J \sum_{i}^{N-1} (X_i X_{i+1} + Y_i Y_{i+1} + Z_i Z_{i+1}) + B \sum_{i}^{N} Z_i \tag{2.24}$$

where the parameters $J = B = 1$; the 4-site instance of this model was studied in Ref. [63]. We also study (b) the 1-D transverse-field Ising model given in Eqn. 2.23. Specifically, we performed an estimation of the total number of Pauli string

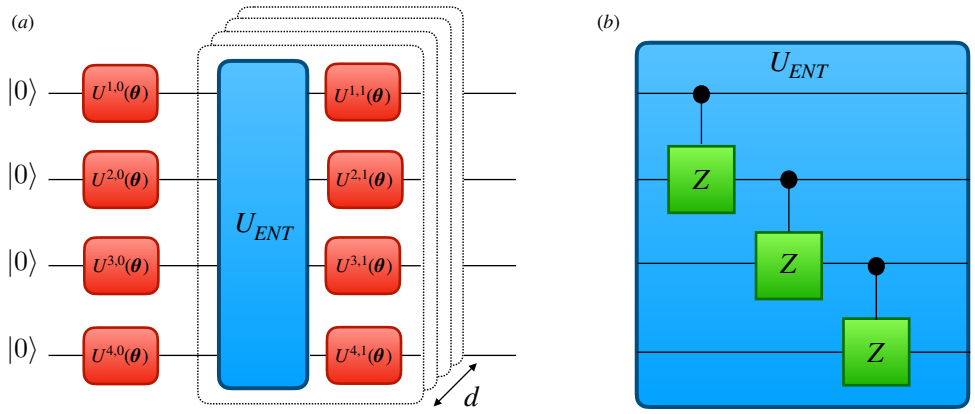

Figure 2.12: **Schematic of VQE ansatz used.** (**a**) VQE Ansatz that is composed of a sequence of interleaved single-qubit rotations $U^{q,i}(\boldsymbol{\theta})$ and entangling operations. (**b**) The entangling operations consist of applying CZ gates between nearest neighbours.

measurements required to obtain the ground state of a 4-site and 6-site instance of the two models. We considered the state to have converged to the ground state if its energy was within a certain threshold (1% or 2%) of the exact ground state energy. By comparing the total number of Pauli string measurements in VQE and QITE, we can gain insights into their respective measurement requirements for obtaining the ground state of the spin models.

2.5.1 Counting Pauli strings in VQE

To perform the VQE calculations, we used the hardware-efficient variational Ansatz as described in [63]. This consists of first applying rotation unitaries represented by $U^{q,i}(\boldsymbol{\theta}) = Rz_{\theta_1^{q,i}} Rx_{\theta_2^{q,i}} Rz_{\theta_3^{q,i}}$ to all qubits before applying layers of a certain depth d; each layer begins by applying CZ gates between nearest-neighbors followed by applying $U^{q,i}(\boldsymbol{\theta}) = Rz_{\theta_1^{q,i}} Rx_{\theta_2^{q,i}} Rz_{\theta_3^{q,i}}$ to all qubits again. Details of the circuit can be seen in Fig. 2.12.

As in [63], we also used the simultaneous perturbation stochastic approximation (SPSA) algorithm as the optimization protocol. The SPSA algorithm is commonly used because (i) it performs well in the presence of stochastic fluctuations and (ii) it requires only evaluating the objective function twice to update the variational parameters regardless of the number of parameters involved. The performance of the optimizer depends on the hyperparameters α and γ as described in [63] and we found that their reported values of $\alpha = 0.602$ and $\gamma = 0.101$ also gave the best

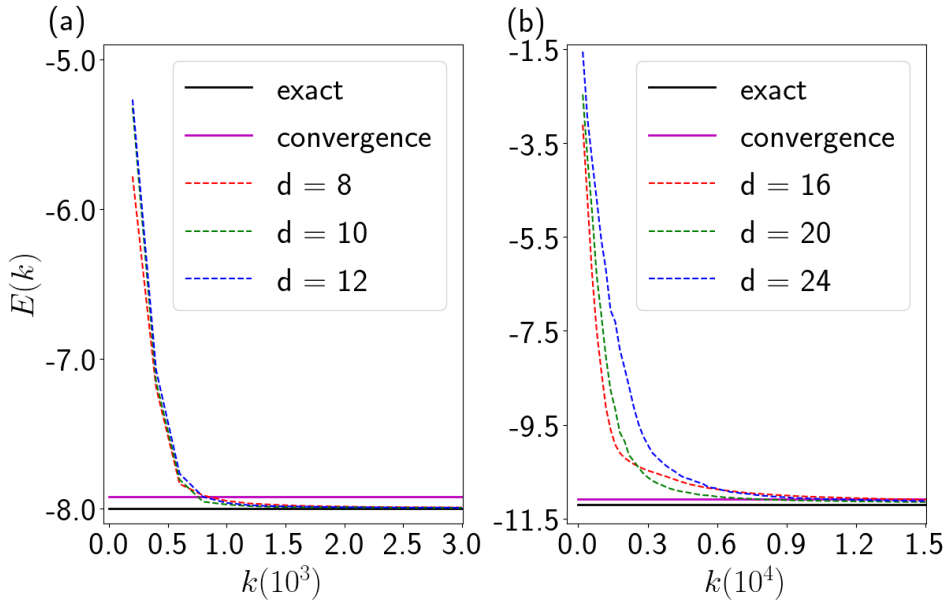

Figure 2.13: **Convergence plot for VQE emulations.** VQE calculations for (**a**) 4-site and (**b**) 6-site 1-D Heisenberg model. k is the number of optimization steps.

results for us. Numerical evidence of this is provided later on.

Evaluating the objective function involves estimating the expectation value of the Pauli strings that appear in the Hamiltonian. To prevent sampling errors from influencing the comparison, we evaluated the expectation values exactly. We conducted the VQE calculations using Qiskit [72], a quantum emulator Python package provided by IBM. The package provides both the SPSA algorithm and a variational Ansatz which we modified to reproduce the exact Ansatz used in [63].

To count the number of Pauli strings needed for convergence, we ran VQE using different layer depths and determined the number of iterations N needed for the algorithm to converge to a state with an energy within a certain percentage (1% or 2%) of the exact ground state energy. Examples of converged VQE calculations for the 1-D Heisenberg model are given in Fig. 2.13. In each iteration, the objective function was evaluated twice, and the evaluation of the objective function required measuring the expectation value of the M Pauli strings that appear in the Hamiltonian. Therefore, the total number of Pauli strings P_{total} is given as

$$P_{total} = 2 \times N \times M \tag{2.25}$$

It should be noted that the results obtained from different VQE trajectories may exhibit slight variations. To mitigate this, we performed 10 trajectories in our VQE

calculations and analyzed the data by considering the average trajectory. In Table 2.2, we summarize the VQE parameters that yielded the lowest total number of Pauli measurements required to converge to the ground state. For the 6-site 1-D antiferromagnetic (AFM) transverse field Ising model, VQE could not achieve convergence within 1%, and therefore, we used a 2% convergence criterion instead.

For the 6-site 1-D Heisenberg model, our simulation results indicated that using $\alpha = 0.602$ and $\gamma = 0.101$ with a circuit depth of 20 resulted in the lowest total number of Pauli measurements. We further conducted tests to identify the optimal values of α and γ for the 6-site 1-D Heisenberg model. The VQE calculation with $\alpha = 0.602$, $\gamma = 0.101$, and a circuit depth of 20 converged within 8400 optimization steps. We performed additional VQE calculations for different values of α and γ, keeping the circuit depth at 20 and a total of 9000 optimization steps. The data presented in Table 2.3 clearly demonstrates that $\alpha = 0.602$ and $\gamma = 0.101$ yielded the best result in our case.

Table 2.2: VQE simulation parameters for (a) 1-D Heisenberg with applied field and (b) 1-D transverse field Ising. Conv. refers to the convergence criterion used. We note for the last case, the VQE optimization could not reach within 1% of the ground state energy, so we set the convergence criterion to 2 %

model	n-site	conv.	α	γ	d	N	P_{total}
a	4	1%	0.602	0.101	8	800	25,600
a	6	1%	0.602	0.101	20	8400	403,200
b	4	1%	0.602	0.101	12	800	12,800
b	6	2%	0.602	0.101	12	2890	69,360

Table 2.3: Hyperparameters sweep for 6-site 1-D Heisenberg model using a circuit depth of 20 for a total of 9000 optimization steps. The step at which the calculation converged is recorded under column T. '-' indicates that VQE failed to converge.

α	γ	T
0.400	0.066	-
0.400	0.101	-
0.400	0.133	-
0.602	0.066	-
0.602	0.101	8400
0.602	0.133	8800
0.800	0.066	-
0.800	0.101	-
0.800	0.133	-

2.5.2 Counting Pauli strings in QITE

To implement QITE, we used the second-order Trotter decomposition given by

$$e^{-\beta\hat{H}} = (e^{-\Delta\tau/2\hat{h}[1]} \dots e^{-\Delta\tau/2\hat{h}[K-1]} e^{-\Delta\tau\hat{h}[K]} \\ e^{-\Delta\tau/2\hat{h}[K-1]} \dots e^{-\Delta\tau\hat{h}[1]})^n + O\left(\Delta\tau^2\right);\ n = \frac{\beta}{\Delta\tau} \tag{2.26}$$

to carry out the real time evolution. We initialized our state as: (a) $|0101\dots\rangle$ for the 1-D Heisenberg model and (b) maximally-mixed state for the 1-D AFM transverse-field Ising model. We converged to the ground state using a time step of $\Delta\tau = 0.1$ and a domain size D of 4, as seen in Figs. 2.14. To count the number of Pauli strings, we note that a domain size of 4 implies that to evaluate $e^{-\Delta\tau/2\hat{h}[i]}$ involves measuring $4^4 = 256$ Pauli strings (without using the real-valued nature of the Hamiltonian). Therefore, with a total number of Trotter steps T, the total number of Pauli strings P_{total} is given as

$$P_{total} = (2K-1) \times T \times 256 \tag{2.27}$$

where K is a multiplicative factor that depends on the size of the system. We summarize the parameters that we used for QITE to obtain the ground state in table 2.4. We had no trouble converging our ground state to arbitrary accuracy using QITE but we used the same convergence criterion as for VQE to facilitate comparison.

Table 2.4: QITE simulation parameters for (a) 1-D Heisenberg with applied field and (b) 1-D transverse-field Ising. Conv. indicates the convergence criterion used. We used 2% for the final calculation to facilitate comparison with VQE which failed to converge to within 1%.

model	n-site	conv.	$\Delta\tau$	D	T	K	P_{total}
a	4	1%	0.1	4	7	4	12,544
a	6	1%	0.1	4	17	6	47,872
b	4	1%	0.2	4	7	4	12,544
b	6	2%	0.2	4	8	6	22,528

2.5.3 Resource comparison

We plot the number of Pauli string expectation values with respect to system size in Fig. 2.14 for the (a) 1-D Heisenberg and (b) 1-D TFIM models. Our data suggests that QITE is competitive with VQE with respect to the number of Pauli string measurements. In fact, for the 6 qubit system, the number of measurements needed in QITE was significantly less than in VQE, due largely to the SPSA iterations needed to reach convergence when optimizing the VQE energy. While it is likely

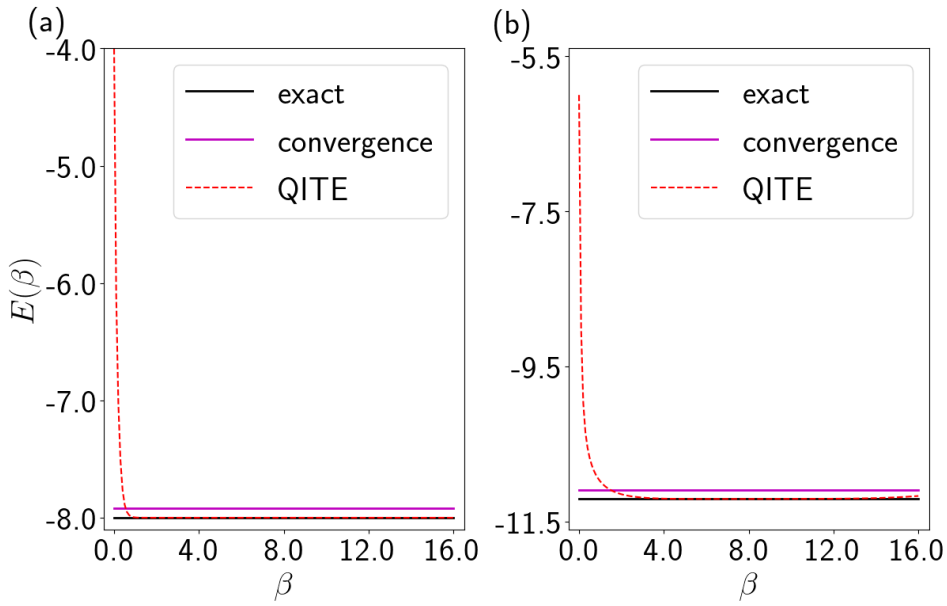

Figure 2.14: **Convergence plot for QITE emulation.** QITE calculations for (**a**) 4-site and (**b**) 6-site for the 1-D Heisenberg model. A trotter step of $\Delta tau = 0.2$ and a domain size of 4 are used for the calculations. A total of 7 and 8 Trotter steps are used for the calculations performed in (**a**) and (**b**) respectively.

that the VQE costs could be lowered by using a better optimizer, or a better VQE Ansatz, we also note that the counts for QITE can also be reduced by using the methods outlined in [49]. The widespread current implementation of VQE and the observed performance of QITE suggest that it will be practical to implement the QITE protocol for intermediate system sizes on near-term devices.

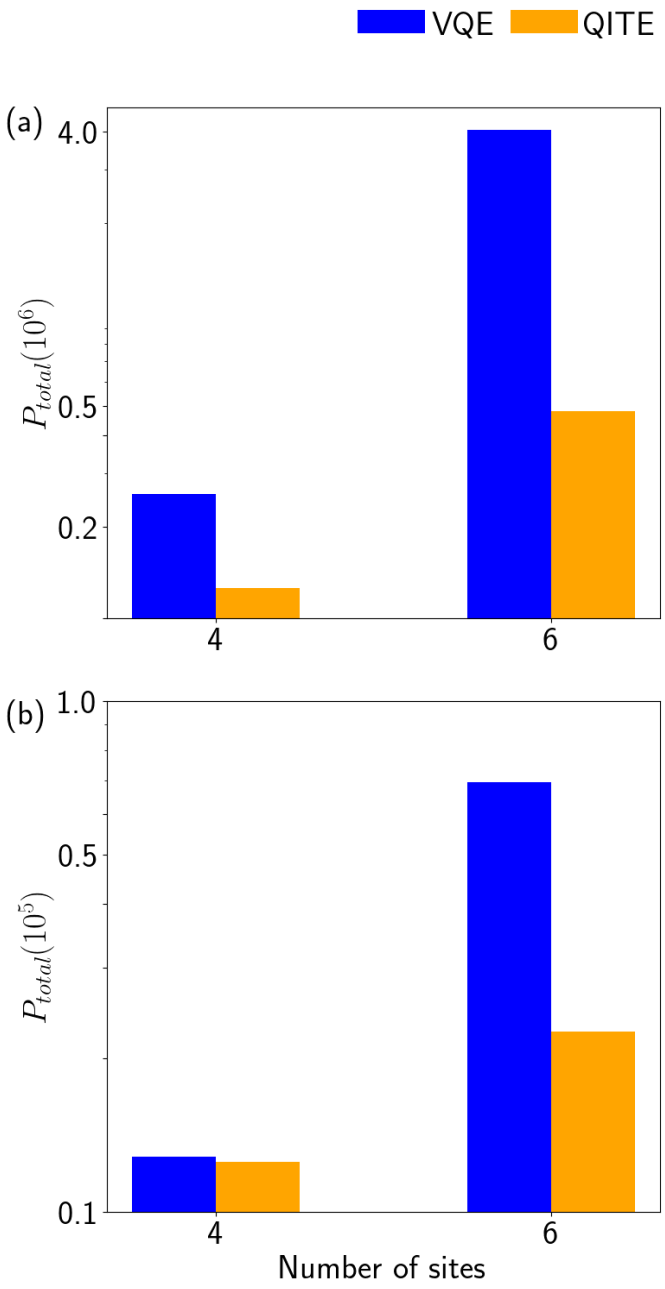

Figure 2.15: **QITE and VQE resource comparison.** Estimate of the number of Pauli string expectation values (P_{total}) needed for QITE and VQE to converge for the (**a**) 1-D Heisenberg model with magnetic field, and (**b**) 1-D TFIM model. QITE is competitive with VQE for the 4-site model and requires significantly fewer measurements in the 6-site model. While the number of measurements could potentially be reduced in VQE by different optimizers and ansatz, the data suggests that QITE is a promising alternative to VQE on near-term devices.

2.6 Conclusion

In conclusion, we have presented our efforts to implement the quantum analogs of imaginary-time evolution and Lanczos schemes on present quantum hardware. These methods offer several advantages, such as eliminating the need for ancillae or deep circuits required in quantum phase estimation and avoiding complex optimization problems commonly encountered in variational approaches. Hence, their experimental validation is a crucial task in advancing the state of Hamiltonian ground state computation on NISQ devices.

Through experimental demonstrations on Rigetti's Aspen-1 superconducting quantum processors and the provided emulators, we have established the feasibility of implementing these algorithms on NISQ devices for performing ground state simulations. Finally, our results indicate that QITE can compete favorably with VQE in terms of the number of Pauli string expectation values required.

Overall, our research contributes valuable insights into the capabilities and potential applications of these methods in the context of quantum simulation. It sets the stage for further advancements and investigations, paving the way for future breakthroughs in utilizing gate-based quantum computing to surpass classical computing in Hamiltonian ground state simulations.

Chapter 3

FINITE TEMPERATURE SIMULATION USING QITE

The work in this chapter related with sampling minimally entangled thermal states has been adapted, in part, from:

1. Motta, M., Sun, C., **Tan, Adrian T. K.**, O'Rourke, M. J., Ye, E., *et al.* Determining eigenstates and thermal states on a quantum computer using quantum imaginary time evolution. *Nat. Phys.* ISSN: 1745-2481. https://doi.org/10.1038/s41567-019-0704-4 (2019).

   Contributions A.T.K.T. designed the quantum circuits to execute the algorithms, carried out the simulation runs on the quantum computers, performed simulations and analyzed the experimental data, and contributed to the writing of the manuscript.

The work in this chapter related to computing free energies has been adapted from unpublished work carried out during the course of the author's graduate studies.

The investigation of finite temperature effects is of great significance in the fields of chemistry and condensed matter physics as it sheds light on various intriguing phenomena, including high-temperature superconductivity, which still eludes a detailed understanding and spans a substantial portion of the finite temperature phase diagram [73].

Nevertheless, the utilization of circuit-based quantum computers for conducting finite temperature simulations still poses challenges. Although several theoretical proposals have been put forth for performing thermal simulations on quantum computers, the complexity of the quantum circuits involved has hindered their implementation on NISQ devices.

In this chapter, we present two distinct yet interconnected projects that demonstrate the implementation of finite temperature simulations on NISQ devices. One key objective in such simulations is the computation of thermal averages. In the first project, we demonstrate how the quantum imaginary time evolution can be used to sample minimally entangled typical thermal states (METTS) on a quantum computer to compute the desired thermal averages. This routine, referred to as QMETTS, was

successfully implemented on Rigetti's Aspen-1 quantum processor unit, marking the first demonstration of performing finite temperature simulations using quantum processors.

In quantum statistical mechanics, the free energy F is a valuable quantity for understanding thermodynamic properties. In the next project, we employ QITE to determine the free energy by computing the partition function Z of a system. We validate the feasibility of our algorithm by running it on the IBM Bogota quantum processor. Our approach involves a sum with exponential number of terms, and we propose an alternative method supported by numerical evidence of its viability.

Overall, our findings highlight the significant potential of quantum computation in the domain of finite temperature simulations. These results pave the way for exciting opportunities and avenues for further exploration and advancement in this area.

3.1 Quantum minimally entangled thermal typical states (QMETTS)

3.1.1 Background

In the context of finite temperature simulations, a key objective is to compute thermal averages of observables A for the Gibbs ensemble $\rho_{th} = e^{-\beta \hat{H}}$, where $\hat{H}$ represents the Hamiltonian of interest. Specifically, we aim to calculate averages of the form

$$\begin{aligned} \langle \hat{A} \rangle_{th} &= \mathrm{Tr}[\rho_{th} A]/\mathrm{Tr}[\rho_{th}] \\ &= Z^{-1}\mathrm{Tr}[\rho_{th}\hat{A}], \quad Z = \mathrm{Tr}[e^{-\beta \hat{H}}] \end{aligned} \tag{3.1}$$

where Z denotes the partition function and $\hat{A}$ represents the observable of interest. Previous methodologies have proposed protocols to compute these thermal averages by either preparing the Gibbs ensemble [74–76] or utilizing Metropolis sampling [77, 78]. However, these approaches require quantum phase estimation as a subroutine, resulting in circuit depths that render them infeasible for NISQ devices (as discussed in Chapter 1.2). Consequently, it is imperative to explore alternative strategies that involve fewer quantum gate operations to enable thermal calculations on NISQ devices.

3.1.2 Minimally entangled typical thermal states

We present a workflow that has been introduced by our collaborators [49] to adapt a classical protocol that samples the minimally entangled typical thermal states (METTS) [79] into a feasible implementation on a quantum computer.

The original METTS algorithm computes thermal averages by sampling from states that are "typical" of a finite temperature system [79]. To see this, Eqn. 3.1 can be rewritten as

$$\begin{aligned}\langle A\rangle_{th} &= Z^{-1}\mathrm{Tr}[\rho_{th}A] \\ &= \mathrm{Z}^{-1}\mathrm{Tr}[e^{-\beta\hat{H}/2}Ae^{-\beta\hat{H}/2}] \\ &= \mathrm{Z}^{-1}\sum_i \langle i|[e^{-\beta\hat{H}/2}Ae^{-\beta\hat{H}/2}|i\rangle \\ &= \mathrm{Z}^{-1}\sum_i p(i)\langle\phi(i)|A|\phi(i)\rangle \end{aligned} \tag{3.2}$$

where $\{|i\rangle\}$ is some orthonormal basis, $p(i) = \langle i|e^{-\beta\hat{H}}|i\rangle$ and the new states $|\phi(i)\rangle$ defined as

$$|\phi(i)\rangle = p(i)^{-1/2}e^{-\beta\hat{H}/2}|i\rangle \tag{3.3}$$

are considered the "typical" states of the thermal system. The sum in Eqn. 3.2 can be estimated by the following:

1. Start from some orthonormal basis $\{|i\rangle\}$. A simple choice will be the product states, i.e. $|i_0\rangle \otimes ... \otimes |i_k\rangle$, $k \in \{0, 1\}$.
2. Compute the METTS wavefunction $|\phi(i)\rangle$ and the observable $\langle\phi(i)|A|\phi(i)\rangle$.
3. Repeat 1. and 2. with a new product state $|i'\rangle$ that is sampled from $|\phi(i)\rangle$ with the probability $p(i \to i') = |\langle i'|\phi(i)\rangle|^2$

Stoudenmire et. al [79] have shown that the procedure above indeed samples from a valid distribution, and in fact, reconstruct observables sampled from the Gibbs distribution.

To sample METTS on a quantum computer, the following protocol is proposed:

1. Start from a state sampled from the computational basis, i.e. $|i\rangle = |i_0\rangle \otimes ... \otimes |i_k\rangle$, $i \in \{0, 1\}$.
2. Prepare the METTS $|\phi(i)\rangle$ on the quantum computer using QITE and measure the desired observables.
3. Prepare the METTS $|\phi(i)\rangle$ again and perform a measurement in the Z-basis to determine $|i'\rangle$ and repeat 1-3.

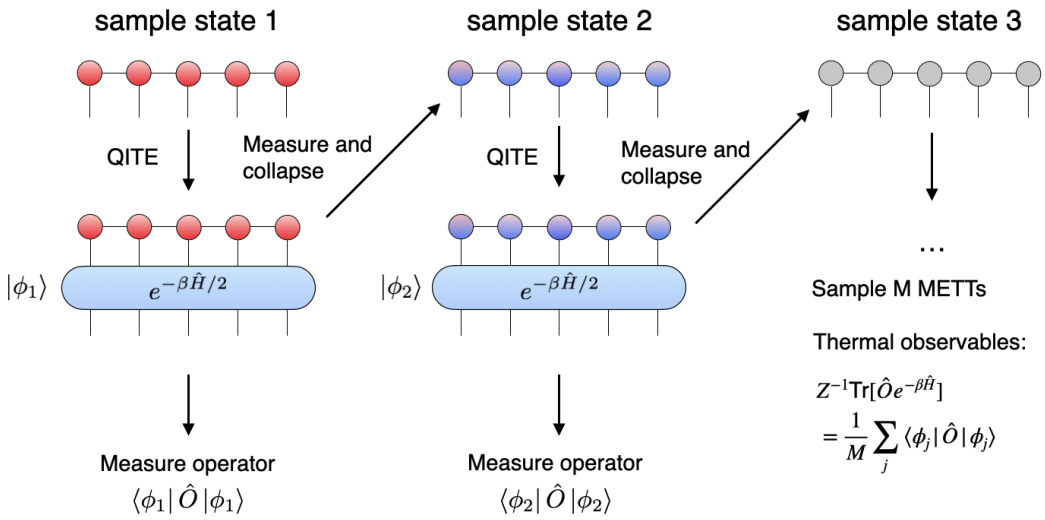

Figure 3.1: **Workflow to sample METTS on a quantum computer.** To compute the thermal observables $Z^{-1}\mathrm{Tr}[\hat{O}e^{-\beta\hat{H}}]$, the METTS state can be sampled on a quantum computer. This is done by first choosing a computational basis state $|i\rangle$ randomly, and using QITE to generate the state $|\phi_1\rangle e^{-\beta\hat{H}/2}|i\rangle$. The expectation value $\langle\phi_1|\hat{O}|\phi_1\rangle$ is measured and then a new basis state is chosen by measuring $|\phi_1\rangle$ in the z-basis. The whole process is repeated M times. The thermal observables can approximated as $\frac{1}{M}\sum_i\langle\phi_i|\hat{O}|\phi_i\rangle$.

The measurement in 3. naturally picks a product state with the correct distribution, i.e., $p(i) = |\langle i|\phi(i)\rangle|^2$. The entire workflow is called QMETTS and the proposed routine is illustrated in Fig. 3.1.

3.1.3 Demonstration of QMETTS on Aspen-1 quantum processor

In this section, we present our efforts to validate the QMETTS workflow on existing quantum hardware. In our experimental studies, we conducted the algorithm on Rigetti Computing's Aspen-1 quantum processing units (QPUs), which was introduced earlier in Chapter 2.4.1. To interface with the QPUs via the cloud, we utilized pyQuil [71], an open-source Python library provided by Rigetti Computing. This library offers application programming interfaces (APIs) for specifying the quantum circuits to be executed on the QPUs and extracting data obtained during measurement operations. Additionally, pyQuil features a quantum virtual machine (QVM) emulator, which can simulate the circuits of interest and generate synthetic data that replicates the measurement outcomes observed in real experiments. Furthermore, the library provides APIs for incorporating noise into the synthetic data using various noise models discussed in Chapter 1.5.

To begin, we present calculations for the single-qubit system introduced in Chapter

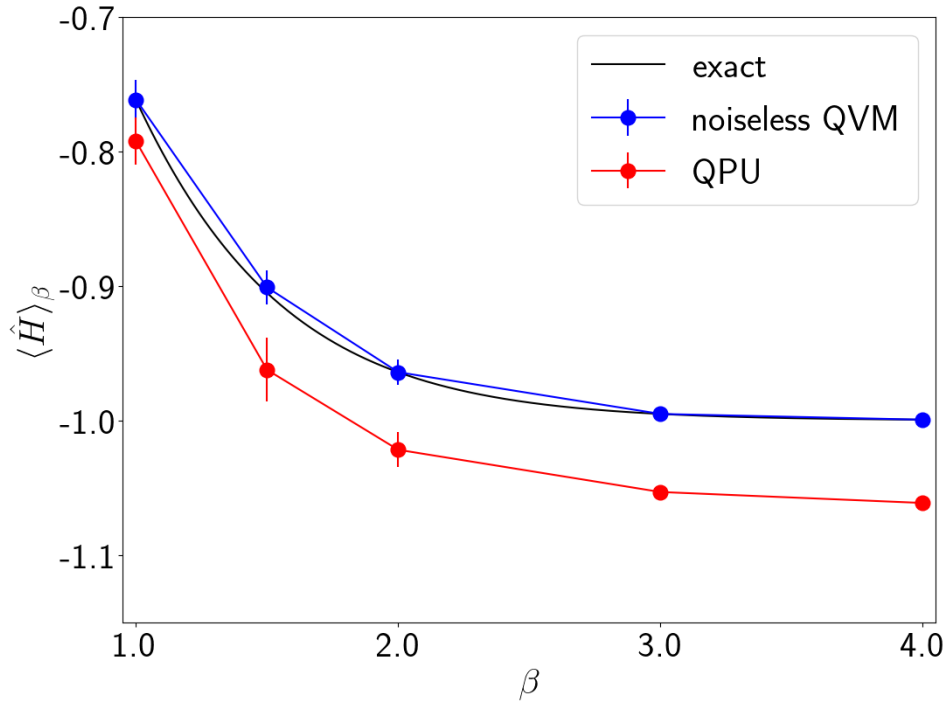

Figure 3.2: **QMETTS calculation on a quantum computer for a single-qubit system.** The mean and standard deviation of the thermal energy $\langle H \rangle_\beta$ as a function of imaginary time β. The data from the Quantum Virtual Machine (QVM) matches the exact solution. While there is a systematic shift in the data from the quantum processing unit (QPU), it reproduces the qualitative trend in the phase diagram. To perform the calculations, a total of 10 Trotter steps are taken at each data point. 1500 measurements are used to determine the expectation values of each observable. In addition, 70 samples were used at each data point.

2.4.2. The METTS algorithm was executed on both the Aspen-1 quantum processing unit and the QVM. We employed 70 samples and plotted the mean and standard deviation of the thermal energy $\langle H \rangle_\beta$ as a function of imaginary time β in Fig. 3.2. The QVM successfully reproduced the exact phase diagram, affirming the expected functionality of the algorithm. Conversely, the data from the QPU exhibited a systematic shift in the thermal energy, likely attributable to hardware imperfections. Nevertheless, it captured the qualitative features of the phase diagram, marking the first successful implementation of finite temperature simulations on NISQ devices.

Next, we also present emulated calculations for the two-qubit system introduced in Chapter 2.4.3. The METTS algorithm was executed on the QVM both with and without noise. We plotted the mean and standard deviation of the thermal energy $\langle H \rangle_\beta$ as a function of imaginary time β in Fig. 3.3. As before, the QVM successfully reproduced the exact phase diagram in the absence of noise. However,

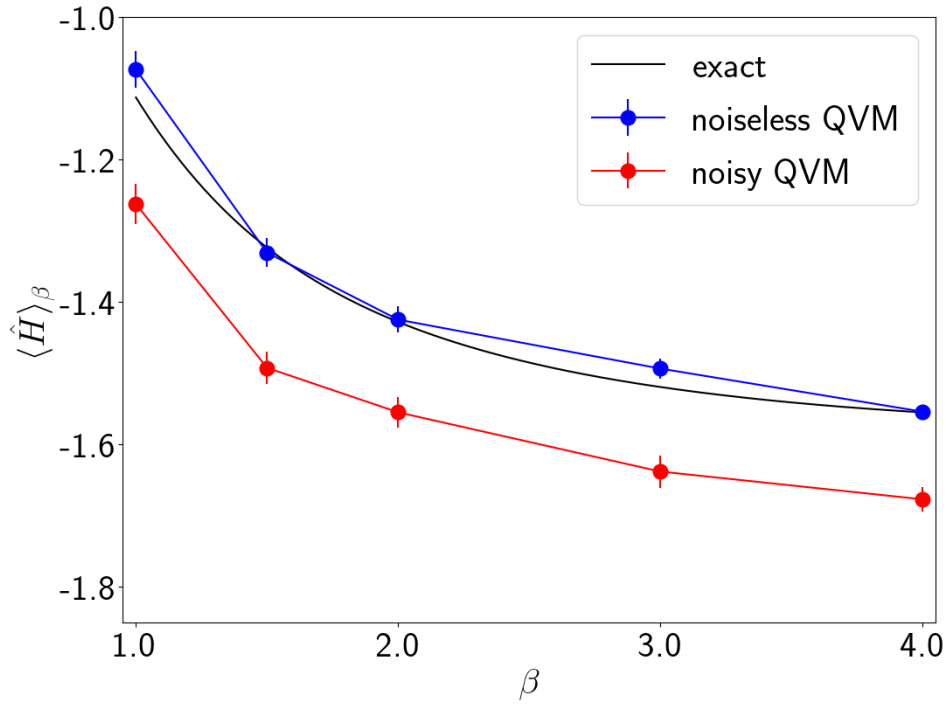

Figure 3.3: **Emulation of QMETTS using QVM for a two-qubit system.** The mean and standard deviation of the thermal energy $\langle H \rangle_\beta$ as a function of imaginary time β. The data from the Quantum Virtual Machine (QVM) matches the exact solution. The noisy QVM results reproduce the systematic shift observed in Fig. 3.2. To perform the calculations, a total of 10 Trotter steps are taken at each data point. 30000 measurements are used to determine the expectation values of each observable. In addition, 100 samples were used at each data point. We use the noise parameters defined in noise model 1 for the noisy emulation (see Chapter. 2.4.3).

when noise was introduced in the QVM emulation, we observed a systematic shift in the thermal energy, consistent with our earlier findings. These results further support the potential of QMETTS as a powerful tool for performing finite temperature simulations on a quantum computer.

3.2 Computing free energies using QITE

3.2.1 Background

The free energy F is related to the partition function Z through the equation $F = -\frac{1}{\beta}\ln Z$, where β is the inverse temperature and we consider the Boltzmann constant to be 1. Computation of either F or Z is a crucial task in finite temperature simulation as they offer valuable insights into the thermodynamic properties, such as heat capacities, of the physical system. Therefore, the quantum computation of these quantities is an important problem that warrants further investigation.

Early proposals focused on preparing Gibbs states [75, 76] to efficiently evaluate the partition function. However, as discussed in Chapter 3.1.1, such methods rely on quantum phase estimation, which is not reliably executable on NISQ devices.

Alternatively, variational methods have been suggested as an alternative approach to prepare thermal states on NISQ devices [80–82]. These methods [83] have been successfully demonstrated on hardware for evaluating the zeros of the partition function and, consequently, the free energy. However, as discussed in Chapter 2.2, variational methods suffer from the challenge of solving the optimization problem [65], and they often require a large number of measurements [60] to accurately evaluate observables.

Another approach is to use QITE and QMETTS as subroutines in a workflow to calculate free energy differences [84]. However, this method only provides an upper bound on the free energy difference and only converges to the exact difference in certain cases. Importantly, this method does not directly provide the free energy itself.

3.2.2 QITE evaluation of partition function

We propose a method to compute the free energy using the QITE algorithm. To achieve this, we observe that the partition function can be evaluated over any basis set $|i\rangle$ as follows

$$\begin{aligned} Z &= \mathrm{Tr}[e^{-\beta\hat{H}}] \\ &= \sum_i \langle i|e^{-\beta\hat{H}}|i\rangle \\ &= \sum_i \langle \phi(i)|\phi(i)\rangle \quad |\phi(i)\rangle = e^{-\beta/2\hat{H}}|i\rangle \end{aligned} \tag{3.4}$$

In the last line, we observe that the partition function can be expressed as a sum of norms $\langle\phi(i)|\phi(i)\rangle$. Specifically, if we consider the complete computational basis states $|i\rangle$, our task is accomplished if we can evaluate $\langle\phi(i)|\phi(i)\rangle$ using a quantum computer. Remarkably, the QITE algorithm involves the computation of norms, as shown in Eqn. 2.7, to establish the system of equations. Therefore, by applying the QITE algorithm to a basis state $|i\rangle$, we gain the necessary information to evaluate $\langle\phi(i)|\phi(i)\rangle$.

Figure 3.4: **Layout of IBM Q devcie Bogota.** It consists of 5 transmon qubits arranged in a linear chain. The figure is reproduced from [85].

3.2.3 Demonstration of free energy calculations using QITE

As a proof of concept, we conducted our algorithm on the IBM Q device Bogota, which consists of 5 transmon qubits. The device layout is depicted in Figure 3.4. To interface with Bogota and collect measurement data, we utilized Qiskit [72], an open-source development kit for quantum computing. This library offers application programming interfaces (APIs) to specify the quantum circuits to be executed on Bogota and extract the corresponding data. Qiskit also provides tools for numerical simulations of the implemented circuits, including a statevector simulator for exact computation of observable expectation values and an emulator for approximate measurement-based sampling. Additionally, the library incorporates noise channels, as described in Chapter 1.5, to incorporate realistic noise models into numerical simulations.

We demonstrated the potential of our algorithm by computing the free energy of a two-qubit transverse-field Ising model (TFIM) described by the Hamiltonian:

$$H = -JZ_0Z_1 + h(X_0 + X_1) \tag{3.5}$$

with $J = 3$ and $h = 1$. To construct the QITE operation at each Trotter step, typically 15 operators are required: $\{X_0, Y_0, Z_0, X_1, Y_1, Z_1, X_0X_1, X_0Y_1, X_0Z_1, Y_0X_1, Y_0Y_1, Y_0Z_1, Z_0X_1, Z_0Y_1, Z_0Z_1\}$. However, due to symmetry considerations [86], we discovered that the number of required operators can be reduced to just one: X_0Y_1. This operator alone suffices for implementing QITE in this system, and the proof of this construction is provided in Appendix A.

We begin by conducting numerical simulations using the emulator and statevector capabilities provided by Qiskit. For the emulator, we utilize 8192 measurements to estimate the expectation values.

In Fig. 3.5, we plot the free energy $F(\beta)$ as a function of imaginary beta β. From our statevector simulation, we observe that by using a step size of $d\tau = 0.01$, the free energy converges to the numerically exact free energy, confirming the validity of our protocol. When we increase the step size to $d\tau = 0.1$, a systematic shift in the free

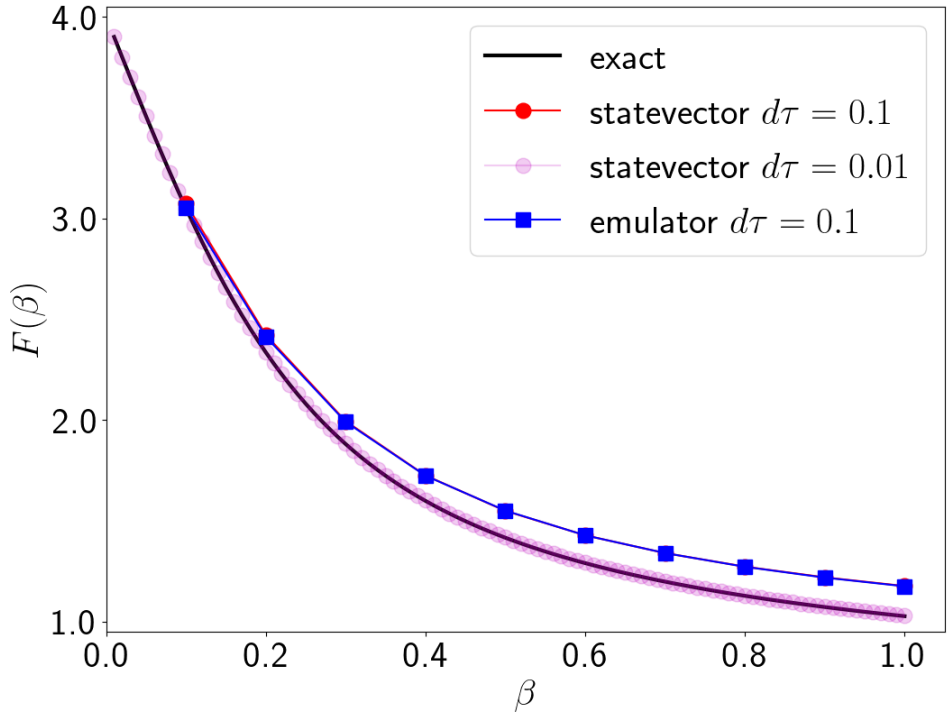

Figure 3.5: **Numerical computation of free energy for two-qubit systems using statevector and emulator.** The free energy $F(\beta)$ against imaginary beta β is plotted. The data from the statevector converges to the numerically exact curve using a Trotter step size $d\tau = 0.01$. The data generated using a $d\tau = 0.1$ is qualitatively similar. 8192 measurements are used per observable for the simulation carried out using the emulator.

energy occurs, likely attributable to Trotter error. Nonetheless, the obtained data exhibits qualitative similarities to that obtained with a smaller step size. Notably, we also observe that the data generated by the emulator converges towards the data generated by the statevector simulation, indicating that sampling errors are small. These findings suggest that employing a step size of $d\tau = 0.1$ along with 8192 measurements per observable is sufficient for validating our algorithm on the actual quantum device.

We execute the algorithm on IBM Q Bogota, employing 8192 measurements and a step size of 0.1. In addition, we generate data using an emulator with a noise model provided by IBM [87], which captures the device's noise characteristics.

Fig. 3.6 displays the plot of the free energy $F(\beta)$ as a function of imaginary beta β. Promisingly, we observe that despite a systematic shift, the data obtained from the hardware device exhibits qualitative similarity to the data generated by the noiseless emulator. This systematic shift is also evident in the data generated by the

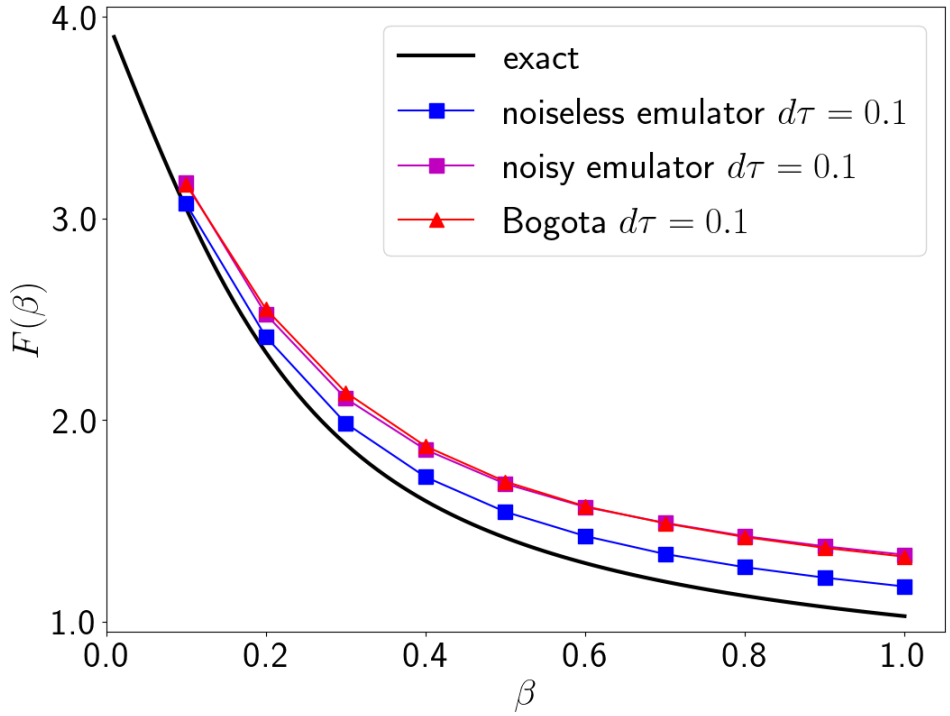

Figure 3.6: **Computation of free energies for 2-qubit system using IBM Q Device.** The free energy $F(\beta)$ against imaginary beta β is plotted. The data from the hardware is qualitatively similar to the emulator results without noise. The systematic shift in free energy can be reproduced by using a noise model provided by IBM Q [87] . 8192 measurements are used per observable for the simulation carried out using the emulator.

emulator with noise. These findings suggest that as quantum devices improve, we can anticipate obtaining more accurate quantitative results. Collectively, our results demonstrate the feasibility of our protocol for calculating free energies on NISQ devices.

3.2.4 Sampling partition function

Although the proposed algorithm has been validated successfully, it is worth noting that the sum in Eqn. 3.4 requires the evaluation of d^N terms, where d and N represent the number of dimensions of each site and the total number of sites, respectively. This implies that the proposed algorithm still incurs an exponential cost when implemented on a quantum computer.

To address this challenge, we propose a workaround by approximating the partition function using random sampling. This idea is inspired by previous work that numerically evaluated thermal observables on classical computers through a few random evaluations of "typical" states [88–90]. We hypothesize that a similar approach could be effective for evaluating the partition function, and thus modify our algorithm as follows

$$Z \approx \frac{N}{S} \sum_{\text{sample},i\in|i\rangle}^{S} \langle\phi(i)|\phi(i)\rangle \quad |\phi(i)\rangle = e^{-\beta/2\hat{H}}|i\rangle \tag{3.6}$$

In this modified algorithm, we randomly sample S computational basis states to evaluate the partition function. This approach provides an approximation of the true partition function while reducing the computational burden associated with evaluating all d^N terms.

We validate the proposed protocol by applying it to a 4-site analog of the system described in Eqn. 3.5. In this case, the partition function involves the evaluation of 16 terms. To assess the feasibility of our approach, we perform calculations using a sample size of $S = 10$ and repeat the routine 10 times, implementing the algorithm through classical numerical simulation.

In Fig. 3.7, we present the mean and standard deviation of the free energy $F(\beta)$ as a function of imaginary beta β. Our numerical results demonstrate that a sample size of 10 is sufficient to obtain a converged free energy. This finding is highly encouraging, suggesting that our protocol effectively captures the essential features of the system with a significantly reduced computational cost compared to evaluating all d^N terms.

We extend our investigation to examine the behavior of numerical error as the system size increases. In addition to the 4-site system, we perform similar calculations for systems with 6, 8, and 10 sites. In all cases, we use a sample size of $S = 10$ and repeat the routine 10 times to ensure statistical accuracy.

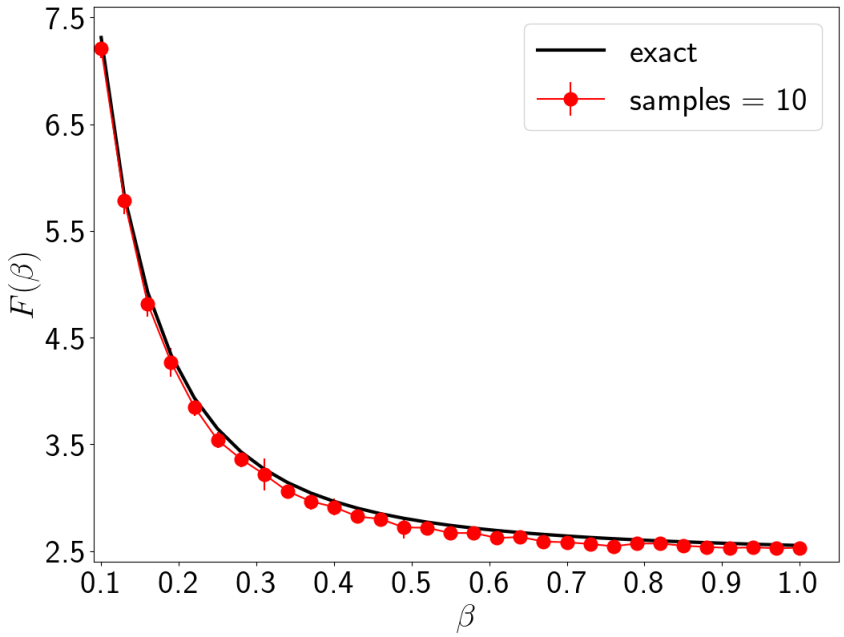

Figure 3.7: **Random sampling to evaluate free energies.** Mean and standard deviation of the free energy $F(\beta)$ against imaginary beta β obtained from repeating the algorithm 10 times. The free energy converges to the numerically exact answer with 10 samples.

In Fig. 3.8, we present the mean and standard deviation of the relative error in the free energy, denoted as Rel. error $F(\beta)$, as a function of the number of sites for different values of imaginary time β (0.1, 0.4, 0.7, 1.0). The relative error is defined as $|F(\beta) - F_{\text{exact}}|/F_{\text{exact}} \times 100$, where F_{exact} represents the exact value of the free energy. Notably, our numerical results exhibit no abnormal behavior in the relative error across the different values of β. The largest relative error we observe is $3.1 \pm 2.2\%$ when $\beta = 0.4$ and the number of sites is 4. This finding suggests that the free energy can be reliably evaluated with a smaller number of samples compared to the full computational cost of evaluating d^N terms. Combining these results with our earlier findings, we establish a feasible approach to evaluate the free energy of larger system sizes on a quantum computer.

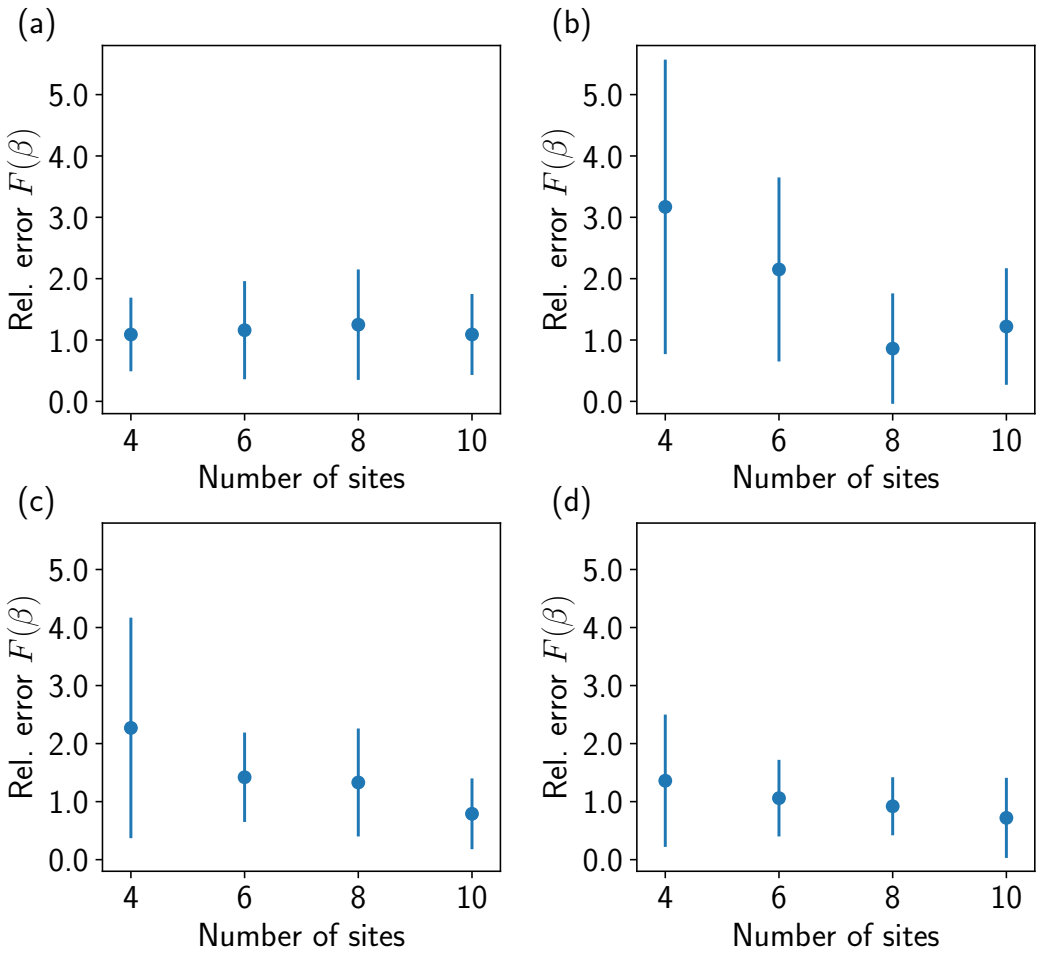

Figure 3.8: **Error in random sampling evaluation of free energy.** The relative error in free energy Rel. error $F(\beta)$ is plotted against the number of sites for β = (**a**) 0.1, (**b**) 0.4, (**c**) 0.7, and (**d**) 1.0. The relative error is defined as defined by $|F(\beta) - F_{exact}|/F_{exact} \times 100$. We see that the protocol is numerically well-behaved.

3.3 Conclusion

In conclusion, we have presented innovative approaches that utilize quantum imaginary time evolution for finite temperature simulations on quantum computers. We validated a practical method to sample minimally entangled thermal typical states on quantum computers, and have achieved the computation of thermal averages using a quantum computer for the first time.

Furthermore, we have addressed the crucial task of computing the free energy, which provides a comprehensive characterization of a system's thermodynamic properties at finite temperature. Our approach has been successfully validated on real hardware, yielding promising results. Moreover, we have proposed a scalable strategy using random sampling to enhance our original approach, and provided

numerical evidence supporting its effectiveness in evaluating the free energies of larger systems on NISQ devices.

Our work makes significant contributions to the ongoing exploration of quantum computers' potential in studying the finite temperature physics of condensed matter and chemical systems. Solving this problem holds tremendous technological implications, and our efforts contribute to advancing this field of research.

Chapter 4

ADIABATIC PREPARATION OF A SYMMETRY-PROTECTED TOPOLOGICAL (SPT) PHASE

This chapter is adapted from:

1. **Tan, Adrian T.K.**, Sun, S.-N., Tazhigulov, R. N., Chan, G. K.-L. & Minnich, A. J. Realizing symmetry-protected topological phases in a spin-1/2 chain with next-nearest neighbor hopping on superconducting qubits. *Phys. Rev. A* **107,** 032614. https://link.aps.org/doi/10.1103/PhysRevA.107.032614 (3 2023).

   Contributions A.T.K.T. conceptualized the project, designed and optimized the quantum circuits, carried out the simulation runs on the quantum computers, performed simulations and analyzed the experimental data, and wrote the manuscript.

The exploration of topological phases of matter has garnered significant interest in the scientific community. These phases defy the conventional Landau paradigm that relies on local order parameters resulting from symmetry breaking. Understanding their ground-state properties and excitations has become a thriving field of research in condensed matter physics [91–94].

In alignment with Feynman's vision of harnessing quantum systems to simulate quantum phenomena, there is a growing interest in preparing and studying these phases on quantum platforms. Furthermore, the creation of novel quantum states of matter provides an opportunity to assess the capabilities of near-term digital quantum computers in implementing relevant quantum simulation circuits.

Considering these objectives, we conduct benchmark studies to realize the symmetry-protected topological (SPT) phases of a spin-1/2 Hamiltonian with next-nearest-neighbor hopping on up to 11 qubits on a programmable superconducting quantum processor and present our work in this Chapter.

We first provide an overview of previous work that has successfully achieved topological phases of matter using quantum simulators. Next, we present a model based on a spin-1/2 Hamiltonian with next-nearest-neighbor hopping, which serves as a host for SPT phases. We highlight the experimental signatures that can be used to

identify these phases. Subsequently, we detail our approach, combining adiabatic state preparation with circuit recompilation, to achieve the desired SPT phases on a programmable superconducting quantum processor. Our experimental data exhibits clear indications of two distinct SPT phases, including excitations localized to specific edges and finite string order parameters. Additionally, we identify a parasitic phase associated with the two-qubit gate as the primary imperfection limiting circuit depth. We discuss our attempts to mitigate the impact of this parasitic phase.

4.1 Background and motivation

Early studies of topological phases on quantum platforms primarily utilized analog quantum simulators. These experiments explored a wide range of fascinating topological phases and associated phenomena, including models with topological band structures [95–98], Thouless charge pumps [99–101], various symmetry-protected topological (SPT) phases [102–107], and quantum spin liquids [108]. However, analog quantum simulators have limitations due to their specific native interactions, restricting the study of only a subset of topological phases [109]. In contrast, gate-based quantum simulation, which can efficiently synthesize a broader range of interactions using appropriate quantum logic gates [17], has emerged as a more flexible approach for investigating these exotic phases.

Significant progress has already been made in the study of various topological phases using circuit-based quantum computation. For instance, SPT phases in a spin-1/2 chain model with three-body interactions have been successfully realized on superconducting quantum processors [110–112]. Additionally, quantum circuits for preparing ground states of the toric code [113] and topological Floquet phases [114] have been developed and utilized to explore the topological properties of these systems. These studies underscore the potential of circuit-based quantum computation as a valuable tool for realizing and investigating intriguing topological phases of matter.

Furthermore, beyond achieving the desired quantum phase, comparing the experimental data with theoretical predictions allows for benchmarking quantum devices and identifying hardware imperfections that restrict circuit complexity [115, 116]. The impact of these imperfections varies depending on the circuit's specific structure, indicating that benchmarking methods utilizing dissimilar circuit structures are inadequate for characterizing devices intended for quantum simulation applications [117]. Randomized circuits, commonly employed in protocols assessing quantum

computer performance [118, 119], do not accurately reflect the influence of coherent errors in more structured circuits [120, 121]. To obtain more relevant information about the capabilities of near-term hardware, circuits performing representative quantum simulation tasks are expected to be more suitable for benchmarking purposes.

In particular, we believe spin-1/2 models with beyond-nearest-neighbor interactions are especially an attractive target of study that align with our objectives. hese models require more complex circuits to be realized compared to those with only nearest-neighbor couplings, making them suitable benchmarks for state-of-the-art superconducting quantum processors. Additionally, these models exhibit rich physics [122, 123], warranting further investigation. Of particular interest are topological phases characterized by non-local string order parameters and edge excitations [124], which we will describe in the following section.

4.2 SPT phases of spin-1/2 chain with next-nearest neighbor hopping

We consider a one-dimensional spin-1/2 chain with NN and next-nearest-neighbor (NNN) interactions. The Hamiltonian is given by

$$\begin{aligned} H_T = -\sum_k & J_1'(\sigma_{2k}^x\sigma_{2k+1}^x + \sigma_{2k}^y\sigma_{2k+1}^y + \eta\sigma_{2k}^z\sigma_{2k+1}^z) \\ & + J_1(\sigma_{2k+1}^x\sigma_{2k+2}^x + \sigma_{2k+1}^y\sigma_{2k+2}^y + \eta\sigma_{2k+1}^z\sigma_{2k+2}^z) \\ & + J_2(\sigma_k^x\sigma_{k+2}^x + \sigma_k^y\sigma_{k+2}^y + \eta\sigma_k^z\sigma_{k+2}^z) \end{aligned} \tag{4.1}$$

where $\sigma^x, \sigma^y, \sigma^z$ are Pauli operators, J_1' (J_1) denotes the strength of the NN interactions from the even to odd sites (odd to even), J_2 denotes the strength of the NNN coupling and η is the anistropy of the interactions. A schematic of the spin$-\{1/2\}$ chain is given in Fig. 4.1.

Zou et. al. [124] numerically determined the phase diagram of H_T (see Fig. 4.2) and show that it contains two distinct gapped SPT phases known as the even-parity dimer (ED) and singlet-dimer (SD) phases. In addition, they show that for the case where $\eta = 0$, the model is in the ED (SD) phase when $J_1' = 2J_1 < 0; J_1 > 0$ ($J_1 = -2J_2 > 0; J_1' < 0$) and analytically derived the behavior of the edge states in the two phases. Each edge state is two-fold degenerate and protected by time-reversal (TR) symmetry. The two phases are topologically distinct because they cannot be deformed into one another without breaking TR, inversion, and D_2 symmetry of spin rotation by π about the x, y, and z axes [125].

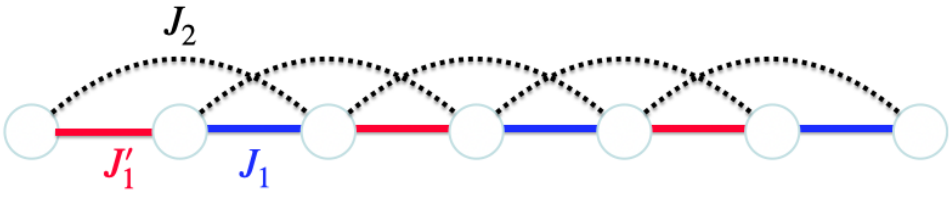

Figure 4.1: **Arrangement of sites in a spin$-1/2$ chain of 7 sites.** The strength of interactions going from even-labelled to odd-labelled (odd-labelled to even-labelled) sites are given by J_1' (J_1); those for NNN couplings are given by J_2. For this study, we also consider chains with 9 and 11 sites.

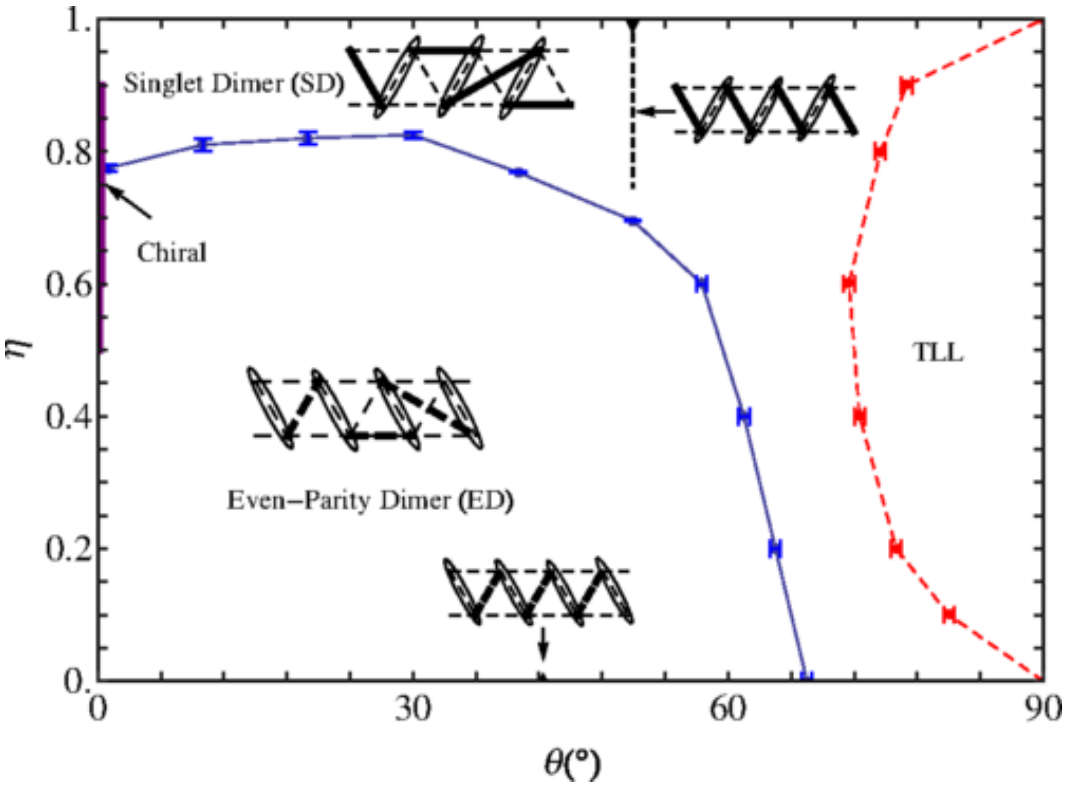

Figure 4.2: **The phase diagram of H_T in the $\theta - \eta$ plane obtained using iTEBD.** For the numerical calculations, the couplings in Eqn. 4.1 are parametrized using $J_1 = [1 - 3\cos^2(\theta + \gamma)]$, $J_1' = [1 - 3\cos^2(\theta - \gamma)]$, and $J_2 = [1 - 3\sin^2\theta]/8\sin^3\gamma$ where $\gamma = 30^o$. The insets depict the singlet dimer (SD) and even-parity dimer (ED) phases. In addition to the two SPT phases, the phase diagram contains a Chiral phase and a Tomonaga-Luttinger liquid (TLL) phase. The figure is reproduced from [124].

These phases can be distinguished by the location of their edge excitations; for a lattice with an odd number of lattice points, the ED (SD) phase has an edge excitation on the right (left) edge of the chain. In addition, the phases can be distinguished by string order parameters, defined as:

$$O_{z_n} = -\lim_{r\to\infty}\langle(\sigma^z_n + \sigma^z_{n+1})e^{i\pi\sum_k \sigma^z_k}(\sigma^z_{2r+n} + \sigma^z_{2r+n+1})\rangle \tag{4.2}$$

where the sum over k is restricted to $n+2 \leq k \leq 2r+n-1$ and r should be as large as possible. Generally, a non-zero string-order parameter indicates the presence of hidden long-range order and a topologically non-trivial phase. In the present model, the ED (SD) phase exhibits a finite O_{z_n} value for odd (even) n. In this work, n is chosen to be 0 or 1. To select r, we choose the largest value that satisfies the constraint that the number of operators used to construct O_{z_0} and O_{z_1} are the same. This requirement is equivalent to using the maximum integer value of r that satisfies $2r + 1 + 1 \leq M$, where M is the number of sites of the system. For systems with $M = 7, 9, 11$, this constraint corresponds to $r = 2, 3, 4$, respectively.

4.3 Preparation of SPT phases on Rainbow and Weber quantum processors

4.3.1 Quantum hardware and software

For this work, we used Google's Rainbow and Weber quantum processors. The Weber and Rainbow processors consist of a two-dimensional array of 49 and 54 transmon qubits, respectively, with each qubit tunably coupled to its neighbors. The layouts for the two processors are given in Fig. 4.3. The native single-qubit gates are the PhasedXZ gate which consists of a rotation about an axis in the XY plane of the Bloch sphere with an extra phase about the Z axis. The native two-qubit gates are the $\sqrt{\text{iS}}^{\dagger}$ gates. Further information on the device parameters are available in Ref. [126]. Simulated data in the absence of noise are generated using Google's circuit emulator qsim. [127]

4.3.2 Adiabatic state preparation of SPT phases

We employed adiabatic state preparation (ASP) [8, 128] to prepare the symmetry-protected topological (SPT) phases of the Hamiltonian H_T on a superconducting quantum processor. Specifically, we considered the case where $\eta = 0$. The system was initialized in the ground state of an initial Hamiltonian H_I and evolved to the ground state of the target Hamiltonian H_T over a duration of time T using a linear interpolation $H(s) = (1-s)H_I + sH_T$, where $s \equiv t/T$. In this study, H_T is given by Equation (1). The initial Hamiltonian H_I is defined as follows:

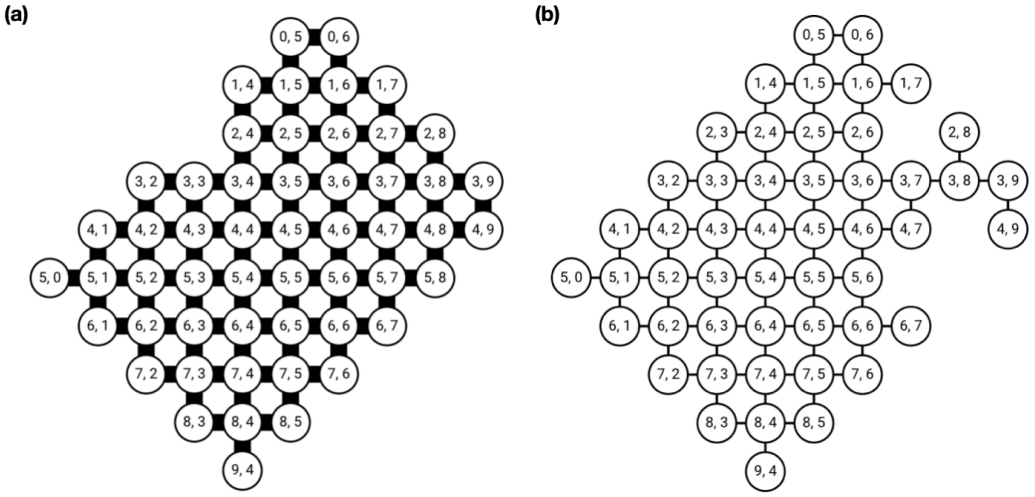

Figure 4.3: **Layout of Google's quantum processors.** (a) Weber quantum processor with 53 qubits. (b) Rainbow quantum processor with 49 qubits. The layout for the two is similar with the main difference being Weber having 4 more qubits.

$$H_I = -B_z \sum_k (-1)^k \sigma_k^z \tag{4.3}$$

with B_z a uniform external field. For $B_z > 0$ and an odd number of sites, the ground state of H_I is given by $|\downarrow\uparrow\downarrow\uparrow \ldots \downarrow\uparrow\downarrow\uparrow\downarrow\rangle$ which can be prepared by applying X-rotation single-qubit gates on sites labeled by odd indices.

We performed the following transformation to map the model onto the quantum processor:

$$\begin{aligned} |\downarrow\rangle &\rightarrow |0\rangle \\ |\uparrow\rangle &\rightarrow |1\rangle \\ \sigma_k^z &\rightarrow Z_k \end{aligned} \tag{4.4}$$

To carry out ASP, we utilized first-order Trotterization (see Chapter 1.3) to approximate the adiabatic evolution. The resulting steps were implemented using quantum circuits constructed from single-qubit and two-qubit gates. Fig. 4.4 illustrates the Trotterized circuit used for this purpose. The two-qubit gate K, known as the fermionic simulation (FSIM) gate, was constructed using the available native gate set [115].

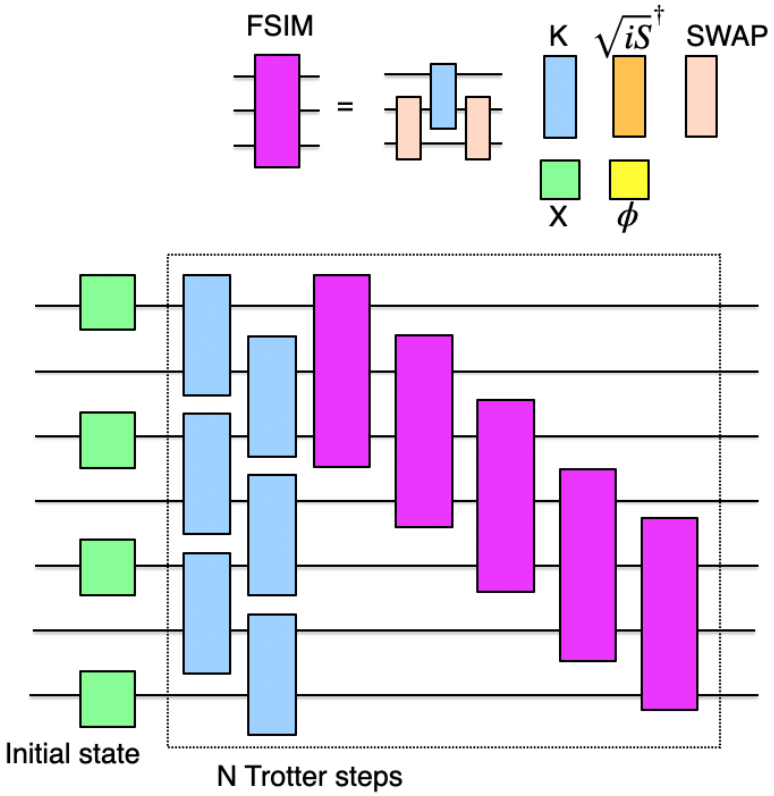

Figure 4.4: **Circuit to implement Trotterized ASP for a system with 7 sites for N Trotter steps.** The matrix representations for the quantum gates used to construct the circuits are provided in ref. [129].

4.3.3 Circuit recompilation scheme

Despite extensive experimentation, the overall circuit that carries out the full ASP was found to produce qualitative inaccuracies with theory. To assess the maximum gate depth that could be achieved while yielding quantitative agreement, we used a circuit recompilation scheme [86] by fitting the circuits needed to realize the state at each time in the adiabatic evolution to a parameterized circuit. In ref. [86], the parameterized circuits consisted of alternating layers of single-qubit gates and two-qubit gates. We used this ansatz in our benchmark studies by using the native gate $\sqrt{\text{iS}}^\dagger$ for the two-qubit gate and the native gate PhasedXZ(ϕ) for the single qubit gate, respectively. A schematic of the final recompiled circuit is shown in Fig. 4.5.

The circuit recompilation scheme works as follows. Let the target unitary be U_{targ} and the parameterized circuit be $U_{rec}(\boldsymbol{\theta})$, where $\boldsymbol{\theta}$ is a composite vector of all the free variables in the parameterized circuit. Given a reduced density operator ρ on the finite domain acted on by the target unitary, the optimal parameterized circuit is

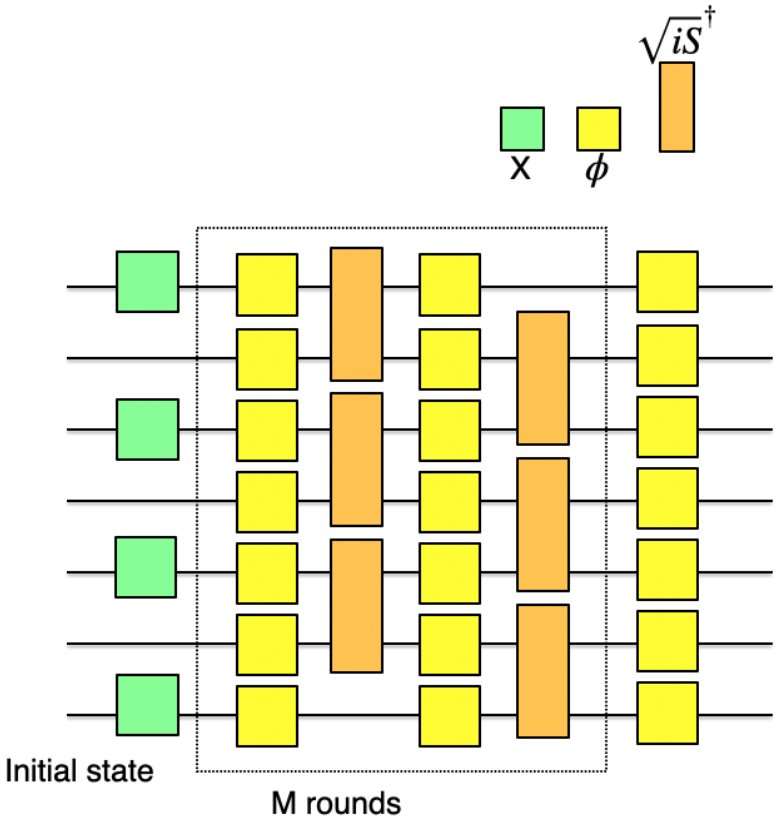

Figure 4.5: **Schematic of the recompiled circuit with M gate rounds.** The matrix representations for the quantum gates used to construct the circuits are provided in ref. [129].

found by performing a gradient descent to maximize the function

$$F(\boldsymbol{\theta}) = \left|\mathrm{Tr}(U_{\mathrm{rec}}(\boldsymbol{\theta})^{\dagger} U_{\mathrm{targ}} \rho)\right|^2, \tag{4.5}$$

which can be interpreted as the fidelity between $U_{\mathrm{rec}}(\boldsymbol{\theta})$ and U_{targ} with respect to the reduced density matrix ρ. For the purpose of this work, we set $F(\boldsymbol{\theta}) = 0.999$ as the stopping criterion. We compare the number of two-qubit gates present in the target unitary U_{targ} at the end of 12 Trotter steps and in the parameterized circuit $U_{rec}(\boldsymbol{\theta})$ in Table 4.1. The number of two-qubit gates required decreases by around an order of magnitude with recompilation.

System size	U_{targ}	$U_{rec}(\boldsymbol{\theta})$
7	336	30
9	468	40
11	564	50

Table 4.1: Comparison of number of two-qubit gates in target unitary U_{targ} for 12 Trotter steps and in $U_{rec}(\boldsymbol{\theta})$ for different system sizes

4.4 Experimental results

We implemented the circuits as described and performed 8192 repetitions of each circuit with measurements in the Z-basis for all sites at each Trotter step. We collected data from 15 configurations of qubits; based on the $\sqrt{\text{iSWAP}}$ gate cross-entropy benchmarking (XEB) average error per cycle, we selected the ten best configurations, from which we computed the mean and standard deviation for all observables.

4.4.1 Preparation of ED phase for increasing system sizes

We first report calculations of the string order parameters O_{z_1} for the ED phase versus ASP time s for spin chains with 7, 9, and 11 sites. As per Eqn. 4.2, O_{z_1} can be written as:

$$\begin{aligned} O_{z_1,7\,sites} &= ZIZZZII + IZZZZII \\ &\quad + ZIZZIZI + IZZZIZI \end{aligned} \tag{4.6}$$

$$\begin{aligned} O_{z_1,9\,sites} &= ZIZZZZZII + IZZZZZZII \\ &\quad + ZIZZZZIZI + IZZZZZIZI \end{aligned} \tag{4.7}$$

$$\begin{aligned} O_{z_1,11\,sites} &= ZIZZZZZZZII + IZZZZZZZZII \\ &\quad + ZIZZZZZZIZI + IZZZZZZZIZI \end{aligned} \tag{4.8}$$

The string order parameters consists of sums of Z-strings such as $ZIZZZII$ and can be directly computed from the collected measurements in the z-basis.

To prepare the ED phase, the Hamiltonian parameters were set to $J_1 = 0.2$, $J_1' = -1.5$, $J_2 = -0.1$, $B_z = 2.5$, and $T = 3.0$, and $M = 5$ layers of gate rounds were used for circuit recompilation. Emulated results were obtained by running the Trotterized ASP circuit on Google's circuit emulator qsim.

We plot $|O_{z_1}|$ versus ASP time s on 7 sites in Fig. 4.6. We observe good agreement between the final value of $|\langle O_{z_1}\rangle|$ at $s = 1$ obtained from Trotterized ASP using

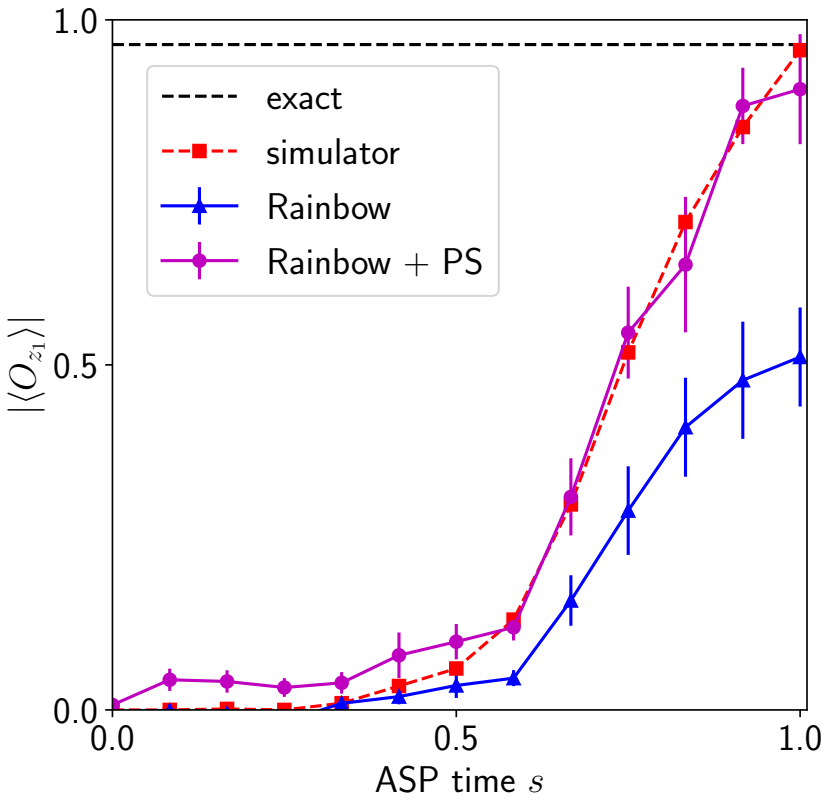

Figure 4.6: **Preparation of ED phase on Rainbow quantum processor.** Absolute value of the string order parameter O_{z_1} versus ASP time s for a system size of 7 qubits respectively. Data from Rainbow was collected using 15 different configurations of qubits and only the best 10 configurations were selected based on their $\sqrt{\text{iSWAP}}$ gate XEB average error per cycle. The hardware data without any error mitigation (blue triangle) yields qualitative agreement with the emulated ASP trajectory (red square). Quantitative agreement is obtained when post-selection is used (purple circle). The parameters $J_1 = 0.2$, $J_1' = -1.5$, $J_2 = -0.1$, $B_z = 2.5$, and $T = 3.0$ are used to prepare the ED phase. The lines through the symbols are guides to the eye.

qsim and the value from exact diagonalization in Fig. 4.6. This result indicates that a Trotter step size of 0.25 is sufficiently small enough to approximate the ASP evolution that yields the ED phase with high fidelity.

We next compare the data obtained by running Trotterized ASP trajectories on qsim with the data obtained by running recompiled circuits on Rainbow without any error mitigation for 7 sites. These circuits required 30 $\sqrt{\text{iS}}^{\dagger}$ gates. Although the trend of O_{z_1} increasing with ASP time is reproduced as seen in Fig. 4.6, a clear discrepancy exists for the final value of O_{z_1} at the end of the adiabatic trajectory. To mitigate this discrepancy, we perform post-selection based on S_{total} symmetry as described in Chapter 1.6.2. We observe a marked improvement in the quality of

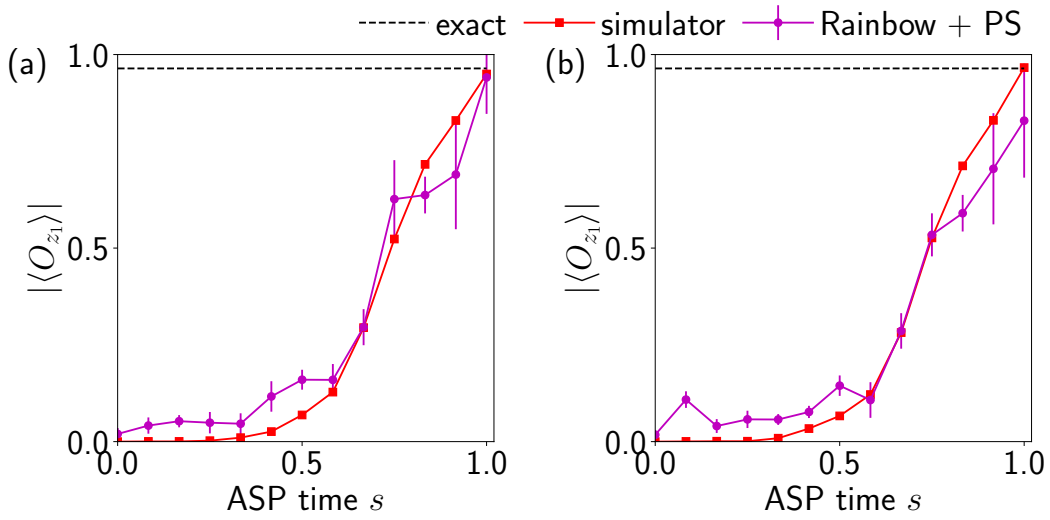

Figure 4.7: **Preparation of ED phase for increasing system sizes on Rainbow quantum processor.** Absolute value of the string order parameter O_{z_1} versus ASP time s for a system size of (**a**) 9, and (**b**) 11 respectively. Data from Rainbow was collected using 15 different configurations of qubits and only the best 10 configurations were selected based on their $\sqrt{\text{iSWAP}}$ gate XEB average error per cycle. The ED phase can be prepared reliably for system sizes of up to 11 qubits. The parameters $J_1 = 0.2$, $J_1' = -1.5$, $J_2 = -0.1$, $B_z = 2.5$, and $T = 3.0$ are used to prepare the ED phase. The lines through the symbols are guides to the eye.

the hardware data, with quantitative agreement obtained between the hardware data and the simulator. With this error mitigation step, the quantum processor is able to reproduce the adiabatic trajectory with sufficient fidelity to arrive at the expected non-zero value of the string order parameter in the ED phase.

We next compute O_{z_1} for system sizes of 9 and 11 qubits. The number of two-qubit gates used in the recompiled circuits was 40 and 50, respectively, compared to 30 in the 7 qubit case. Despite the larger number of gates, we observe good agreement in the value of the string order parameter over the adiabatic trajectory in Fig. 4.7a and 4.7b, although with a slight degradation that likely arises from the deeper circuits. The data indicates that the SPT phases for a system of 11 sites can be prepared with enough fidelity to observe its topological features on the Rainbow quantum processor.

4.4.2 Preparation of ED and SD phase on 11 qubits

Next, we verify that we can distinguish the SD and ED phases using the string order parameters. In addition to computing O_{z_1}, we compute O_{z_0} given by

$$O_{z_0,11\ sites} = IZIZZZZZZZI + IIZZZZZZZZI + IZIZZZZZZIZ + IIZZZZZZZIZ \tag{4.9}$$

Figure 4.8a and 4.8b shows $|O_{z_0}|$ and $|O_{z_1}|$ versus s on 11 qubits when the model is tuned into the ED phase. We observe good agreement between the hardware data and the simulator over the adiabatic path. At the end of the adiabatic path, we measure 0.029 ± 0.007 and 0.829 ± 0.147 for O_{z_0} and O_{z_1}, respectively, which is in good agreement with the expected values of ~ 0 and 0.964. Similarly, we tune the model into the SD phase by setting the Hamiltonian parameters to $J_1 = 1.5$, $J_1' = -0.2$, $J_2 = -0.1$. The string order parameters O_{z_0} and O_{z_1} versus s are given in Figs. 4.8c and 4.8d, respectively. Again, the final values of the string order parameter from the hardware are 0.981 ± 0.085 and 0.034 ± 0.013, which are in quantitative agreement with the numerically determined exact values of 0.962 and ~ 0. In both cases, we measured a finite value for the appropriate string order parameters and nearly zero for the other, indicating that the correct SPT phases were successfully prepared.

We finally present data on the occupancy of each site. The occupancy of the ith site is simply related to the expectation value $\langle Z_i \rangle$ and can also be directly computed by performing the appropriate sums with the measurement bitstrings. We plot the occupancy of each site at the end of the adiabatic evolution for the ED and SD phases in Figs. 4.9a and 4.9b, respectively. In the ED (SD) phase, an edge excitation is predicted to exist on the right (left) end of the chain. This feature is indeed observed using the exact solution obtained from exact diagonalization. The results from the hardware clearly indicate a difference in the occupancy on the appropriate edge of the chain for each phase and the rest of the chain, with the value in good agreement with the exact result. This observation provides additional evidence that the SPT states prepared on the hardware exhibit the key features expected of these topological phases.

4.4.3 Origin of gate depth limitations

The results obtained above required the use of circuit recompilation techniques to reduce the gate depth for ASP to a maximum of around 50 two-qubit gates. Without circuit recompilation, the number of required two-qubit gates was around 170 for 7

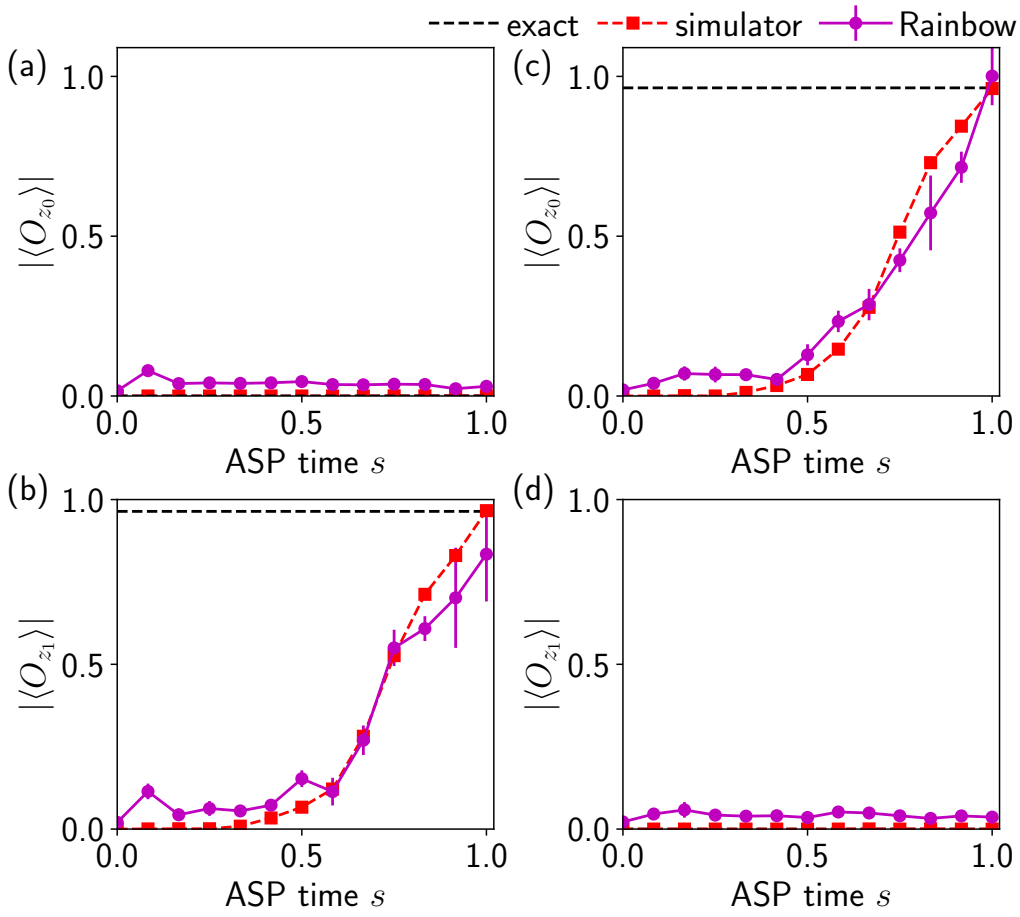

Figure 4.8: **String order parameter signatures of ED and SD phases for 11 qubits on the Rainbow quantum processor.** Absolute value of the string order parameters (**a**) O_{z_0} and (**b**) O_{z_1} versus ASP time (s) in the ED phase. (**c, d**) Analogous result for the SD phase. The two SPT phases can be prepared and distinguished clearly by finite or zero string-order parameter. The parameters $J_1 = 0.2$, $J_1' = -1.5$, $J_2 = -0.1$, $B_z = 2.5$, $T = 3.0$ were used to prepare the ED phase. The parameters $J_1 = 1.5$, $J_1' = -0.2$, $J_2 = -0.1$, $B_z = 2.5$, $T = 3.0$ were used to prepare the SD phase.

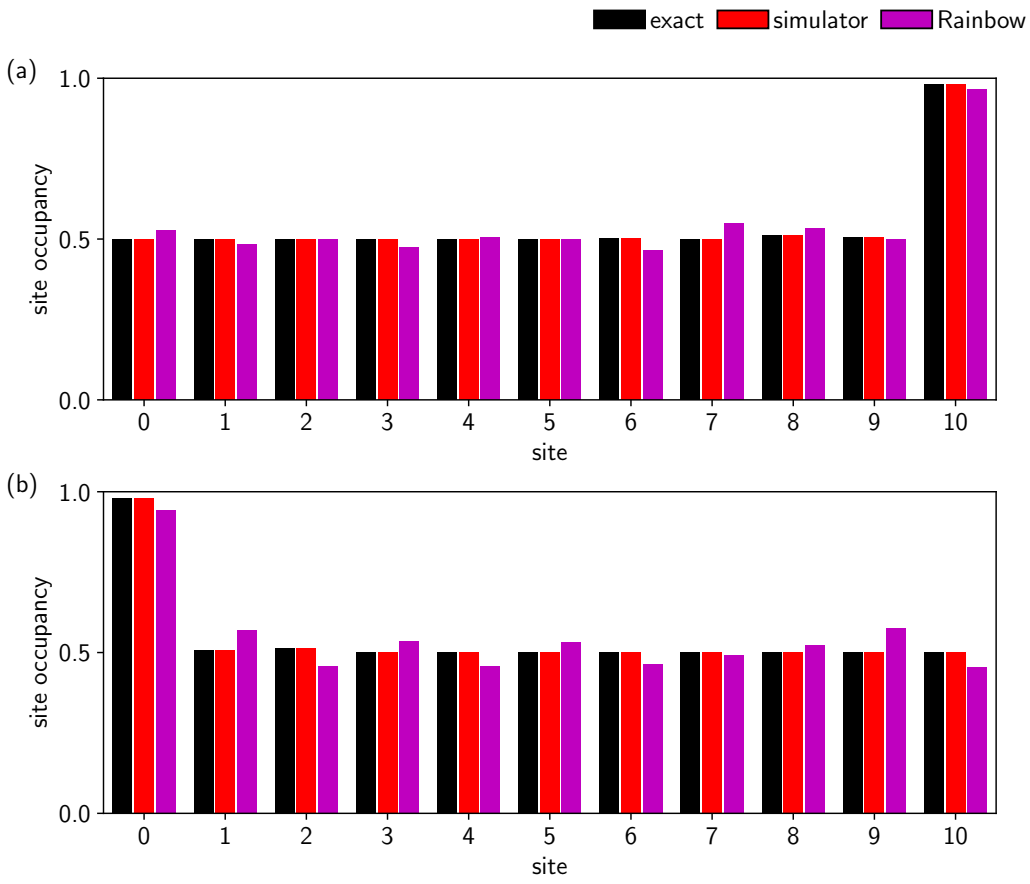

Figure 4.9: **Preparation of ED and SD phases using 11 qubits on the Rainbow quantum processor.** Occupancy of each site at the end of the ASP trajectory for the (**a**) ED and (**b**) SD phases. The two SPT phases can be prepared and distinguished clearly by the location of edge excitation. The parameters $J_1 = 0.2$, $J_1' = -1.5$, $J_2 = -0.1$, $B_z = 2.5$, $T = 3.0$ were used to prepare the ED phase. The parameters $J_1 = 1.5$, $J_1' = -0.2$, $J_2 = -0.1$, $B_z = 2.5$, $T = 3.0$ were used to prepare the SD phase.

sites, and the hardware results were in only qualitative agreement with the expected final string order parameter value. To investigate the origin of this circuit depth limitation, we examined the non-idealities of the two-qubit gates on the Rainbow processor. The most general excitation-number-conserving two-qubit gate, denoted by $U(\theta, \zeta, \chi, \gamma, \phi)$ takes the following form (with the basis states in the order $|00\rangle$, $|01\rangle$, $|10\rangle$, and $|11\rangle$)[115]:

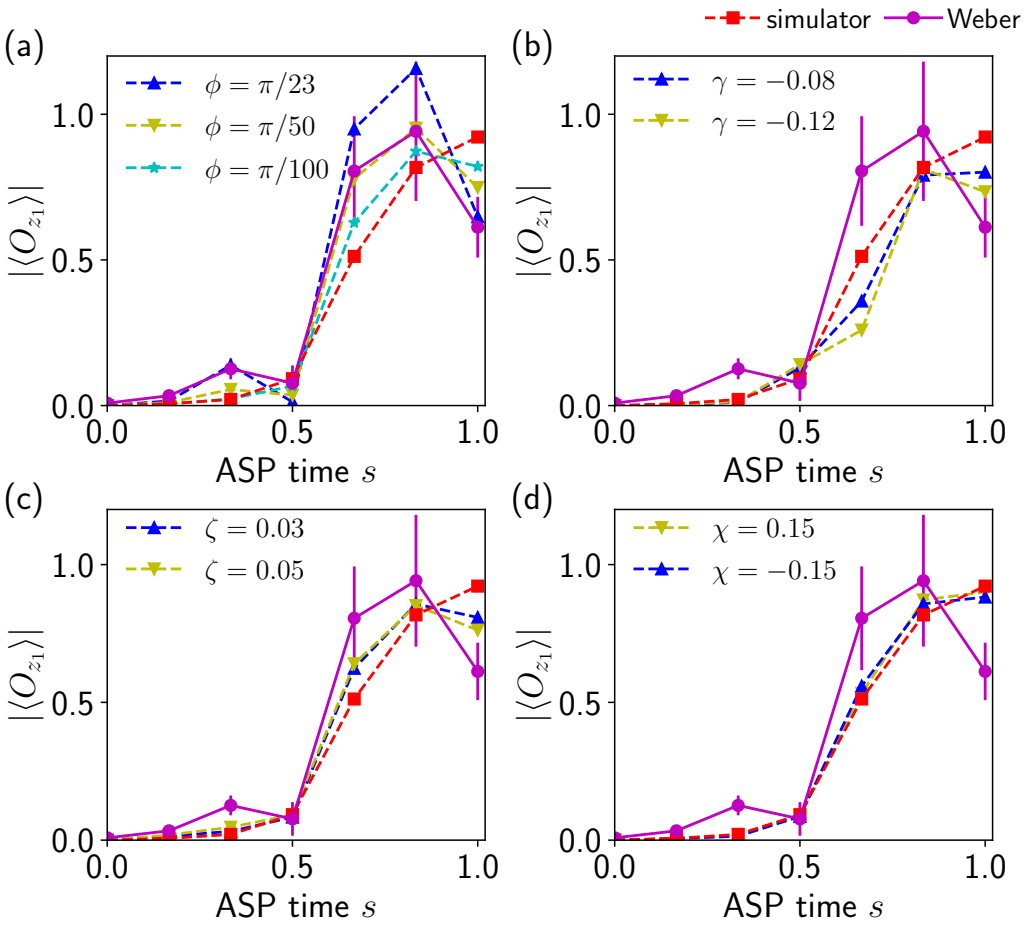

Figure 4.10: **Effects of gate imperfections on $|\langle O_{z_1}\rangle|$ in the ED phase.** Absolute value of the string order parameters O_{z_1} versus ASP time (s) in the ED phase when (**a**) ϕ, (**b**) γ, (**c**) ζ, and (**d**) χ are varied. Error bars for the hardware data (Weber) were obtained from 4 different qubit configurations. The parameter ϕ best explains the observed trend in string order parameter with s. The parameters $J_1 = 0.2$, $J_1' = -1$, $J_2 = -0.1$, $B_z = 1.5$, $T = 3.0$ were used to prepare the ED phase.

$$\begin{pmatrix} 1 & 0 & 0 & 0 \\ 0 & e^{-i(\gamma+\zeta)}\cos\theta & -ie^{-i(\gamma-\chi)}\sin\theta & 0 \\ 0 & ie^{-i(\gamma+\chi)}\sin\theta & e^{-i(\gamma-\zeta)}\cos\theta & 0 \\ 0 & 0 & 0 & e^{-i(2\gamma+\phi)} \end{pmatrix} \tag{4.10}$$

While the ideal native two-qubit gate on Rainbow and Weber is given by $U(\pi/4\ ,0\ ,0\ ,0\ ,0)^{\dagger}$, additional interactions lead to non-zero values of ζ, χ, γ and ϕ. We numerically simulated the effects of these non-idealities on the value of the string

order parameter along the adiabatic trajectory by plotting $|\langle O_{z_1}\rangle|$ versus ASP time s on 7 sites for different values of ϕ, γ, ζ, and χ.

Figure 4.10 shows the string order parameter versus ASP time s for various values of ϕ, γ, ζ, and χ. We also collected data from four different qubits configurations on Weber, a quantum processor with similar specifications as Rainbow, and plot the mean and standard deviation of the string order parameter. For comparison, we plot the ideal trajectory obtained using qsim [127]. Comparing the ideal trajectory with data from Weber, we observe a non-monotonic trend at the end of the trajectory in the hardware data. Similar behavior was observed in the simulator results for various values of ϕ, γ, ζ, and χ. The non-monotonic trend is observed to be most sensitive to ϕ, and the results with $\phi = \pi/50$ yielded the best qualitative agreement with the hardware results. These observations suggest that the parasitic controlled phase ϕ is a dominant factor in limiting the gate depth of the present simulations.

4.5 Attempts to mitigate parasitic phase

This section describes attempted strategies to mitigate the parasitic controlled phase. The first approach constructs CPHASE(ψ) and appends it to the back of the native gate with $\psi = -\phi$ to compensate for the parasitic phase; that is we implement $\sqrt{iS}^{\dagger}_{hardware}$CPHASE($\psi = -\phi$). This gate can be constructed exactly by using a series of single-qubit rotations and two $\sqrt{iS}^{\dagger}_{hardware}$ to compensate for the phase in each $\sqrt{iS}^{\dagger}$. By noting that $\sqrt{iS}^{\dagger}_{hardware}$ is approximately $\sqrt{iS}^{\dagger}$CPHASE(ϕ) for some parasitic phase ϕ, a controlled-phase gate between control qubit i and target qubit j, CPHASE($\psi = -\phi$)$_{ij}$ can be constructed exactly as [130]

$$\begin{aligned}
\text{CPHASE}(\psi)_{ij} =& [R_{Z_i}(\pi - \psi/2) \otimes R_{Z_j}(-\psi/2)], \\
& [R_{X_i}(-\xi_i) \otimes R_{X_j}(-\xi_j)], \\
& \sqrt{iS}^{\dagger}_{hardware,ij}, \\
& [R_{Z_i}(\pi + \phi/2) \otimes R_{Z_j}(\phi/2)], \\
& [R_{X_i}(-2\alpha) \otimes \mathcal{I}_j], \\
& \sqrt{iS}^{\dagger}_{hardware,ij}, \\
& [R_{Z_i}(\psi/2) \otimes R_{Z_j}(\psi/2)], \\
& [R_{X_i}(\xi_i) \otimes R_{X_j}(\xi_j)]
\end{aligned} \tag{4.11}$$

where R_Z, R_X are the single-qubit rotations around the z-axis and x-axis, and the decomposition parameters α, ξ_i, ξ_j are given by

$$\sin(\alpha) = \sqrt{\frac{\sin^2(\psi/4) - \sin^2(\phi/2)}{\sin^2(\pi/4) - \sin^2(\phi/2)}} \tag{4.12}$$

$$\xi_i = \tan^{-1}\left(\frac{\tan(\alpha)\cos(\pi/4)}{\cos(\phi/2)}\right) + \frac{\pi}{2}(1 - \mathrm{sgn}(\cos(\phi/2))) \tag{4.13}$$

$$\xi_j = \tan^{-1}\left(\frac{\tan(\alpha)\sin(\pi/4)}{\sin(\phi/2)}\right) + \frac{\pi}{2}(1 - \mathrm{sgn}(\sin(\phi/2))) \tag{4.14}$$

The cost of this approach is the addition of two native two-qubit gates for each original two-qubit gate, thereby increasing the gate depth by a factor of 3.

We tested this scheme on Weber by performing Floquet characterization to estimate the parasitic phase ϕ present on each qubit [115], then used the average value to construct a compensated CPHASE($-\phi_{avg}$) that was appended to the hardware gate $\sqrt{iS}^{\dagger}_{hardware}$. The results with these compensated circuits are presented in Fig. 4.11. We observe greater deviations from the exact result when the compensated circuits are used. The likely origin of the worse performance is the larger number of two-qubit gates are used in the compensated circuits (510 versus 170 to reach the end of the adiabatic path).

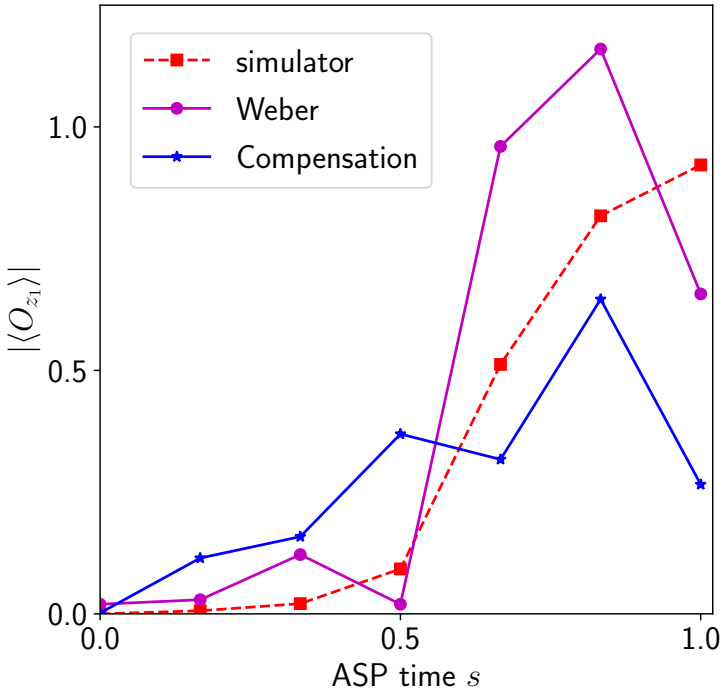

Figure 4.11: **Attempts to compensate for parasitic controlled phase by appending CPHASE.** Absolute value of the string order parameters O_{z_1} versus ASP time (s) in the ED phase for circuits with appended to each native two-qubit gate to compensate for the parasitic controlled phase; The data obtained from Weber and the noiseless data from the simulator are also shown. The compensated circuit performed worse likely due to the increase in the number of two-qubit gates. The parameters $J_1 = 0.2$, $J_1' = -1$, $J_2 = -0.1$, $B_z = 1.5$, $T = 3.0$ were used to prepare the ED phase.

The second approach is based on the observation that the phase present in the $|11\rangle$ can be removed at the expense of adding half the phase to the $|01\rangle$ and $|10\rangle$ using single-qubit Z rotations. Assuming that fidelity is a quadratic function of gate parameters, a higher fidelity can be obtained by splitting the phase into two. We tested this scheme by performing Floquet calibration to estimate the ϕ present on each qubit and used the average to perform single-qubit Z rotations on the qubits. The result is shown in Fig. 4.12. Although some improvement in the final value of the string order parameter is observed, the non-monotonic trend remains largely unchanged, indicating that manipulation of the parasitic phase is inadequate to remove the discrepancy.

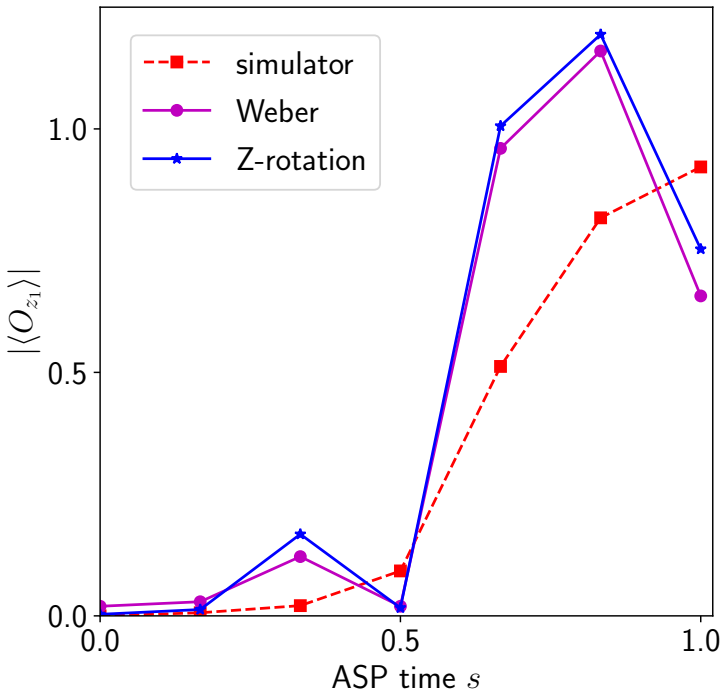

Figure 4.12: **Attempts to compensate for parasitic controlled phase by appending single qubit rotations.** Absolute value of the string order parameters O_{z_1} versus ASP time (s) in the ED phase for circuits with single-qubit Z rotations added to split the parasitic phase among two basis states. The data obtained from Weber and the noiseless data from the simulator are also shown. The qualitative trend of the string order parameter is qualitatively unchanged. The parameters $J_1 = 0.2$, $J_1' = -1$, $J_2 = -0.1$, $B_z = 1.5$, $T = 3.0$ were used to prepare the ED phase.

4.6 Conclusion

We now discuss the implications of our findings regarding the role of the parasitic phase in limiting gate depth for quantum simulation. Error mitigation strategies such as randomized compiling [131] may be applicable to mitigate coherent errors. However, in the present simulations, this protocol cannot be implemented because the two-qubit native gate does not commute with the Pauli group. Other strategies to mitigate coherent gate errors may be possible, but their effectiveness is in general problem-dependent. Supposing that the parasitic phase can be successfully mitigated, emulations using Cirq indicate that the maximum number of two-qubit gates is around 100 for the present simulations given reported error rates [115] which agrees well with the findings of a recent work which simulated correlated molecules and materials on the same device [132].

Given the capabilities of present quantum processors, we examine the resources required to prepare more complex chiral spin liquids that are thought to exist in

a spin-1/2 frustrated honeycomb with similar couplings studied in our work [122, 123, 133]. For a system size of 20 spins in a hexagonal lattice, corresponding to 4 unit cells, the total number of two-qubit gates required to implement a single Trotter step of the ASP trajectory is 210. Assuming six Trotter steps are needed in total, 1260 two-qubit gates would therefore be required. This value exceeds our estimate of the achievable gate depth by around an order of magnitude. Our results provide quantitative metrics regarding the improvements needed for future quantum devices to realize more exotic topological phases using ASP.

Chapter 5

SUMMARY AND OUTLOOK

In this thesis, we have tackled the challenging task of performing quantum simulation on NISQ devices from various perspectives. We have made significant strides in addressing this open problem and now summarize our key accomplishments. Additionally, we highlight the notable developments that have emerged from our research and outline promising avenues for future exploration, which have the potential to build upon our results and further advance the field of quantum simulation on NISQ devices.

5.1 Studying ground state properties using QITE

In this project, we validated the quantum primitive called quantum imaginary time evolution (QITE), which serves as a tool for determining ground state properties on quantum processors. Our results have demonstrated the feasibility of implementing these proposed schemes on NISQ devices, as well as experimentally validate their favorable comparison with the variational quantum eigensolver in terms of the required number of Pauli string measurements.

Based on our findings, we acknowledge the need for improvements to mitigate the influence of noise so as to apply QITE to larger system sizes. We propose two broad directions for exploration: (a) investigating methods to reduce the circuit complexities of QITE, thereby minimizing the introduction of noise when implementing the algorithm, and (b) evaluating the impact of new error mitigation strategies on the performance of QITE.

5.1.1 Reducing circuit complexities

Promising advancements have already been made in reducing the circuit complexities of QITE. Studies have demonstrated that symmetry considerations can reduce the number of operators required for constructing the unitary operators in QITE, consequently reducing the number of gates needed for implementing a Trotter step [86]. Moreover, circuit recompilation techniques have been employed to decrease the number of gate operations [86]. By leveraging these approaches, researchers have successfully employed QITE to study ground state properties of systems up to 10 qubits [86, 132].

Similarly, the utilization of new primitive gates like the three-qubit i-Toffoli gate [134] has been shown to reduce gate complexities in quantum simulation tasks [134], leading to a halving of the two-qubit gate counts. Therefore, it may prove fruitful to leverage these recent developments and explore ways to reduce the circuit complexities of QITE by incorporating these novel multi-qubit primitive gates into its implementation.

5.1.2 Evaluating new error mitigation strategies

An alternative approach is to conduct a thorough benchmarking of the impact of new error mitigation strategies on the performance of QITE. For example. coherent errors can have unpredictable effects on structured circuits like those utilized in QITE [131]. To address this issue, error mitigation techniques such as randomized compiling have emerged as a valuable tool [131]. Randomized compiling involves introducing random single-qubit gates to convert coherent errors into stochastic noise, thereby enhancing the performance of structured circuits. Notably, randomized compiling has been successfully applied to QITE, resulting in improved energy estimation and ground state fidelities [135].

These successful applications highlight the importance of systematically studying the impact of existing error mitigation strategies [46] on the performance of QITE. Conducting such a study will be crucial for unlocking the full potential of QITE on NISQ devices. By thoroughly evaluating and benchmarking different error mitigation approaches, we can gain insights into their effectiveness in mitigating noise and improving the overall performance of QITE.

5.2 Simulating finite temperature properties using QITE

In this study, we have explored the application of QITE to perform finite temperature simulations. We validated the method for computing thermal averages on a quantum computer by sampling minimally entangled typical thermal states (METTS) using QITE. This approach allowed us to demonstrate, for the first time, the computation of thermal averages on existing quantum hardware. Additionally, we developed a technique to evaluate the partition function and compute the free energy using QITE. We successfully validated our approach on NISQ devices and obtained accurate free energy estimates for a two-qubit system.

All of the schemes relied on utilizing QITE as a subroutine. Therefore, improvements to QITE, as discussed in Chapter 5.1, directly contribute to the performance enhancement of our proposed algorithms. For example, the utilization of symmetry

considerations and circuit recompilation enabled the study of the thermal properties of a $\alpha-$RuCl [132], a system known to exhibit spin liquid physics in its phase diagram [136]. The researchers were able to compute the thermal dynamical correlation functions of a 10-site $\alpha-$RuCl, representing one of the largest thermal simulations conducted using NISQ devices to date. This outcome underscores the significance of reducing circuit complexities and adopting new error mitigation strategies in extending the capability of NISQ devices for finite temperature simulations.

Moreover, it is worth delving into the possibilities of integrating QITE into other thermal simulation techniques. While we have successfully showcased the computation of thermal averages through METTS sampling, it is intriguing to explore the potential of QITE in generating other types of states that are pertinent to finite temperature simulations. Notably, recent advancements have utilized QITE to prepare canonical thermal pure states (CTPS) on NISQ devices [137]. CTPS exhibit favorable scaling properties and offer a promising approach for estimating thermal properties of quantum systems without the need for an escalating number of samples as the system size increases [137]. The exploration of QITE's applicability in preparing CTPS opens up exciting opportunities for advancing thermal simulations using NISQ devices.

5.3 Realizing symmetry protected topological phases on a quantum computer

In this project, we benchmark the capabilities of current state-of-the-art in preparing topological phases of matter. We experimentally realize the SPT phases of a 1-D next-nearest-neighbor hopping spin chain via adiabatic state preparation, and verified their experimental signatures on superconducting processors provided by Google Quantum AI.

Our results were achieved using classical recompilation schemes to reduce the two-qubit gate counts of our trotterized adiabatic state preparation circuits. Improvements in circuit compression techniques to reduce circuit complexities will thus allow for the preparation of topological phases in models where even more two-qubit gates are needed. The compression of time-dynamics circuits is an active area of research [138–140]. Hence, it may be worthwhile to leverage on such advances and perform a systematic evaluation of existing work to identify approaches that can be used to compress the circuits found commonly in adiabatic state preparation.

In our work, we also identified the presence of parasitic CPHASE noise, which negatively impacts the fidelity of our quantum program. Despite our attempts, we

were unable to successfully mitigate the influence of this hardware non-ideality. Consequently, this issue warrants further investigation.

One potential solution is to employ software-based methods to mitigate parasitic two-qubit gate errors [141]. The proposed approach involves Cartan's KAK decomposition, which counteracts parasitic two-qubit gates by exclusively applying single-qubit rotations, thereby eliminating the need for additional two-qubit gates. Experimental data from the study indicate that the unitary infidelity decreased by a factor of 3 compared to the noisy implementation. Exploring the applicability of such software mitigation strategies to improve the fidelity of adiabatic state preparation circuits would be a worthwhile endeavor.

5.4 Broader outlook for quantum simulation

We have presented our work to implement and benchmark several quantum simulation workflows on NISQ devices. However, it remains an open question on when and even if, quantum advantage can be achieved using NISQ devices for quantum simulation problems. Clearly, investigations to advance the state of quantum simulation on NISQ devices makes the most sense if there is strong evidence that suggests quantum advantage can be achieved pending more improvements in quantum computers, albeit just below the threshold for fault tolerance.

Recent investigations [142, 143] have been undertaken to systematically examine for what problems in quantum simulation can quantum advantage be achieved. Lee et. al. [142] have numerically investigated the ground state Hamiltonian problem across the quantum chemistry space, and their data suggests that it might be prudent to assume no exponential quantum advantage can be achieved with adiabatic state preparation or quantum phase estimation in this domain space. Their results do not rule out polynomial advantage.

Polynomial advantage depending on its form, could translate to practical quantum advantage [144]. This suggests that it is critical to begin investigating whether QITE can offer a polynomial speed-up for the Hamiltonian ground state problem, and if yes, whether QITE offer a speed-up beyond quadratic scaling. A similar investigation should be conducted for problems motivated by by finite temperature simulations. Babbush et. al. [143] has presented numerical evidence that certain problems in finite temperature simulation may be more amenable to quantum advantage. Investigating whether QITE can achieve this will provide a useful result to guide future experimental work on NISQ devices.

Appendix A

PAULI STRING REDUCTION METHOD OF QITE

This section is adapted from [86]. We introduced a scheme to reduce Pauli strings in the QITE unitaries by $\mathbb{Z}_2$ symmetries. We mentioned that rather than impose $\mathbb{Z}_2$ symmetries when choosing the Pauli strings in the QITE unitries, the original QITE algorithm subsumes the preservation of $\mathbb{Z}_2$ symmetries. We now state the proposition and present a proof that derives directly from the QITE linear systems.

Proposition. *Suppose QITE is applied to approximate the imaginary time propagator $e^{-\Delta\tau\hat{H}[l]}$ on the state $|\Psi\rangle$. If there exists a stabilizer $\mathcal{S}$ such that every element of $\mathcal{S}$ commutes with $\hat{H}[l]$ and $|\Psi\rangle \in V_{\mathcal{S}}$, then*
(a) The action of $e^{-i\Delta\tau\hat{G}[l]}$ on $|\Psi\rangle$ with $\sigma_\mu \in \mathcal{P}_{\hat{H}[l]}$ is equivalent to the action with $\sigma_\mu \in \mathcal{P}_{\hat{H}[l]} \cap \mathcal{N}(\mathcal{S})/\mathcal{S}$,
(b) $e^{-i\Delta\tau\hat{G}[l]}|\Psi\rangle \in V_{\mathcal{S}}$.

Proof. Pick $\sigma_\mu \notin \mathcal{N}(\mathcal{S})$. Since $e^{-\Delta\tau\hat{H}[l]}$ commutes with elements of $\mathcal{S}$ and $|\Psi\rangle \in V_{\mathcal{S}}$, for any $s \in \mathcal{S}$ we have $\langle\Psi| e^{-\Delta\tau\hat{H}[l]}\sigma_\mu s |\Psi\rangle = -\langle\Psi| s\, e^{-\Delta\tau\hat{H}[l]}\sigma_\mu |\Psi\rangle$, which implies $\langle\Psi| e^{-\Delta\tau\hat{H}[l]}\sigma_\mu |\Psi\rangle = 0$. Hence

$$b[l]_\mu = \frac{\Im\langle\Psi|e^{-\Delta\tau\hat{H}[l]}\sigma_\mu|\Psi\rangle}{\Delta\tau c[l]^{1/2}} = 0 \tag{A.1}$$

Now fix the column index ν such that $\sigma_\nu \in \mathcal{N}(\mathcal{S})$, then for any $s \in \mathcal{S}$, $\langle\Psi|\sigma_\mu\sigma_\nu s|\Psi\rangle = -\langle\Psi| s\,\sigma_\mu\sigma_\nu |\Psi\rangle$, which implies $\langle\Psi|\sigma_\mu\sigma_\nu|\Psi\rangle = 0$. Hence

$$A_{\mu\nu} = \Re(\langle\Psi|\sigma_\mu\sigma_\nu|\Psi\rangle) = 0 \tag{A.2}$$

Since $\boldsymbol{A}$ is Hermitian and real, $A_{\nu\mu} = A^*_{\mu\nu} = A_{\mu\nu} = 0$. Thus the linear system has the block-diagonal form

$$\begin{pmatrix} \boldsymbol{A}\boldsymbol{l}' & 0 \\ 0 & \boldsymbol{A}\boldsymbol{l}'' \end{pmatrix}\begin{pmatrix} \boldsymbol{x}\boldsymbol{l}' \\ \boldsymbol{x}\boldsymbol{l}'' \end{pmatrix} = \begin{pmatrix} \boldsymbol{b}\boldsymbol{l}' \\ 0 \end{pmatrix}, \tag{A.3}$$

where the quantities with single primes are indexed by $\boldsymbol{\mu}$ such that $\sigma_\mu \in \mathcal{N}(\mathcal{S})$ and those with double primes are indexed by $\boldsymbol{\mu}$ such that $\sigma_\mu \notin \mathcal{N}(\mathcal{S})$. By setting $\boldsymbol{x}\boldsymbol{l}''$ to 0, the linear system is reduced to $\boldsymbol{A}\boldsymbol{l}'\boldsymbol{x}\boldsymbol{l}' = \boldsymbol{b}\boldsymbol{l}'$.

To show that the set of σ_μ can be reduced from $\mathcal{N}(\mathcal{S})$ to $\mathcal{N}(\mathcal{S})/\mathcal{S}$, suppose σ_μ and $\sigma_{\mu'}$ belong to the same coset in $\mathcal{N}(\mathcal{S})/\mathcal{S}$, then $\sigma_{\mu'} = \pm\sigma_\mu s$ for some $s \in \mathcal{S}$. In the QITE unitary $e^{-i\Delta\tau\hat{G}[l]} = \sum_{k=0}^{\infty}(-i\Delta\tau)^k(\sum_\mu x[l]_\mu\sigma_\mu)^k$, each term in the sum is a power of $-i\Delta\tau$ times a product of the form $\prod_\nu(x[l]_\nu\sigma_\nu)$. If a product term contains $x[l]_{\mu'}\sigma_{\mu'}$, the action of this term on $|\Psi\rangle$ is proportional to

$$\left(\prod_{\nu''} x[l]_{\nu''}\sigma_{\nu''}\right)(x[l]_{\mu'}\sigma_{\mu'})\left(\prod_{\nu'} x[l]_{\nu'}\sigma_{\nu'}\right)|\Psi\rangle \tag{A.4}$$

In the product over $\boldsymbol{\nu'}$, each $\sigma_{\nu'} \in \mathcal{N}(\mathcal{S})$, so $\prod_{\nu'}(x[l]_{\nu'}\sigma_{\nu'})|\Psi\rangle \in V_\mathcal{S}$. Then Eq. (A.4) is equivalent to

$$\left(\prod_{\nu''} x[l]_{\nu''}\sigma_{\nu''}\right)(\pm x[l]_{\mu'}\sigma_\mu)\left(\prod_{\nu'} x[l]_{\nu'}\sigma_{\nu'}\right)|\Psi\rangle \tag{A.5}$$

Since this applies to every pair of Pauli strings in the same coset, $\hat{G}[l]$ can be written as

$$\hat{G}[l] = \sum_{\boldsymbol{\mu}} \widetilde{x[l]}_\mu\sigma_\mu, \tag{A.6}$$

where $\boldsymbol{\mu}$ is chosen such that $\sigma_\mu \in \mathcal{P}_{\hat{H}[l]} \cap \mathcal{N}(\mathcal{S})/\mathcal{S}$, $\widetilde{x[l]}_\mu = \sum_{\mu'}\eta_{\mu'}x[l]_{\mu'}$, $\eta_{\mu'} = \pm 1$ and $\boldsymbol{\mu'}$ is chosen such that $\sigma_{\mu'} \in \sigma_\mu\mathcal{S}$.

Since all Pauli strings on the exponent of $e^{-i\Delta\tau\hat{G}[l]}$ commute with elements of $\mathcal{S}$, $e^{-i\Delta\tau\hat{G}[l]}$ commutes with elements of $\mathcal{S}$ and hence $e^{-i\Delta\tau\hat{G}[l]}|\Psi\rangle \in V_\mathcal{S}$. □

Our Pauli string reduction scheme is related to the qubit encoding scheme that removes redundant qubits by exploiting $\mathbb{Z}_2$ symmetries reported in Ref. [145]. In the qubit encoding scheme, a Hamiltonian over some number of qubits is transformed to another Hamiltonian over a smaller number of qubits by a series of Clifford gates. Our Pauli string reduction scheme coincides with the qubit encoding scheme when the domain size D equals the total number of qubits N, in the sense that the reduced set of Pauli strings in our scheme exactly corresponds to all Pauli strings in the encoded Hamiltonian with redundant qubits removed in the qubit encoding scheme.

However, because the weight of a Pauli string can change during the Clifford transformation, the two schemes differ when $D < N$. On the one hand, some Pauli strings can decrease in weight after encoding. If we include all Pauli strings with domain size D in the encoded Hamiltonian, these Pauli strings might include those with domain size $D' > D$ in the original Hamiltonian, thus increasing the total number

of Pauli strings. On the other hand, some Pauli strings can increase in weight after encoding and result in an increased cost of the QITE algorithm. As an example, consider performing QITE on a Hamiltonian with periodic boundary condition and the $\mathbb{Z}_2$ symmetry $Z_0Z_1Z_2Z_3$. One of the $D = 2$ Pauli strings is X_0Y_3. In the qubit encoding scheme, the symmetry operator $Z_0Z_1Z_2Z_3$ is transformed to Z_3 so that qubit 3 can be eliminated, but the weight-two Pauli string X_0Y_3 is transformed to the higher-weight Pauli string $X_0X_1Y_2$, thus requiring a larger QITE domain and increasing the overall cost of the algorithm. Therefore, in the present work, we use $\mathbb{Z}_2$ symmetries to reduce the number of Pauli strings in the QITE unitaries rather than eliminate redundant qubits.

BIBLIOGRAPHY

1. Dirac, P. A. M. & Fowler, R. H. Quantum mechanics of many-electron systems. *Proceedings of the Royal Society of London. Series A, Containing Papers of a Mathematical and Physical Character* **123,** 714–733. eprint: https://royalsocietypublishing.org/doi/pdf/10.1098/rspa.1929.0094. https://royalsocietypublishing.org/doi/abs/10.1098/rspa.1929.0094 (1929).

2. *Press release. NobelPrize.org. Nobel Prize Outreach* Accessed: 2023-04-29. https://www.nobelprize.org/prizes/chemistry/1998/press-release/.

3. Feynman, R. P. Simulating physics with computers. *Int. J. Theor. Phys.* **21,** 467–488. https://doi.org/10.1007/BF02650179 (1982).

4. Lloyd, S. Universal Quantum Simulators. *Science* **273,** 1073–1078. http://science.sciencemag.org/content/273/5278/1073 (1996).

5. Abrams, D. S. & Lloyd, S. Simulation of Many-Body Fermi Systems on a Universal Quantum Computer. *Phys. Rev. Lett.* **79,** 2586–2589. https://link.aps.org/doi/10.1103/PhysRevLett.79.2586 (13 1997).

6. Hubbard, J. Electron Correlations in Narrow Energy Bands. *Proc. R. Soc. London, Ser. A* **276,** 238–257. http://rspa.royalsocietypublishing.org/content/276/1365/238.abstract (1963).

7. Abrams, D. S. & Lloyd, S. Quantum Algorithm Providing Exponential Speed Increase for Finding Eigenvalues and Eigenvectors. *Phys. Rev. Lett.* **83,** 5162–5165. https://link.aps.org/doi/10.1103/PhysRevLett.83.5162 (24 1999).

8. Aspuru-Guzik, A., Dutoi, A. D., Love, P. J. & Head-Gordon, M. Simulated Quantum Computation of Molecular Energies. *Science* **309,** 1704–1707. http://science.sciencemag.org/content/309/5741/1704 (2005).

9. Kassal, I., Jordan, S. P., Love, P. J., Mohseni, M. & Aspuru-Guzik, A. Polynomial-time quantum algorithm for the simulation of chemical dynamics. *Proceedings of the National Academy of Sciences* **105,** 18681–18686. eprint: https://www.pnas.org/doi/pdf/10.1073/pnas.0808245105. https://www.pnas.org/doi/abs/10.1073/pnas.0808245105 (2008).

10. Du, J., Xu, N., Peng, X., Wang, P., Wu, S., *et al.* NMR Implementation of a Molecular Hydrogen Quantum Simulation with Adiabatic State Preparation. *Phys. Rev. Lett.* **104,** 030502. https://link.aps.org/doi/10.1103/PhysRevLett.104.030502 (3 Jan. 2010).

11. Georgescu, I. M., Ashhab, S. & Nori, F. Quantum simulation. *Rev. Mod. Phys.* **86,** 153–185. https://link.aps.org/doi/10.1103/RevModPhys.86.153 (1 Mar. 2014).

12. Greiner, M., Mandel, O., Esslinger, T., Hansch, T. W. & Bloch, I. Quantum phase transition from a superfluid to a Mott insulator in a gas of ultracold atoms. *Nature* **415,** 39–44. ISSN: 00280836. http://dx.doi.org/10.1038/415039a (Jan. 2002).

13. Kinoshita, T., Wenger, T. & Weiss, D. S. Observation of a One-Dimensional Tonks-Girardeau Gas. *Science* **305,** 1125–1128. eprint: https://www.science.org/doi/pdf/10.1126/science.1100700. https://www.science.org/doi/abs/10.1126/science.1100700 (2004).

14. Schneider, U., Hackermüller, L., Will, S., Best, T., Bloch, I., *et al.* Metallic and Insulating Phases of Repulsively Interacting Fermions in a 3D Optical Lattice. *Science* **322,** 1520–1525. eprint: https://www.science.org/doi/pdf/10.1126/science.1165449. https://www.science.org/doi/abs/10.1126/science.1165449 (2008).

15. Neeley, M., Ansmann, M., Bialczak, R. C., Hofheinz, M., Lucero, E., *et al.* Emulation of a Quantum Spin with a Superconducting Phase Qudit. *Science* **325,** 722–725. eprint: https://www.science.org/doi/pdf/10.1126/science.1173440. https://www.science.org/doi/abs/10.1126/science.1173440 (2009).

16. Bauer, B., Bravyi, S., Motta, M. & Kin-Lic Chan, G. Quantum Algorithms for Quantum Chemistry and Quantum Materials Science. *Chem. Rev.* **120,** 12685–12717. https://doi.org/10.1021/acs.chemrev.9b00829 (22 Nov. 2020).

17. Kitaev, A. Y. Quantum computations: algorithms and error correction. *Russian Mathematical Surveys* **52,** 1191–1249. https://doi.org/10.1070/rm1997v052n06abeh002155 (Dec. 1997).

18. Deutsch, D. E. & Penrose, R. Quantum computational networks. *Proceedings of the Royal Society of London. A. Mathematical and Physical Sciences* **425,** 73–90. eprint: https://royalsocietypublishing.org/doi/pdf/10.1098/rspa.1989.0099. https://royalsocietypublishing.org/doi/abs/10.1098/rspa.1989.0099 (1989).

19. Raussendorf, R. & Briegel, H. J. A One-Way Quantum Computer. *Phys. Rev. Lett.* **86,** 5188–5191. https://link.aps.org/doi/10.1103/PhysRevLett.86.5188 (22 May 2001).

20. Aharonov, D., van Dam, W., Kempe, J., Landau, Z., Lloyd, S., *et al. Adiabatic quantum computation is equivalent to standard quantum computation* in *45th Annual IEEE Symposium on Foundations of Computer Science* (2004), 42–51.

21. Nielsen, M. A. & Chuang, I. L. *Quantum Computation and Quantum Information* ISBN: 9781107002173 (Cambridge University Press, 2000).

22. Kitaev, A. Y. *Quantum measurements and the Abelian Stabilizer Problem* 1995. eprint: arXiv:quant-ph/9511026.

23. *Quantum protocols and quantum algorithms* Accessed: 2023-04-29. https://learn.qiskit.org/course/ch-algorithms/quantum-phase-estimation.

24. Suzuki, M. General theory of fractal path integrals with applications to many-body theories and statistical physics. *Journal of Mathematical Physics* **32,** 400–407. ISSN: 0022-2488. eprint: https://pubs.aip.org/aip/jmp/article-pdf/32/2/400/8160505/400_1_online.pdf. https://doi.org/10.1063/1.529425 (Feb. 1991).

25. Hatano, N. & Suzuki, M. in *Quantum Annealing and Other Optimization Methods* (eds Das, A. & K. Chakrabarti, B.) 37–68 (Springer Berlin Heidelberg, Berlin, Heidelberg, 2005). ISBN: 978-3-540-31515-5. https://doi.org/10.1007/11526216_2.

26. *Rigetti computing: quantum cloud services* https:// qcs . rigetti . com / dashboard. Accessed: 2019-01-21.

27. *Qiskit runtime* Accessed: 2023-04-29. https://cloud.ibm.com/quantum.

28. *Google Quantum AI: Explore our quantum software* Accessed: 2023-04-29. https://quantumai.google/software.

29. *Aquila: Our 256-qubit quantum processor* Accessed: 2023-04-29. https://www.quera.com/aquila.

30. *IonQ harmony* Accessed: 2023-04-29. https://ionq.com/quantum-systems/harmony.

31. *Quantum Computing: Progress and Prospects* (eds Grumbling, E. & Horowitz, M.) ISBN: 978-0-309-47969-1. https://nap.nationalacademies.org/catalog/25196/quantum-computing-progress-and-prospects (The National Academies Press, 2019).

32. Koch, J., Yu, T. M., Gambetta, J., Houck, A. A., Schuster, D. I., *et al.* Charge-insensitive qubit design derived from the Cooper pair box. *Phys. Rev. A* **76,** 042319. https://link.aps.org/doi/10.1103/PhysRevA.76.042319 (4 Oct. 2007).

33. Schreier, J. A., Houck, A. A., Koch, J., Schuster, D. I., Johnson, B. R., *et al.* Suppressing charge noise decoherence in superconducting charge qubits. *Phys. Rev. B* **77,** 180502. https://link.aps.org/doi/10.1103/PhysRevB.77.180502 (18 May 2008).

34. Kjaergaard, M., Schwartz, M. E., Braumüller, J., Krantz, P., Wang, J. I.-J., *et al.* Superconducting Qubits: Current State of Play. *Annual Review of Condensed Matter Physics* **11,** 369–395. eprint: https://doi.org/10.1146/annurev-conmatphys-031119-050605. https://doi.org/10.1146/annurev-conmatphys-031119-050605 (2020).

35. Arute, F., Arya, K., Babbush, R., Bacon, D., Bardin, J., *et al.* Quantum Supremacy using a Programmable Superconducting Processor. *Nature* **574,** 505–510. https://www.nature.com/articles/s41586-019-1666-5 (2019).

36. Bruzewicz, C. D., Chiaverini, J., McConnell, R. & Sage, J. M. Trapped-ion quantum computing: Progress and challenges. *Applied Physics Reviews* **6.** 021314. ISSN: 1931-9401. eprint: https://pubs.aip.org/aip/apr/article-pdf/doi/10.1063/1.5088164/14577412/021314_1_online.pdf. https://doi.org/10.1063/1.5088164 (May 2019).

37. Saffman, M. Quantum computing with atomic qubits and Rydberg interactions: progress and challenges. *Journal of Physics B: Atomic, Molecular and Optical Physics* **49,** 202001. https://dx.doi.org/10.1088/0953-4075/49/20/202001 (Oct. 2016).

38. Henriet, L., Beguin, L., Signoles, A., Lahaye, T., Browaeys, A., *et al.* Quantum computing with neutral atoms. *Quantum* **4,** 327. ISSN: 2521-327X. https://doi.org/10.22331/q-2020-09-21-327 (Sept. 2020).

39. *Software-tailored architectures for quantum co-design* Accessed: 2023-04-29. http://staq.pratt.duke.edu/.

40. *UW–Madison, industry partners run quantum algorithm on neutral atom quantum computer for the first time* Accessed: 2023-04-29. https://news.wisc.edu/uw-madison-industry-partners-run-quantum-algorithm-on-neutral-atom-quantum-computer-for-the-first-time/.

41. Preskill, J. Quantum Computing in the NISQ era and beyond. *Quantum* **2,** 79. ISSN: 2521-327X. https://doi.org/10.22331/q-2018-08-06-79 (Aug. 2018).

42. Preskill, J. *Lecture Notes for Physics 229:Quantum Information and Computation* ISBN: 9781506189918. https://books.google.com/books?id=MIv8rQEACAAJ (CreateSpace Independent Publishing Platform, 2015).

43. Bravyi, S., Sheldon, S., Kandala, A., Mckay, D. C. & Gambetta, J. M. Mitigating measurement errors in multiqubit experiments. *Phys. Rev. A* **103,** 042605. https://link.aps.org/doi/10.1103/PhysRevA.103.042605 (4 Apr. 2021).

44. Greenbaum, D. & Dutton, Z. Modeling coherent errors in quantum error correction. *Quantum Science and Technology* **3,** 015007. https://dx.doi.org/10.1088/2058-9565/aa9a06 (Dec. 2017).

45. Debroy, D. M., Li, M., Newman, M. & Brown, K. R. Stabilizer Slicing: Coherent Error Cancellations in Low-Density Parity-Check Stabilizer Codes. *Phys. Rev. Lett.* **121,** 250502. https://link.aps.org/doi/10.1103/PhysRevLett.121.250502 (25 Dec. 2018).

46. Cai, Z., Babbush, R., Benjamin, S. C., Endo, S., Huggins, W. J., *et al.* Quantum error mitigation. *arXiv preprint arXiv:2210.00921* (2022).

47. McArdle, S., Yuan, X. & Benjamin, S. Error-Mitigated Digital Quantum Simulation. *Phys. Rev. Lett.* **122,** 180501. https://link.aps.org/doi/10.1103/PhysRevLett.122.180501 (18 May 2019).

48. Bonet-Monroig, X., Babbush, R. & O'Brien, T. E. Nearly Optimal Measurement Scheduling for Partial Tomography of Quantum States. *Phys. Rev. X* **10,** 031064. https://link.aps.org/doi/10.1103/PhysRevX.10.031064 (3 Sept. 2020).

49. Motta, M., Sun, C., Tan, A. T. K., O'Rourke, M. J., Ye, E., *et al.* Determining eigenstates and thermal states on a quantum computer using quantum imaginary time evolution. *Nat. Phys.* ISSN: 1745-2481. https://doi.org/10.1038/s41567-019-0704-4 (2019).

50. **Tan, Adrian T.K.**, Sun, S.-N., Tazhigulov, R. N., Chan, G. K.-L. & Minnich, A. J. Realizing symmetry-protected topological phases in a spin-1/2 chain with next-nearest neighbor hopping on superconducting qubits. *Phys. Rev. A* **107,** 032614. https://link.aps.org/doi/10.1103/PhysRevA.107.032614 (3 2023).

    Contributions A.T.K.T. conceptualized the project, designed and optimized the quantum circuits, carried out the simulation runs on the quantum computers, performed simulations and analyzed the experimental data, and wrote the manuscript.

51. Lee, S., Lee, J., Zhai, H., Tong, Y., Dalzell, A., *et al.* Evaluating the Evidence for Exponential Quantum Advantage in Ground-State Quantum Chemistry. *Nature Communications* **14.** https://www.nature.com/articles/s41467-023-37587-6 (2023).

52. Kitaev, A. Y., Shen, A. H. & Vyalyi, M. N. *Classical and Quantum Computation* ISBN: 0821832298 (American Mathematical Society, USA, 2002).

53. Schuch, N. & Verstraete, F. Computational complexity of interacting electrons and fundamental limitations of density functional theory. eng. *NATURE PHYSICS* **5,** 732–735. ISSN: 1745-2473. http://dx.doi.org/10.1038/NPHYS1370 (2009).

54. Dobšíček, M., Johansson, G., Shumeiko, V. & Wendin, G. Arbitrary accuracy iterative quantum phase estimation algorithm using a single ancillary qubit: A two-qubit benchmark. *Phys. Rev. A* **76,** 030306. https://link.aps.org/doi/10.1103/PhysRevA.76.030306 (3 Sept. 2007).

55. Svore, K. M., Hastings, M. B. & Freedman, M. Faster Phase Estimation. *Quantum Info. Comput.* **14,** 306–328. ISSN: 1533-7146 (Mar. 2014).

56. Wiebe, N. & Granade, C. Efficient Bayesian Phase Estimation. *Phys. Rev. Lett.* **117,** 010503. https://link.aps.org/doi/10.1103/PhysRevLett.117.010503 (1 June 2016).

57. Poulin, D., Kitaev, A., Steiger, D. S., Hastings, M. B. & Troyer, M. Quantum Algorithm for Spectral Measurement with a Lower Gate Count. *Phys. Rev. Lett.* **121,** 010501. https://link.aps.org/doi/10.1103/PhysRevLett.121.010501 (1 July 2018).

58. O'Malley, P. J. J., Babbush, R., Kivlichan, I. D., Romero, J., McClean, J. R., *et al.* Scalable Quantum Simulation of Molecular Energies. *Phys. Rev. X* **6,** 031007. https://link.aps.org/doi/10.1103/PhysRevX.6.031007 (3 July 2016).

59. Peruzzo, A., McClean, J., Shadbolt, P., Yung, M.-H., Zhou, X.-Q., *et al.* A variational eigenvalue solver on a photonic quantum processor. *Nat. Commun.* **5,** 4213. ISSN: 2041-1723. https://doi.org/10.1038/ncomms5213 (2014).

60. Cerezo, M., Arrasmith, A., Babbush, R., Benjamin, S. C., Endo, S., *et al.* Variational quantum algorithms. *Nature Reviews Physics* **3,** 625–644. ISSN: 2522-5820. https://doi.org/10.1038/s42254-021-00348-9 (Sept. 2021).

61. Szabo, A. & Ostlund, N. S. *Modern Quantum Chemistry: Introduction to Advanced Electronic Structure Theory* First (Dover Publications, Inc., Mineola, 1996).

    This is the revised first edition, originally published in 1989 by McGraw-Hill Publishing Company, New York, with an additional section written by M. C. Zerner. First edition originally published in 1982.

62. Bharti, K., Cervera-Lierta, A., Kyaw, T. H., Haug, T., Alperin-Lea, S., *et al.* Noisy intermediate-scale quantum algorithms. *Rev. Mod. Phys.* **94,** 015004. https://link.aps.org/doi/10.1103/RevModPhys.94.015004 (1 Feb. 2022).

63. Kandala, A., Mezzacapo, A., Temme, K., Takita, M., Brink, M., *et al.* Hardware-efficient variational quantum eigensolver for small molecules and quantum magnets. *Nature* **549,** 242–246. https://doi.org/10.1038/nature23879 (Sept. 2017).

64. Hempel, C., Maier, C., Romero, J., McClean, J., Monz, T., *et al.* Quantum Chemistry Calculations on a Trapped-Ion Quantum Simulator. *Phys. Rev. X* **8,** 031022. https://link.aps.org/doi/10.1103/PhysRevX.8.031022 (3 July 2018).

65. McClean, J. R., Boixo, S., Smelyanskiy, V. N., Babbush, R. & Neven, H. Barren plateaus in quantum neural network training landscapes. *Nat. Commun.* **9,** 4812. ISSN: 2041-1723. https://doi.org/10.1038/s41467-018-07090-4 (2018).

66. Sakurai, J. J. & Napolitano, J. *Modern Quantum Mechanics* 2nd ed. (Cambridge University Press, 2017).

67. Lehtovaara, L., Toivanen, J. & Eloranta, J. Solution of time-independent Schrödinger equation by the imaginary time propagation method. *Journal of Computational Physics* **221,** 148–157. ISSN: 0021-9991. https://www.sciencedirect.com/science/article/pii/S0021999106002798 (2007).

68. Hastings, M. B. & Koma, T. Spectral Gap and Exponential Decay of Correlations. *Comm. Math. Phys.* **265,** 781–804. https://doi.org/10.1007/s00220-006-0030-4 (2006).

69. McClean, J. R., Kimchi-Schwartz, M. E., Carter, J. & de Jong, W. A. Hybrid quantum-classical hierarchy for mitigation of decoherence and determination of excited states. *Phys. Rev. A* **95,** 042308. https://link.aps.org/doi/10.1103/PhysRevA.95.042308 (4 Apr. 2017).

70. Colless, J. I., Ramasesh, V. V., Dahlen, D., Blok, M. S., Kimchi-Schwartz, M. E., *et al.* Computation of Molecular Spectra on a Quantum Processor with an Error-Resilient Algorithm. *Phys. Rev. X* **8,** 011021. https://link.aps.org/doi/10.1103/PhysRevX.8.011021 (1 Feb. 2018).

71. *Welcome to the Docs for pyQuil!* https:// pyquil-docs . rigetti . com / en / stable/. Accessed: 2023-05-02.

72. ANIS, M. S., Abraham, H., AduOffei, Agarwal, R., Agliardi, G., *et al. Qiskit: An Open-source Framework for Quantum Computing* 2021.

73. Lee, P. A., Nagaosa, N. & Wen, X.-G. Doping a Mott insulator: Physics of high-temperature superconductivity. *Rev. Mod. Phys.* **78,** 17–85. https://link.aps.org/doi/10.1103/RevModPhys.78.17 (1 Jan. 2006).

74. Terhal, B. M. & DiVincenzo, D. P. Problem of equilibration and the computation of correlation functions on a quantum computer. *Phys. Rev. A* **61,** 022301. https://link.aps.org/doi/10.1103/PhysRevA.61.022301 (2 2000).

75. Poulin, D. & Wocjan, P. Sampling from the Thermal Quantum Gibbs State and Evaluating Partition Functions with a Quantum Computer. *Phys. Rev. Lett.* **103,** 220502. https://link.aps.org/doi/10.1103/PhysRevLett.103.220502 (22 Nov. 2009).

76. Riera, A., Gogolin, C. & Eisert, J. Thermalization in Nature and on a Quantum Computer. *Phys. Rev. Lett.* **108,** 080402. https://link.aps.org/doi/10.1103/PhysRevLett.108.080402 (8 Feb. 2012).

77. Temme, K., Osborne, T. J., Vollbrecht, K. G., Poulin, D. & Verstraete, F. Quantum Metropolis sampling. *Nature* **471,** 87. https://doi.org/10.1038/nature09770 (2011).

78. Yung, M.-H. & Aspuru-Guzik, A. A quantum–quantum Metropolis algorithm. *Proceedings of the National Academy of Sciences* **109,** 754–759. eprint: https://www.pnas.org/doi/pdf/10.1073/pnas.1111758109. https://www.pnas.org/doi/abs/10.1073/pnas.1111758109 (2012).

79. Stoudenmire, E. M. & White, S. R. Minimally entangled typical thermal state algorithms. *New J. Phys.* **12,** 055026. http://stacks.iop.org/1367-2630/12/i=5/a=055026 (2010).

80. Martyn, J. & Swingle, B. Product spectrum ansatz and the simplicity of thermal states. *Phys. Rev. A* **100,** 032107. https://link.aps.org/doi/10.1103/PhysRevA.100.032107 (3 Sept. 2019).

81. Wu, J. & Hsieh, T. H. Variational Thermal Quantum Simulation via Thermofield Double States. *Phys. Rev. Lett.* **123,** 220502. https://link.aps.org/doi/10.1103/PhysRevLett.123.220502 (22 Nov. 2019).

82. Verdon, G., Marks, J., Nanda, S., Leichenauer, S. & Hidary, J. *Quantum Hamiltonian-Based Models and the Variational Quantum Thermalizer Algorithm* 2019. arXiv: 1910.02071 [quant-ph].

83. Francis, A., Zhu, D., Alderete, C. H., Johri, S., Xiao, X., *et al.* Many-body thermodynamics on quantum computers via partition function zeros. *Science Advances* **7,** eabf2447. eprint: https://www.science.org/doi/pdf/10.1126/sciadv.abf2447. https://www.science.org/doi/abs/10.1126/sciadv.abf2447 (2021).

84. Bassman Oftelie, L., Klymko, K., Liu, D., Tubman, N. M. & de Jong, W. A. Computing Free Energies with Fluctuation Relations on Quantum Computers. *Phys. Rev. Lett.* **129,** 130603. https://link.aps.org/doi/10.1103/PhysRevLett.129.130603 (13 Sept. 2022).

85. Geller, M. R., Holmes, Z., Coles, P. J. & Sornborger, A. Experimental quantum learning of a spectral decomposition. *Phys. Rev. Res.* **3,** 033200. https://link.aps.org/doi/10.1103/PhysRevResearch.3.033200 (3 Aug. 2021).

86. Sun, S.-N., Motta, M., Tazhigulov, R. N., Tan, A. T., Chan, G. K.-L., *et al.* Quantum Computation of Finite-Temperature Static and Dynamical Properties of Spin Systems Using Quantum Imaginary Time Evolution. *PRX Quantum* **2,** 010317. https://link.aps.org/doi/10.1103/PRXQuantum.2.010317 (1 Feb. 2021).

87. *Device backend noise model simulations* https:// qiskit.org /documentation/tutorials /simulators /2_device_noise_ simulation.html. Accessed: 2023-05-5.

88. Raedt, H. D., Hams, A. H., Michielsen, K., Miyashita, S. & Saito, K. Quantum Statistical Mechanics on a Quantum Computer. *Progress of Theoretical Physics Supplement* **138,** 489–494. ISSN: 0375-9687. eprint: https://academic.oup.com/ptps/article-pdf/doi/10.1143/PTPS.138.489/5313554/138-489.pdf. https://doi.org/10.1143/PTPS.138.489 (Apr. 2000).

89. Elsayed, T. A. & Fine, B. V. Regression Relation for Pure Quantum States and Its Implications for Efficient Computing. *Phys. Rev. Lett.* **110,** 070404. https://link.aps.org/doi/10.1103/PhysRevLett.110.070404 (7 Feb. 2013).

90. Steinigeweg, R., Gemmer, J. & Brenig, W. Spin-Current Autocorrelations from Single Pure-State Propagation. *Phys. Rev. Lett.* **112,** 120601. https://link.aps.org/doi/10.1103/PhysRevLett.112.120601 (12 Mar. 2014).

91. Hasan, M. Z. & Kane, C. L. Colloquium: Topological insulators. *Rev. Mod. Phys.* **82,** 3045–3067. https://link.aps.org/doi/10.1103/RevModPhys.82.3045 (4 Nov. 2010).

92. Qi, X.-L. & Zhang, S.-C. Topological insulators and superconductors. *Rev. Mod. Phys.* **83,** 1057–1110. https://link.aps.org/doi/10.1103/RevModPhys.83.1057 (4 Oct. 2011).

93. Senthil, T. Symmetry-Protected Topological Phases of Quantum Matter. *Annual Review of Condensed Matter Physics* **6,** 299–324. https://doi.org/10.1146/annurev-conmatphys-031214-014740 (2015).

94. Wen, X.-G. Colloquium: Zoo of quantum-topological phases of matter. *Rev. Mod. Phys.* **89,** 041004. https://link.aps.org/doi/10.1103/RevModPhys.89.041004 (4 Dec. 2017).

95. Atala, M., Aidelsburger, M., Barreiro, J. T., Abanin, D., Kitagawa, T., *et al.* Direct measurement of the Zak phase in topological Bloch bands. *Nature Physics* **9,** 795–800. ISSN: 1745-2481. https://doi.org/10.1038/nphys2790 (Dec. 2013).

96. Jotzu, G., Messer, M., Desbuquois, R., Lebrat, M., Uehlinger, T., *et al.* Experimental realization of the topological Haldane model with ultracold fermions. *Nature* **515,** 237–240. ISSN: 1476-4687. https://doi.org/10.1038/nature13915 (Nov. 2014).

97. Aidelsburger, M., Lohse, M., Schweizer, C., Atala, M., Barreiro, J. T., *et al.* Measuring the Chern number of Hofstadter bands with ultracold bosonic atoms. *Nature Physics* **11,** 162–166. ISSN: 1745-2481. https://doi.org/10.1038/nphys3171 (Feb. 2015).

98. Tan, X., Zhang, D.-W., Liu, Q., Xue, G., Yu, H.-F., *et al.* Topological Maxwell Metal Bands in a Superconducting Qutrit. *Phys. Rev. Lett.* **120,** 130503. https://link.aps.org/doi/10.1103/PhysRevLett.120.130503 (13 Mar. 2018).

99. Nakajima, S., Tomita, T., Taie, S., Ichinose, T., Ozawa, H., *et al.* Topological Thouless pumping of ultracold fermions. *Nature Physics* **12,** 296–300. https://doi.org/10.1038/nphys3622 (Apr. 2016).

100. Lohse, M., Schweizer, C., Zilberberg, O., Aidelsburger, M. & Bloch, I. A Thouless quantum pump with ultracold bosonic atoms in an optical superlattice. *Nature Physics* **12,** 350–354. https://doi.org/10.1038/nphys3584 (Apr. 2016).

101. Lohse, M., Schweizer, C., Price, H. M., Zilberberg, O. & Bloch, I. Exploring 4D quantum Hall physics with a 2D topological charge pump. *Nature* **553,** 55–58. ISSN: 1476-4687. https://doi.org/10.1038/nature25000 (Jan. 2018).

102. Leder, M., Grossert, C., Sitta, L., Genske, M., Rosch, A., *et al.* Real-space imaging of a topologically protected edge state with ultracold atoms in an amplitude-chirped optical lattice. *Nature Communications* **7,** 13112. https://doi.org/10.1038/ncomms13112 (2016).

103. Meier, E. J., An, F. A. & Gadway, B. Observation of the topological soliton state in the Su–Schrieffer–Heeger model. *Nature Communications* **7,** 13986. https://doi.org/10.1038/ncomms13986 (2016).

104. Song, B., Zhang, L., He, C., Poon, T. F. J., Hajiyev, E., *et al.* Observation of symmetry-protected topological band with ultracold fermions. *Science Advances* **4,** eaao4748. https://www.science.org/doi/abs/10.1126/sciadv.aao4748 (2018).

105. Xie, D., Gou, W., Xiao, T., Gadway, B. & Yan, B. Topological characterizations of an extended Su–Schrieffer–Heeger model. *npj Quantum Information* **5,** 55. https://doi.org/10.1038/s41534-019-0159-6 (May 2019).

106. De Léséleuc, S., Lienhard, V., Scholl, P., Barredo, D., Weber, S., *et al.* Observation of a symmetry-protected topological phase of interacting bosons with Rydberg atoms. *Science* **365,** 775–780. ISSN: 0036-8075. https://science.sciencemag.org/content/365/6455/775 (2019).

107. Cai, W., Han, J., Mei, F., Xu, Y., Ma, Y., *et al.* Observation of Topological Magnon Insulator States in a Superconducting Circuit. *Phys. Rev. Lett.* **123,** 080501. https://link.aps.org/doi/10.1103/PhysRevLett.123.080501 (8 Aug. 2019).

108. Semeghini, G., Levine, H., Keesling, A., Ebadi, S., Wang, T. T., *et al. Probing Topological Spin Liquids on a Programmable Quantum Simulator* 2021. arXiv: 2104.04119 [quant-ph].

109. Altman, E., Brown, K. R., Carleo, G., Carr, L. D., Demler, E., *et al.* Quantum Simulators: Architectures and Opportunities. *PRX Quantum* **2,** 017003. https://link.aps.org/doi/10.1103/PRXQuantum.2.017003 (1 Feb. 2021).

110. Choo, K., von Keyserlingk, C. W., Regnault, N. & Neupert, T. Measurement of the Entanglement Spectrum of a Symmetry-Protected Topological State Using the IBM Quantum Computer. *Phys. Rev. Lett.* **121,** 086808. https://link.aps.org/doi/10.1103/PhysRevLett.121.086808 (8 Aug. 2018).

111. Azses, D., Haenel, R., Naveh, Y., Raussendorf, R., Sela, E., *et al.* Identification of Symmetry-Protected Topological States on Noisy Quantum Computers. *Phys. Rev. Lett.* **125,** 120502. https://link.aps.org/doi/10.1103/PhysRevLett.125.120502 (12 Sept. 2020).

112. Smith, A., Jobst, B., Green, A. G. & Pollmann, F. *Crossing a topological phase transition with a quantum computer* 2020. arXiv: 1910.05351 [cond-mat.str-el].

113. Satzinger, K. J., Liu, Y., Smith, A., Knapp, C., Newman, M., *et al. Realizing topologically ordered states on a quantum processor* 2021. arXiv: 2104.01180 [quant-ph].

114. Mei, F., Guo, Q., Yu, Y.-F., Xiao, L., Zhu, S.-L., *et al.* Digital Simulation of Topological Matter on Programmable Quantum Processors. *Phys. Rev. Lett.* **125,** 160503. https://link.aps.org/doi/10.1103/PhysRevLett.125.160503 (16 Oct. 2020).

115. Arute, F., Arya, K., Babbush, R., Bacon, D., Bardin, J. C., *et al. Observation of separated dynamics of charge and spin in the Fermi-Hubbard model* 2020. arXiv: 2010.07965 [quant-ph].

116. Kokail, C., Maier, C., van Bijnen, R., Brydges, T., Joshi, M. K., *et al.* Self-verifying variational quantum simulation of lattice models. *Nature* **569,** 355–360. http://dx.doi.org/10.1038/s41586-019-1177-4 (2019) (May 2019).

117. Proctor, T., Rudinger, K., Young, K., Nielsen, E. & Blume-Kohout, R. Measuring the capabilities of quantum computers. *Nature physics* **18,** 75–79. ISSN: 1745-2473. https://www.nature.com/articles/s41567-021-01409-7 (2022) (Jan. 2022).

118. Boixo, S., Isakov, S. V., Smelyanskiy, V. N., Babbush, R., Ding, N., *et al.* Characterizing quantum supremacy in near-term devices. *Nature physics* **14,** 595–600. ISSN: 1745-2481. https://doi.org/10.1038/s41567-018-0124-x (2022) (June 2018).

119. Cross, A. W., Bishop, L. S., Sheldon, S., Nation, P. D. & Gambetta, J. M. Validating quantum computers using randomized model circuits. *Phys. Rev. A* **100,** 032328. https://link.aps.org/doi/10.1103/PhysRevA.100.032328 (3 Sept. 2019).

120. Kueng, R., Long, D. M., Doherty, A. C. & Flammia, S. T. Comparing Experiments to the Fault-Tolerance Threshold. *Phys. Rev. Lett.* **117,** 170502. https://link.aps.org/doi/10.1103/PhysRevLett.117.170502 (17 Oct. 2016).

121. Murphy, D. C. & Brown, K. R. Controlling error orientation to improve quantum algorithm success rates. *Phys. Rev. A* **99,** 032318. https://link.aps.org/doi/10.1103/PhysRevA.99.032318 (3 Mar. 2019).

122. Varney, C. N., Sun, K., Galitski, V. & Rigol, M. Kaleidoscope of Exotic Quantum Phases in a Frustrated *XY* Model. *Phys. Rev. Lett.* **107,** 077201. https://link.aps.org/doi/10.1103/PhysRevLett.107.077201 (7 Aug. 2011).

123. Zhu, Z., Huse, D. A. & White, S. R. Unexpected z-Direction Ising Antiferromagnetic Order in a Frustrated Spin-1/2 $J_1 - J_2$ *XY* Model on the Honeycomb Lattice. *Phys. Rev. Lett.* **111,** 257201. https://link.aps.org/doi/10.1103/PhysRevLett.111.257201 (25 Dec. 2013).

124. Zou, H., Zhao, E., Guan, X.-W. & Liu, W. V. Exactly Solvable Points and Symmetry Protected Topological Phases of Quantum Spins on a Zig-Zag Lattice. *Phys. Rev. Lett.* **122,** 180401. https://link.aps.org/doi/10.1103/PhysRevLett.122.180401 (18 May 2019).

125. Pollmann, F., Berg, E., Turner, A. M. & Oshikawa, M. Symmetry protection of topological phases in one-dimensional quantum spin systems. *Phys. Rev. B* **85,** 075125. https://link.aps.org/doi/10.1103/PhysRevB.85.075125 (7 Feb. 2012).

126. *Quantum Computer Datasheet* Google Quantum AI (May 2021).

127. team, Q. A. & collaborators. *qsim* Sept. 2020. https://doi.org/10.5281/zenodo.4023103.

128. Born, M. & Fock, V. Beweis des Adiabatensatzes. *Zeitschrift für Physik* **51,** 165–180. https://doi.org/10.1007/BF01343193 (3 Mar. 1928).

129. Developers, C. *Cirq* version v0.12.0. See full list of authors on Github: https://github .com/quantumlib/Cirq/graphs/contributors. Aug. 2021. https://doi.org/10.5281/zenodo.5182845.

130. Jones, E. B., Hillberry, L. E., Jones, M. T., Fasihi, M., Roushan, P., *et al.* Small-world complex network generation on a digital quantum processor. *Nature Communications* **13,** 4483. ISSN: 2041-1723. https://doi.org/10.1038/s41467-022-32056-y (2022).

131. Hashim, A., Naik, R. K., Morvan, A., Ville, J.-L., Mitchell, B., *et al.* Randomized Compiling for Scalable Quantum Computing on a Noisy Superconducting Quantum Processor. *Phys. Rev. X* **11,** 041039. https://link.aps.org/doi/10.1103/PhysRevX.11.041039 (4 Nov. 2021).

132. Tazhigulov, R. N., Sun, S.-N., Haghshenas, R., Zhai, H., Tan, A. T., *et al.* Simulating Models of Challenging Correlated Molecules and Materials on the Sycamore Quantum Processor. *PRX Quantum* **3,** 040318. https://link.aps.org/doi/10.1103/PRXQuantum.3.040318 (4 Nov. 2022).

133. Sedrakyan, T. A., Glazman, L. I. & Kamenev, A. Spontaneous Formation of a Nonuniform Chiral Spin Liquid in a Moat-Band Lattice. *Phys. Rev. Lett.* **114,** 037203. https://link.aps.org/doi/10.1103/PhysRevLett.114.037203 (3 Jan. 2015).

134. Sun, S.-N., Marinelli, B., Koh, J. M., Kim, Y., Nguyen, L. B., *et al. Quantum Computation of Frequency-Domain Molecular Response Properties Using a Three-Qubit iToffoli Gate* 2023. arXiv: 2302.04271 [quant-ph].

135. Ville, J.-L., Morvan, A., Hashim, A., Naik, R. K., Lu, M., *et al.* Leveraging randomized compiling for the quantum imaginary-time-evolution algorithm. *Phys. Rev. Res.* **4,** 033140. https://link.aps.org/doi/10.1103/PhysRevResearch.4.033140 (3 Aug. 2022).

136. Banerjee, A., Yan, J., Knolle, J., Bridges, C. A., Stone, M. B., *et al.* Neutron scattering in the proximate quantum spin liquid α-RuCl₃. *Science* **356,** 1055–1059. eprint: https://www.science.org/doi/pdf/10.1126/science.aah6015. https://www.science.org/doi/abs/10.1126/science.aah6015 (2017).

137. Powers, C., Bassman Oftelie, L., Camps, D. & de Jong, W. A. Exploring finite temperature properties of materials with quantum computers. *Scientific Reports* **13,** 1986. ISSN: 2045-2322. https://doi.org/10.1038/s41598-023-28317-5 (Feb. 2023).

138. Lin, S.-H., Dilip, R., Green, A. G., Smith, A. & Pollmann, F. Real- and Imaginary-Time Evolution with Compressed Quantum Circuits. *PRX Quantum* **2,** 010342. https://link.aps.org/doi/10.1103/PRXQuantum.2.010342 (1 Mar. 2021).

139. Tepaske, M. S. J., Hahn, D. & Luitz, D. J. Optimal compression of quantum many-body time evolution operators into brickwall circuits. *SciPost Phys.* **14,** 073. https://scipost.org/10.21468/SciPostPhys.14.4.073 (2023).

140. Mizuta, K., Nakagawa, Y. O., Mitarai, K. & Fujii, K. Local Variational Quantum Compilation of Large-Scale Hamiltonian Dynamics. *PRX Quantum* **3,** 040302. https://link.aps.org/doi/10.1103/PRXQuantum.3.040302 (4 Oct. 2022).

141. Lao, L., Korotkov, A., Jiang, Z., Mruczkiewicz, W., O'Brien, T. E., *et al.* Software mitigation of coherent two-qubit gate errors. *Quantum Science and Technology* **7,** 025021. https://dx.doi.org/10.1088/2058-9565/ac57f1 (Mar. 2022).

142. Lee, S., Lee, J., Zhai, H., Tong, Y., Dalzell, A., *et al.* Evaluating the Evidence for Exponential Quantum Advantage in Ground-State Quantum Chemistry. *Nature Communications* **14.** https://www.nature.com/articles/s41467-023-37587-6 (2023).

143. Babbush, R., Huggins, W. J., Berry, D. W., Ung, S. F., Zhao, A., *et al.* *Quantum simulation of exact electron dynamics can be more efficient than classical mean-field methods* 2023. arXiv: 2301.01203 [quant-ph].

144. Babbush, R., McClean, J. R., Newman, M., Gidney, C., Boixo, S., *et al.* Focus beyond Quadratic Speedups for Error-Corrected Quantum Advantage. *PRX Quantum* **2,** 010103. https://link.aps.org/doi/10.1103/PRXQuantum.2.010103 (1 Mar. 2021).

145. Bravyi, S., Gambetta, J. M., Mezzacapo, A. & Temme, K. *Tapering off qubits to simulate fermionic Hamiltonians* eprint: arXiv:1701.08213.